



저작자표시-비영리-변경금지 2.0 대한민국

이용자는 아래의 조건을 따르는 경우에 한하여 자유롭게

- 이 저작물을 복제, 배포, 전송, 전시, 공연 및 방송할 수 있습니다.

다음과 같은 조건을 따라야 합니다:



저작자표시. 귀하는 원 저작자를 표시하여야 합니다.



비영리. 귀하는 이 저작물을 영리 목적으로 이용할 수 없습니다.



변경금지. 귀하는 이 저작물을 개작, 변형 또는 가공할 수 없습니다.

- 귀하는, 이 저작물의 재이용이나 배포의 경우, 이 저작물에 적용된 이용허락조건을 명확하게 나타내어야 합니다.
- 저작권자로부터 별도의 허가를 받으면 이러한 조건들은 적용되지 않습니다.

저작권법에 따른 이용자의 권리와 책임은 위의 내용에 의하여 영향을 받지 않습니다.

이것은 [이용허락규약\(Legal Code\)](#)을 이해하기 쉽게 요약한 것입니다.

[Disclaimer](#)



공학박사 학위논문

**Preparation of novel organometallic
precursor-based printing inks and
control of phase and microstructure
of printed films**

새로운 유기금속 전구체 기반 인쇄 잉크의
제조와 인쇄 막의 상 및 미세조직 제어 연구

2014년 2월

서울대학교 대학원

재료공학부

최 윤 혁

Preparation of novel organometallic precursor-based printing inks and control of phase and microstructure of printed films

지도교수 홍국선

이 논문을 공학박사 학위논문으로 제출함

2014년 2월

서울대학교 대학원
재료공학부
최윤혁

최윤혁의 박사 학위논문을 인준함

2013년 12월

卷之二
(二)

부위위장 흥국선

卷之二

위 워 남기 태

52
(안)

위정혁석

卷之三

위 월 김 진 영

(의)

Abstract

Preparation of novel organometallic precursor-based printing inks and control of phase and microstructure of printed films

Yun-Hyuk Choi

Department of Materials Science and Engineering

College of Engineering

Seoul National University

Printing technology based on inkjet, microcontact, offset, and gravure printing techniques has attracted much attention as an alternative to conventional vacuum technology due to its fast, low-cost, large-scale manufacturability for solid-state devices, especially flexible devices. In accordance with these technological developments, the controlled preparation of ink with suitable rheological properties for specific printing processes represents a new issue. Initial studies focusing on printed electronics have focused primarily on the formation of metal electrodes using the inks based on Au, Ag, and Cu nanoparticles. However, such nanoparticle-based inks have serious limitations in industrial production owing to the difficulty in large scale synthesis, homogeneous dispersion and stable storage of the nanoparticles and the increased costs due to the use of surfactants. Therefore, the atmospheric stable, large-scale synthesizable, novel inks based on

organometallic precursors is prepared and their applicability is investigated in this dissertation.

However, no studies on the formation of solid particles or films and their sintering behavior and microstructural evolution have been attempted previously in the printed films with the organometallic precursor-based inks, unlike the case in nanoparticle-based inks. The poor adhesion of metal electrodes, including especially severe Cu, to the substrates, particularly glass, makes it harder for the printed films with organometallic precursor-based inks to be investigated. Accordingly, in this study, the novel Cu(II) complex inks based on Cu(II) formate tetrahydrate, hexylamine and ethyl cellulose were prepared with the high adhesion to substrates and the controlled viscosity, and the ink films were directly printed and heat-treated on glass, SiO₂/Si, and SnO₂:F (FTO) substrates for various device applications – the printed Cu metallization, p-type CuO gas sensor and photocathode for photoelectrochemical water splitting. The detailed studies on thermal decomposition behavior, the formation of solid particles, phase and microstructural evolution, and their sintering behavior of the Cu(II) complex inks enabled the optimization of the printing features, suitable for each device application.

In the part I, it was found that change in the molar concentration ratio between Cu(II) formate tetrahydrate precursor and hexylamine solvent in the Cu(II) complex ink induces the difference in Cu nucleation behavior during thermal decomposition of the ink through Fourier-transform infrared spectroscopy (FT-IR), thermogravimetric analysis (TGA), differential scanning calorimetry (DSC), and field emission scanning electron microscopy (FE-SEM). Specifically, Cu nanoparticles were produced with slow nucleation rate and longer nucleation time period during thermal decomposition of the film printed using the ink with the relatively low hexylamine content, resulting in the film microstructure consisting of large particles with wide size

distribution. The Cu particle packing density inside this film was low and the resulting electrical resistivity was high. In contrast, Cu nanoparticles were produced with high nucleation rate and shorter nucleation time period during thermal decomposition of the film printed using the ink with the high hexylamine content, resulting in the densely packed structure of small particles with narrow size distribution inside the film. As a result, lower electrical resistivity was achieved in this film. Based on these results, it is concluded that the metal-ion complex ink for the printed metallization requiring high electrical conductivity is desirable to be prepared with high concentration of reactive solvent to organometallic precursor in the ink. In addition, the reductive sintering of printed films under a formic acid (HCOOH) atmosphere was performed to obtain better electrical conductivity in the films by removing the oxide scales on the surfaces of the Cu nanoparticles produced during thermal decomposition of the films. As a result, the growth of Cu nanoparticles inside the films was promoted through such a reductive sintering and the electrical resistivity of the films could be reduced by an order of magnitude. Finally, an increase in the sintering temperature further decreased the film resistivity by inducing the necking and densification of the Cu nanoparticles. As a consequence, the lowest electrical resistivity of $\sim 5.2 \mu\Omega\text{cm}$ was achieved in the optimized film using selective ink formulation and reductive and higher temperature sintering processes.

In the part II, pure oxide-phase films with high crystallinity and high surface-to-volume ratio were fabricated via novel Cu(II) complex ink printing routes for functional gas sensor and photoelectrochemical device applications. First, the Cu(II) complex ink with high hexylamine content to Cu(II) precursor was used for the facile preparation of mesoporous p-type CuO sensing films. Pure polycrystalline CuO films were formed with porous structure via thermal heating from 200°C to 600°C in air. Such porous structures were formed by interconnected pore channels due to thermal

evolution of the empty space between densely packed, small Cu nanoparticles. In particular, the mesoporous CuO thin film calcined for 1 h at 500 °C in air revealed the best H₂ and C₂H₅OH gas responses, attributed to sufficient hole concentration, good crystallinity and the highest surface-to-volume ratio. The porous film calcined at 600 °C exhibited the fastest gas response rates, due to both the excellent crystallinity and the low grain boundary density. These results obtained using neat CuO provide the right direction for the development of a high-performance p-type gas sensor. Furthermore, the novel ink solution route used for fabricating the mesoporous structure in this work can provide the realization of the printed sensor devices as well as the facile approach for ion doping or alloying in oxides to improve the sensor performance.

Second, another novel, facile printing processing for preparation of pure oxide-phase films with high crystallinity and high surface-to-volume ratio was introduced. The direct printing synthesis of metal oxide hollow spheres in the form of film on a substrate is reported for the first time. This method offers facile, scalable high-throughput production and device fabrication processes. The printing was carried out by a doctor-blade method using Cu(II) complex ink with low hexylamine content. Following only thermal heating in air, well-defined polycrystalline copper oxide hollow spheres with a submicron diameter ($\leq 1 \mu\text{m}$) were formed spontaneously while being assembled in the form of film with good adhesion on the substrate. This spontaneous hollowing mechanism was found to result from the Kirkendall effect during oxidation at an elevated temperature. The CuO films with hollow spheres, prepared via direct printing synthesis at 500 °C, led to the creation of superior p-type gas sensor and photocathode for photoelectrochemical water splitting with completely hollow cores, a rough/porous shell structure, a single phase, high crystallinity, and no organic/polymer residue. As a result, the CuO hollow-sphere films showed high gas responses and permissible response speeds to

reducing gases and high photocurrent density, compared to conventional CuO powder films and to the values previously reported. These results exemplify the successful realization of a high-throughput printing fabrication method for the creation of superior nanostructured devices.

Keywords: Printed electronics, Ink, Organometallic, Microstructure, Metallization, Gas sensor, Photoelectrochemistry, Copper, Copper oxide

Student Number: 2010-31308

Contents

Chapter 1 Introduction	1
1.1 Printing technology and printed electronics.....	1
1.2 Aim and objective	4
Chapter 2 Theoretical Background	6
2.1 Sintering model of the printed film with nanoparticle-based ink	6
2.2 Sintering issues and techniques for ink-printed films.....	11
Chapter 3 Preparation of Cu(II) Complex Inks, Evolution of Phase and Microstructure of Ink-Printed Cu Films, and Control for Cu Metallization	28
3.1 Experimental	28
3.2 Formulation of novel Cu(II) complex inks with high adhesion to substrates	31
3.3 Rheological properties of Cu(II) complex inks.....	41
3.4 Thermal decomposition of Cu(II) complex inks.....	45
3.5 Nucleation and growth of Cu particles during thermal decomposition of Cu(II) complex inks	54
3.6 Cu metallization optimized	75
Chapter 4 Controlled Preparation of Ink-Printed Copper Oxide Films for Applications in Gas Sensor and Photoelectrochemical Water Splitting	77
4.1 Opening remarks	77
4.2 Direct printing synthesis of CuO mesoporous/porous thin films	81

4.3 Direct printing synthesis of copper oxide hollow spheres	106
4.4 Closing remarks	139
Chapter 5 Conclusions	140
Bibliography.....	143
Abstract (Korean).....	151

List of Tables

Table 3.1	Boiling points of various amine solvents.....	36
Table 3.2	Cu contents in commercial copper(II) formate hydrate powder and formulated inks as determined by mole calculation and ICP-AES composition analysis, respectively.....	38
Table 4.1	Comparison of performances of the pristine CuO sensors reported in the literatures.....	105

List of Figures

- Figure 2.1** A schematic representing various atomic diffusion paths between two contacting particles. Paths 1 and 2 do not produce any shrinkage while Paths 3 and 4 enable the sphere centers to approach one another, resulting in densification.....19
- Figure 2.2** A schematic based on Frenkel’s “two-sphere model” explaining the two-sphere geometry as the centers approach each other. Here, z is the neck radius, a is the initial particle radius, e is engineering strain, $L(t)$ and $L(0)$ are the instantaneous and initial distance between particle centers.....20
- Figure 2.3** Schematic representation of contactless AC sintering between a probe above the nanoparticle layer and a ground plate beneath the printing substrate.....21
- Figure 2.4** Photograph of the non-thermal atmospheric pressure plasma beam focused onto the printed track on PEN foil (a); influence of the plasma pencil height (h) on resistivity (ρ) after sintering (b); silvery appearance of the sintered feature at a height of 2 mm (b, left inset) and 4 mm (b, center inset); black appearance of the sintered feature at a height of 6 mm (b, right inset).....22
- Figure 2.5** Laser sintering process of a nanoparticle-based ink.....23
- Figure 2.6** Schematic of IPL sintering for nanosilver films using xenon flash irradiation.....24
- Figure 2.7** Electrical resistance of IPL-sintered nanosilver films as a function of incident light energy.....25
- Figure 2.8** Top: Schematic illustration showing what happens when a droplet of PDAC solution is printed on Ag NPs array. Bottom: SEM image of a printed drop zone (b) and the magnified images of NP arrays after the contact with

PDAC outside (a) and inside (c) the droplet zone.....	26
Figure 2.9 HR-SEM images and particle size distributions for printed patterns formed by Ag NPs post-treated with PDAC at various PDAC/Ag ratios (the same magnification for all images).....	27
Figure 3.1 Molecular structure of Copper(II) formate tetrahydrate ($\text{Cu}(\text{II})(\text{HCOO})_2 \cdot 4\text{H}_2\text{O}$).....	35
Figure 3.2 Electrical resistivity of Cu electrode films shown as a function of polymeric ethyl cellulose content at a processing temperature of 200 °C.....	37
Figure 3.3 A picture of the formulated inks, containing ethyl cellulose equivalent to 8.5 wt% of Cu, with the various mole ratios of copper(II) formate tetrahydrate versus hexylamine. The numbers in Figure indicate the mole ratio of copper(II) formate tetrahydrate versus hexylamine.....	39
Figure 3.4 The pH value of the formulated ink shown as a function of the molar ratio of hexylamine to Cu(II).....	40
Figure 3.5 Viscosity and shear stress of the formulated 1 : 1 ink shown as a function of the shear rate. The red solid line is the viscosity curve fitted to the Sisko model.....	43
Figure 3.6 Viscosity of the 1 : 2 and 1 : 4 inks shown as a function of the shear rate.....	44
Figure 3.7 TGA and DSC curves of commercial copper(II) formate tetrahydrate powder and 1 : 2 inks without/with ethyl cellulose.....	52
Figure 3.8 TGA and DSC profiles of neat copper(II) formate tetrahydrate powder, and 1 : 1.0, 1 : 2.5 and 1 : 4.0 inks.....	53
Figure 3.9 Cross-sectional FE-SEM micrographs of the films, printed with 1 : 1.0, 1 : 2.5 and 1 : 4.0 inks and then heated for different aging times at 200 °C in N_2 atmosphere, respectively.....	63
Figure 3.10 Particle size and distribution measured from the	

FE-SEM micrographs of Figure 3.9.....	64
Figure 3.11 Crystallite sizes of the Cu films printed with 1 : 1, 1 : 2.5 and 1 : 4.0 inks and then heated at 200 °C in N ₂ atmosphere, shown as a function of aging time.....	65
Figure 3.12 FT-IR spectra of Cu(II) precursor, hexylamine solvent, and the formulated inks, investigated at room temperature.....	66
Figure 3.13 in-situ FT-IR measurements of 1 : 1.0 and 1 : 4.0 inks while heating from 100 °C to 200 °C in air.....	67
Figure 3.14 Electrical resistivity of the Cu films printed with 1 : 1, 1 : 2.5 and 1 : 4.0 inks and then heated at 200 °C in N ₂ atmosphere, shown as a function of aging time. The inset shows the magnification of the electrical resistivity of the Cu films prepared using 1 : 2.5 and 1 : 4.0 inks.....	68
Figure 3.15 Cross-sectional FE-SEM micrographs of the films, printed with 1 : 1.0, 1 : 2.5 and 1 : 4.0 inks and then heated for different aging times at 200 °C in HCOOH atmosphere, respectively.....	69
Figure 3.16 XRD patterns of the 1 : 4.0 ink-printed films heated for 1 and 6 min at 200 °C in HCOOH, respectively.....	70
Figure 3.17 Electrical resistivity of the Cu films printed with 1 : 1, 1 : 2.5 and 1 : 4.0 inks and then heated for 1 and 6 min at 200 °C in HCOOH atmosphere, respectively.....	71
Figure 3.18 Cross-sectional views of the films printed with 1:2 ink and then heated for 5 min at 170, 200 and 250 °C in HCOOH, respectively, observed by FIB-SEM.....	72
Figure 3.19 Electrical resistivity of the films, printed with 1 : 2 ink and then heated for 2 and 5 min under HCOOH atmosphere, shown as a function of processing temperature.....	73
Figure 3.20 XPS spectra of Cu 2p and O1s and their	

quantitative comparison in the films sintered for 5 min at 200 °C under N ₂ and HCOOH atmospheres.....	74
Figure 3.21 FIB-SEM cross-sectional micrographs of 1 : 1.0, 1 : 2.5, and 1 : 4.0 ink-printed films heated for 2, 5, and 10 min at 250 °C under a reductive HCOOH atmosphere.....	76
Figure 4.1 XRD patterns of the ink-printed films heated for 1, 6, 30 and 60 min at 200 °C in air, respectively.....	79
Figure 4.2 Evolution of the peak intensity ratio (I(Cu ₂ O)/I(Cu)) between XRD peaks of Cu and Cu ₂ O of each film, shown in Figure 5.1, with aging time.....	80
Figure 4.3 (a) Grazing-incidence XRD patterns of the mesoporous CuO films, calcined for 1 h at 200-600 °C in air after being spin-coated on SiO ₂ /Si substrates with an ink solution. (b) FWHM shown as a function of calcination temperature. They were deduced from the XRD patterns of the films.....	97
Figure 4.4 The surface SEM images of the mesoporous CuO films calcined at (a) 500 and (b) 600 °C, respectively. The cross-sectional SEM images of the CuO films calcined at (c) 500 and (d) 600 °C, respectively. (e) The surface and cross-sectional porosities of both films.....	98
Figure 4.5 (a) Pt sputtered on the film after FIB fine milling to investigate the cross-section of the mesoporous CuO film calcined at 600 °C, (b) the surface morphology of the film calcined at 400 °C observed by FIB-SEM and (c) EDX patterns analyzed on the surfaces of the films calcined at 400, 500 and 600 °C, respectively.....	99
Figure 4.6 The Cu2p core level XPS spectra of the mesoporous CuO films calcined at 400, 500 and 600 °C...100	
Figure 4.7 Reversible (a) H ₂ and (b) C ₂ H ₅ OH response transients of the mesoporous CuO films calcined at 500 °C.....	101
Figure 4.8 (a) H ₂ and (b) C ₂ H ₅ OH responses of each CuO	

sensor shown as a function of operating temperature. The gas concentration dependences on (c) H ₂ and (d) C ₂ H ₅ OH responses of each CuO sensor investigated at the operating temperature of 300 °C and those on (e) H ₂ and (f) C ₂ H ₅ OH responses of each CuO sensor investigated at the operating temperature of 400 °C. (g) Response times to 1000 ppm H ₂ and (h) the initial stand-by d. c. electrical resistances in air (R _a) of each CuO sensor shown as a function of operating temperature.....	102
Figure 4.9 The ratio of gas responses of each CuO sensor shown in the operating temperatures of 300 and 400 °C, respectively.....	104
Figure 4.10 (a) XRD patterns of films calcined at each temperature after being printed on SiO ₂ /Si substrates with Cu(II) complex ink (S, □ and ● denote the peaks originating from the substrate, CuO and Cu ₂ O, respectively). (b) The evolution of the crystallite sizes of the CuO and Cu ₂ O phases in the films shown as a function of the calcination temperature as determined by the Scherrer formula.....	129
Figure 4.11 FE-SEM cross-sectional views of ink films calcined at (a) 200, (d) 300, (g) 400, (j) 500 and (m) 600 °C. The images focus on large spheres inside the ink films calcined at (b) 200, (e) 300, (h) 400, (k) 500 and (n) 600 °C, respectively. Top views of the surface morphologies of the ink films calcined at (c) 200, (f) 300, (i) 400, (l) 500 and (o) 600 °C, respectively. All scale bars are 1 μm.....	131
Figure 4.12 TEM images of the particles inside ink-printed films calcined at 200, 300, 400, 500 and 600 °C and sliced by a microtome. All scale bars are 0.5 μm.....	133
Figure 4.13 Schematic illustration depicting the spontaneous formation mechanism of copper oxide hollow spheres inside a film sample printed with Cu(II) complex ink during thermal	

heating.....	134
Figure 4.14 (a) CuO hollow spheres assembled spontaneously inside an ink-printed film sample calcined at 500 °C as observed by FE-SEM and (b) their nitrogen adsorption/desorption isotherm and Barrett-Joyner-Halenda (BJH) pore size distribution plot (inset). (c) The lattice fringes of the shell of a single CuO hollow sphere, observed by HRTEM. The inset shows the FFT pattern of the selected single-crystalline area (the inner part of the red square). (d) High-magnification HRTEM real-lattice image of the same single-crystalline area. (e) SAED pattern of the shell. (f) The Cu2p core-level XPS spectrum of the ink-printed CuO film with hollow spheres calcined at 500 °C.....	135
Figure 4.15 (a) Gas responses to C ₂ H ₅ OH, H ₂ and H ₂ S by a CuO hollow-sphere sensor measured at operating temperatures of 200, 300 and 400 °C with various gas concentrations ((1) 1000, (2) 500, (3) 250, (4) 100, (5) 50, (6) 20, (7) 10, (8) 5, (9) 2 and (10) 1 ppm). (b) Response/recovery times for H ₂ S gas shown as a function of the gas concentration at an operating temperature of 400 °C. (c) Gas responses to reducing gases of a CuO hollow-sphere sensor compared to those of a CuO powder sensor. The responses measured at 300 or 400 °C to 1000 ppm of C ₂ H ₅ OH, H ₂ , NH ₃ and CO gases and those measured at 400 °C to 10 or 20 ppm of H ₂ S gas were compared.....	137
Figure 4.16 Current density vs. applied potential (J-V) plots for CuO hollow-sphere and powder photocathodes.....	138

Chapter 1. Introduction

1.1 Printing technology and printed electronics

Technology of printed electronics is to fabricate various electronic devices through direct printing of functional ink materials. The printing technology based on liquid ink solutions has been used for about 1000 years since a word was written on a piece of paper. This technology became common with the development of a personal computer. Recently, printing technology based on inkjet, microcontact, offset, and gravure printing techniques has attracted much attention as an alternative to conventional vacuum technology because of its fast, low-cost, large-scale manufacturability for solid-state devices [1–3]. In particular, printing technology is rising as suitable processing for flexible electronics because lots of inks can be decomposed at low temperatures below glass transition temperatures of plastics.

The preparation of functional printing inks is the key factor for printing fabrication of various electronics. The printing inks should be composed of (1) the conducting, semiconducting, and insulating materials, applicable to various electronics, (2) highly soluble and stably dispersed materials in various solvents, (3) inexpensive materials, and (4) low-temperature decomposable materials.

Conductive inks have been prepared to be used in electrode and metallization. Therefore, their most critical property is the electrical conductivity. For example, the electrode pattern with high electrical

conductivity can minimize the RC delay by resistance in liquid crystal display (LCD) devices and thus rapidly responding picture on the display screens can be guaranteed. The conductive inks, used presently and studied extensively, include a conducting polymer solution [4], a metal nanoparticle-dispersed solution [5], a carbon nanotube (CNT)-dispersed solution [6], and their composite solution [7,8]. However, the developed inks are still dissatisfied. Specifically, metal nanoparticle-dispersed inks, studied most actively, can produce the electrodes with high enough electrical conductivity (\sim 10000 S/cm) for radio-frequency identification (RFID) devices, while high cost by use of dispersants and surfactants for nanoparticles and high annealing temperature (> 150 °C) for removal of them are required. In addition, homogeneous, scalable synthesis of nanoparticles should be ensured as well. The conducting polymer inks have superior manufacturability because of high dispersibility of polymer and low decomposition temperature, while they reveal the low electrical conductivity of 1-10 S/cm. The CNT-dispersed inks are used in the form of dispersion of surface-treated CNTs because of low dispersibility of a raw CNT in common solvents. They can produce the electrodes with high electrical conductivity (100-1000 S/cm) at low processing temperature near 100 °C, but their long-term stability for dispersion is still poor. Accordingly, endeavors to obtain better conductive inks should be continued.

Semiconducting inks are important for use in the preparation of active layers for functional devices and thus studied actively. They are based on organic materials such as conjugated molecules, CNT, and graphene or

inorganic materials such as metal oxide and silicon. In general, the printed active layers with the inks based on the inorganic semiconductors exhibit high mobility compared to those based on the organic semiconductors.

The inks based on the inorganic semiconductors are made up of nanoparticle-based inks and organometallic precursor-based inks. The nanoparticle-based semiconducting inks are prepared through surface treatment of semiconductor nanoparticles prepared beforehand and subsequent dispersion in solvents. Such nanoparticle-based inks have serious limitations in industrial production owing to the difficulty in large-scale synthesis, homogeneous dispersion and stable storage of the nanoparticles and the increased costs due to the use of surfactants. Therefore, the applicability of atmospheric stable and large-scale synthesizable inks, based on organometallic precursors, is alternatively proposed. However, no sintering studies have been performed in the organometallic precursor-based inks.

Meanwhile, inks with the required adhesion performance to glass substrates for high-throughput formation of printed films remain elusive. The poor adhesion of printed electrodes (particularly Cu) to the substrates, particularly glass, makes it harder for inks to be applied to electronic devices. Accordingly, adhesion promoters need to be added to inks for high-throughput processing without introducing any additional adhesion layers.

1.2 Aim and objective

In this study, novel inks based on Cu(II) complexes using organometallic precursors are prepared with controlled viscosities along with facile/scalable method, offering better atmospheric stability, compositional homogeneity and no need for dispersants/surfactants. Cu(II) formate tetrahydrate is chosen as an advantageous organometallic precursor for preparation of ion-complex inks because of its potential for facile ink formulation and low-temperature processing. An optimal amount of polymeric ethyl cellulose is added to the ink as an adhesion promoter to prevent shrinkage, dewetting and delamination of the formed Cu film during a heat treatment after printing the ink on a substrate. As a result, preparation of novel Cu(II) complex inks, which are capable of producing highly conductive, adhesive printed films, is proposed and their phase and microstructural evolution during thermal heating are systematically explored in terms of decomposition, calcination and sintering. These results are linked to improved metallization, gas sensing and photoelectrochemical properties of the printed films, and provide the right direction for the development of the high-performance printed electronics using ion-complex inks.

The originality of this study lies in that one enable the organometallic precursor-based inks having many benefits to be directly printed with high adhesion on various substrates including a glass and thus microstructure of the printed films to be investigated in detail. So far, there are no detailed studies on microstructural evolution in the films printed with organometallic

precursor-based inks. This thesis leads to new ways of ink preparation and processing for printed electronics with such microstructure studies. As a consequence, it is found that the molar concentration ratio between organometallic precursor and reactive solvent is a critical factor of microstructure evolution of the printed films through the detailed analysis. In particular, Cu electrodes with low electrical resistivity could be formed through the selective ink formulation and post-processing optimization. These are the first suggestions of ink formulation and post-processing conditions for preparing densely sintered Cu electrode films at low temperatures using the organometallic precursor-based inks. The originality of these lies mainly in preparation of novel conductive, adhesive organometallic precursor-based inks and suggestions of conditions for ink formulation and post-processing for each device application.

Furthermore, it is firstly suggested that mesoporous/porous oxide films or oxide films with hollow spheres can be synthesized through direct, facile, scalable, high-throughput printing of the organometallic precursor-based inks.

Chapter 2. Theoretical Background

2.1 Sintering model of the printed film with nanoparticle-based ink

Most of sintering studies have focused on the films printed with metal nanoparticle-based inks. The thickness, morphology, and electrical conductivity of the printed films are varied through a sintering process. The sintering is a material transport process based on the atomic diffusion driven by the reduction of surface and interfacial energy. Greer and Street represented a schematic of possible diffusion paths during sintering between two particles, as shown in Figure 2.1 [1]. Further explanation by Greer and Street is as follows [1].

Paths 1 and 2 correspond to lattice and surface diffusion, respectively. These mechanisms do not cause densification since no change in distance between the sphere centers occurs. In crystalline materials, shrinkage and resulting densification can occur only when the atoms are removed from the contact surface, or a grain boundary, so that the centers of the spheres can move towards one another (Paths 3 and 4). In these processes, the centers of spherical particles approach one another, as the neck between them widens, increasing the particle contact area. The neck formation is also driven by the reduction in surface energy by atomic diffusion, where the material fluxes from the areas of convex, or positive, curvature to the regions of negative, or concave, curvature. The energy reduction by neck formation is offset by the

energy of grain boundary creation, and this energy balance dictates the final shape of the pore. These atomic diffusion processes compete with each other: for example, surface diffusion generally prevails in the initial sintering stages, as it has the easiest transport path as well as a low activation energy. While the atomic mobility within a grain boundary is much higher than that in the lattice, it cannot accommodate a large number of atoms, so the atomic flux in the very thin grain boundary is much lower compared with that in the lattice. The activation energy for grain boundary diffusion is much lower than that for lattice diffusion, making the former prevail in the initial stages of sintering, when densification is minimal, and the latter at high temperatures, when most shrinkage occurs. One of the key factors in determining the dominant transport mechanisms is the initial particle, or grain, size: the smaller the grain, the larger the volume fraction occupied by the grain boundary. The kinetics of sintering are complex, as they depend on which of these transport mechanisms is (are) dominant.

Greer and Street [1] also suggested the sintering model relating densification and resistivity using the classical “two-sphere sintering model” by Frenkel [2,3], as shown in Figure 2.2. According to their demonstration, a simple relation between the engineering strain ε , linear dimension L, and the fractional neck radius z/a, as a function of time:

$$L(t) = L(0) \times \sqrt{1 - \left(\frac{z}{a}\right)^2} \quad (2.1)$$

where $L(0) = 2a$ is the initial distance between the sphere centers. This results in the following relationship between resistance and resistivity [1]:

$$R = \rho_0 \int_{-a}^a \frac{dx}{A} = \rho_0 \frac{1}{a^2} \int_{-a}^a \frac{dx}{\pi(z/a)^2} \quad (2.2)$$

where ρ_0 is the initial resistivity of the material, x is the distance along the centerline of the two spheres, and A is the contact area between the spheres. Assuming that the final or “fully sintered” state can be geometrically represented by a cube of side $2a$, the resistivity can be expressed in terms of the linear distance L and sphere radius [1]:

$$\rho(t) = \frac{2\rho_0}{\pi} \times \ln \left\{ \frac{a + L(t)/2}{a - L(t)/2} \right\} \quad (2.3)$$

Greer and Street [1] further considered the dependence of resistivity on time, as the net rate of atomic transport from the grain boundary to the neck is a combination of diffusion through the grain boundary (Path 4) and through the crystal lattice (Path 3). In the initial sintering phase, a relatively large fraction of the particles’ surface area is open to the exterior, making surface diffusion the dominant mechanism and resulting in insignificant shrinkage. To characterize the initial sintering phase, the known-model [4] based on transport by lattice diffusion and predicted the neck radius, and therefore

linear shrinkage, to vary as time^{2/5}, was used [1]:

$$\left(\frac{z}{a}\right)^2 = \left(\frac{80t}{\tau_L}\right)^{2/5} \quad (2.4)$$

Where $\tau_L = kTa^3/D_{lattice}\gamma_{SV}\delta^3$ is the characteristic time for sintering by lattice diffusion. Here, k is Boltzmann's constant, T is temperature, a is the particle radius, $D_{lattice}$ is the lattice diffusion coefficient, γ_{SV} is the surface energy, and δ is the atomic radius. The resulting resistivity based on this model can, then, be determined as follows [1]:

$$\rho(t) = \frac{2\rho_0}{\pi} \times \ln \left\{ \frac{2a(1 - \sqrt{1 - 5.77(t/\tau_L)^{2/5}})}{2a(1 + \sqrt{1 - 5.77(t/\tau_L)^{2/5}})} \right\} \quad (2.5)$$

In the intermediate sintering stage, when the interparticle pores are surrounded by the formed grain boundaries and little surface is exposed, Coble predicted the density β to increase linearly with time if the atomic transport between the grain boundary and the forming neck occurs through the lattice (Path 3 in Figure2.1) [5]:

$$\frac{d\beta}{dt} = \frac{336}{\tau_L} \quad (2.6)$$

Integration of Eq. (2.5) yields the following polynomial dependence between linear dimension, and therefore resistivity, and time [1]:

$$\frac{a^2 L}{2} - \frac{L^3}{24} = \frac{336}{2\pi m \tau_L} t \quad (2.7)$$

2.2 Sintering issues and techniques for ink-printed films

One of the significant issues for the films printed with metal nanoparticle-based or organometallic precursor-based inks is low-temperature sintering applicable to polymer substrates and thus flexible devices. Various sintering techniques regarding fast or selective heating have been introduced.

2.2.1. Electrical sintering

Electrical sintering was developed for the printed Ag nanoparticle layers, where the best conductivity was two orders of magnitude better than for the equivalent structures oven-sintered at the maximum tolerable temperature of the substrate [6]. The sintering is completed within several milliseconds. The schematic description of AC electrical sintering is shown in Figure 2.3. One of the key benefits of AC sintering is the possibility to perform the sintering without ohmic contacts. As shown in Figure 2.3, AC electrical sintering is performed with an experiment system where a high-voltage probe is placed above a Ag nanoparticle layer (a ground plate is placed beneath the printing substrate). A thin ($10 \mu\text{m}$) polyethylene terephthalate (PET) film is used to keep the distance between the probe and the nanoparticle layer constant, while the probe is moved around. Sintering of the nanoparticle layer occurs beneath the probe tip. The limitation of this sintering technique is that an applied voltage magnitude should be individually adjusted according to the whole dimension of each targeted layer [7].

2.2.2. Microwave sintering

Microwave sintering was introduced as the fast, selective heating tool of only the printed components [8,9]. This technique is mainly used for the sintering of ceramics and dielectric materials. It provides advantages such as uniform, fast, and volumetric heating. Microwave radiation is absorbed due to coupling with charge carriers or rotating dipoles [8]. The materials are heated by microwaves due to dielectric losses that are caused by dipole polarization. Metallic materials can be also sintered by microwave radiation, but behave as reflectors for microwave radiation, because of their small skin (penetration) depth, which is defined as the distance at which the incident power is reduced to half of its initial value. The skin depth at 2.54 GHz for Ag, Au, and Cu ranges from 1.3 μm to 1.6 μm [8]. The small skin depth results from the high conductance and the high dielectric loss factor together with a small capacitance. When instead of bulk material, the metal consists of particles and/or is heated to at least 400 °C, the materials absorbs microwave radiation to a greater extent [9]. It is believed that the conductive particle interaction with microwave radiation, i.e., inductive coupling, is mainly based on Maxwell–Wagner polarization, which results from the accumulation of charge at the materials interfaces, electric conduction, and eddy currents [9]. However, the main reasons for successful heating of metallic particles through microwave radiation are not yet fully understood.

The microwave sintering of metals is therefore non-trivial and can only be successful if the dimension of the object perpendicular to the plane of

incidence is of the same order as the penetration depth [8]. Ink-jet printed conductive layers fulfill this requirement. On the other hand, the rotational freedom of any dipoles present in thermoplastic polymers below the glass-transition temperature (T_g) is limited, which makes the polymer's skin depth almost infinite, hence transparent, to microwave radiation. Therefore, the absorption of microwave radiation by the polymer species is negligible and only the conductive particles absorb the microwaves and can be selectively sintered.

However, the electrical conductivity of the printed features sintered by this microwave sintering shows lower levels than those of recent studies.

2.2.3. Plasma sintering

Ar plasma sintering is one selective sintering approach that uses the plasma inherent excited species to remove the stabilizing agent from the particles [10]. For low pressure plasma sintering, the printed structure is forwarded to a vacuum plasma chamber that is purged with Ar. After plasma generation, excited species, like ions, radicals and UV irradiation, cause chain scission as well as decomposition of the stabilizing agent and enable the metal particles to get in direct contact with each other [10]. Due to the high surface energy of the particles and the energy that is delivered by the excited species, grain boundary diffusion and densification occur, resulting in a dense network of conductive material [10]. The decomposition products of the stabilizing molecules can easily evaporate under the applied low pressure [10]. Since

plasma irradiation decomposes the stabilizing organic materials, it also affects the polymers that are used as substrate materials [10]. Complex equipment due to the requirement of vacuum conditions and long sintering times accompanied by matting and coloring of the substrate are significant drawbacks of this process [10].

Recently, in order to overcome these issues, Wünscher et al. [10] attempted a non-thermal Ar plasma sintering approach that can be operated at atmospheric pressure and room temperature, and consequently sintering times could be reduced to several seconds while achieving similar conductivity values of above 10% compared to bulk Ag. Figure 2.4 shows photograph of the non-thermal atmospheric pressure plasma beam focused onto the printed track on polyethylene naphthalate (PEN) foil and influence of the plasma pencil height (h) on resistivity (ρ) after sintering [10].

2.2.4. Laser sintering

Laser sintering was employed to sinter the printed films with metal nanoparticle-based inks. Using laser sintering, materials can be treated selectively and this allows treating jetted nanoparticles at higher temperatures than the substrate material can tolerate. Continuous wave lasers have been commonly used in sintering studies because of the continuous beam properties during sintering [11]. The continuous wave sintering process is controlled with the laser parameters and the beam translation parameters, such as the laser power, beam shape and spot diameter [11]. The further demonstration by

Kumpulainen et al. [11] is as follows.

Laser sintering is dependent on the incident power, the absorption to the material and the interaction time. The required interaction time depends on the laser power and absorption, and defines a suitable translation velocity. A high intensity beam allows the use of a high beam velocity. However with a high beam velocity the time in which additives are evaporated and the particles are sintered is short. Lines printed with multiple layers have to be sintered with different process parameters. For example, one of the more important factors affecting the process parameters is the particle weight percent of the ink and the thickness of the line. Large amounts of carrier fluid in the structure have an effect on the sintering process, and thick lines require either multiple passes or use of a slow processing velocity.

The laser sintering process of a nanoparticle-based ink is shown in Figure 2.5 [11]. Fig. 2.5 (a) shows the ink before sintering. Dispersing agents separate the nanoparticles from each other, preventing interaction between particles. In the sintering process, the solvent must be evaporated first (Fig. 2.5 (b)) before the actual sintering can occur. After the evaporation phase, additional heating of the particles takes place. This additional heating causes the particles to start to agglomerate (Fig. 2.5 (c)). In Fig. 2.5 (d), the particles have sintered, forming a conducting pattern.

However, this local laser sintering process is carried out at a low translation stage speed and has to be conducted many times to enable large-area sintering due to the small beam diameter of several micrometer sizes.

2.2.5. Flash light sintering (Intense pulsed light (IPL) sintering)

An IPL system using a xenon flash lamp is implemented to generate the IPL via arc plasma generation. The lamp produces instant white light with a continuous spectrum for a wide range of wavelengths from 160 nm to 2.5 μm [7]. Figure 2.6 shows a schematic of the IPL sintering process under atmospheric environment at room temperature. The xenon flash lamp emits an optical spectrum of light that covers the absorption spectra of Ag nanoparticles [7]. During IPL irradiation, high intensive light energy is delivered onto nanosilver films within a few tens of miliseconds, thus instantly increasing the temperature to the melting point of Ag nanoparticles because of the photothermal effect [7]. Then, the IPL-irradiated area is transformed to the continuous metallic phase after decomposition of the organic additives around the nanoparticles. Due to the heat supply on the milisecond time scale, the thermal degradation of the polymer substrate could also be minimized [7]. In general, the electrical conductivity of IPL-sintered films increases with increasing incident light intensity, as shown in Figure 2.7.

Recently, Wang et al. reported IPL sintering of the Cu films printed using Cu ion ink [12]. Similar to the cases of printed films with nanoparticle-based inks reported in Refs. [7] and [13], the electrical conductivity of IPL-sintered films increased with increasing pulse energy.

2.2.6. Chemical sintering

A new possibility to sinter the films printed with metal nanoparticle-based inks at room temperature was recently reported [14,15]. The concept is to drop a sintering agent, a cationic polymer poly(diallyldimethylammonium chloride) (PDAC), onto an inkjet-printed Ag nanoparticle array. The sintering agent triggers the neutralization or the removal of the stabilizing polymer (polyacrylic acid) (PAA). As a consequence, the small-sized Ag nanoparticles come into contact and spontaneously coalesce into a continuous metal structure, yielding a conductivity of 20% that of bulk Ag. The conceptual illustration is shown in Figure 2.8. Furthermore, the particle sintering developed with time is revealed in Figure 2.9.

Meanwhile, a new “self-sintered” metal dispersion in which the sintering is triggered by changes in concentration of Cl^- ions was reported [15]. Specifically, the nanoparticles that are stabilized by a polymer undergo self-sintering spontaneously, due to the presence of a destabilizing agent, which comes into action only during drying of the printed pattern. The destabilizing agent, containing Cl^- ions, causes detachment of the anchoring groups of the stabilizer from the nanoparticles' surface and thus enables their coalescence and sintering. Consequently, this new sintering method of metallic ink could lead to very high conductivities of the printed pattern, by a single printing step: up to 41% of the conductivity of bulk Ag was achieved, the highest reported conductivity of a printed pattern that was obtained from nanoparticles at room temperature.

However, all of works have focused only on low-temperature densification and there is no report on the nanostructuration of printed films. In addition, studies on the sintering of printed films with organometallic-based inks are rare, compared to those of printed films with nanoparticle-based ink.

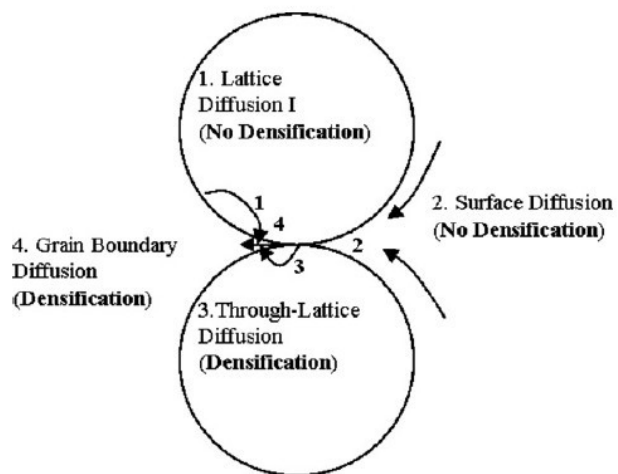


Figure 2.1. A schematic representing various atomic diffusion paths between two contacting particles. Paths 1 and 2 do not produce any shrinkage while Paths 3 and 4 enable the sphere centers to approach one another, resulting in densification [1].

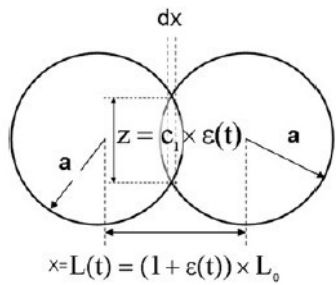


Figure 2.2. A schematic based on Frenkel's “two-sphere model” explaining the two-sphere geometry as the centers approach each other. Here, z is the neck radius, a is the initial particle radius, ε is engineering strain, $L(t)$ and $L(0)$ are the instantaneous and initial distance between particle centers [1].

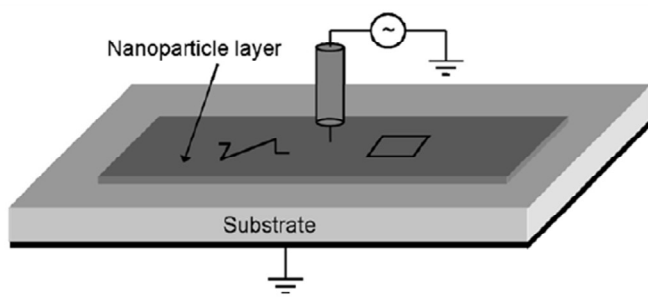


Figure 2.3. Schematic representation of contactless AC sintering between a probe above the nanoparticle layer and a ground plate beneath the printing substrate [6].

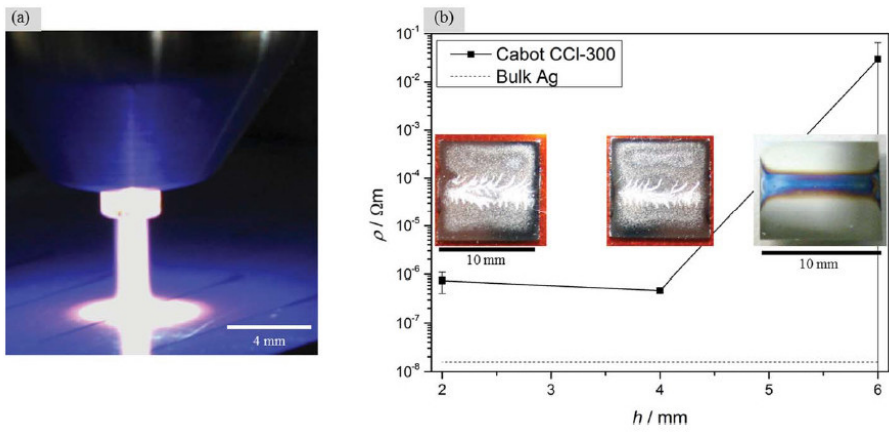


Figure 2.4. Photograph of the non-thermal atmospheric pressure plasma beam focused onto the printed track on PEN foil (a); influence of the plasma pencil height (h) on resistivity (ρ) after sintering (b); silvery appearance of the sintered feature at a height of 2 mm (b, left inset) and 4 mm (b, center inset); black appearance of the sintered feature at a height of 6 mm (b, right inset) [10].

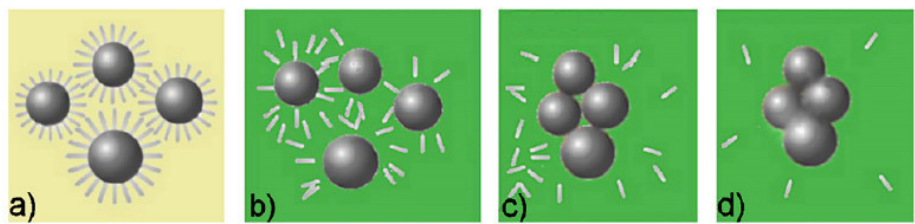


Figure 2.5. Laser sintering process of a nanoparticle-based ink [11].

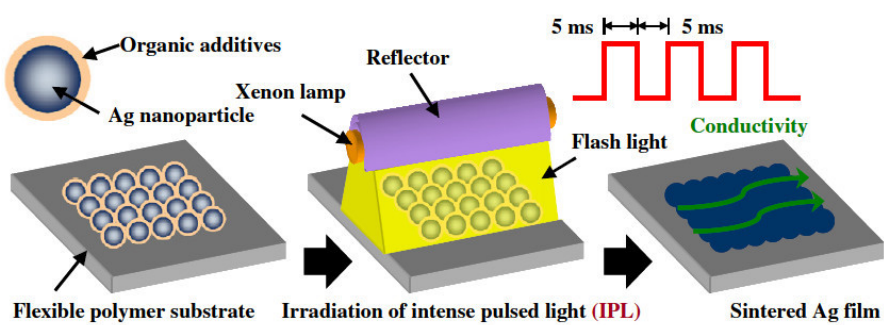


Figure 2.6. Schematic of IPL sintering for nanosilver films using xenon flash irradiation [7].

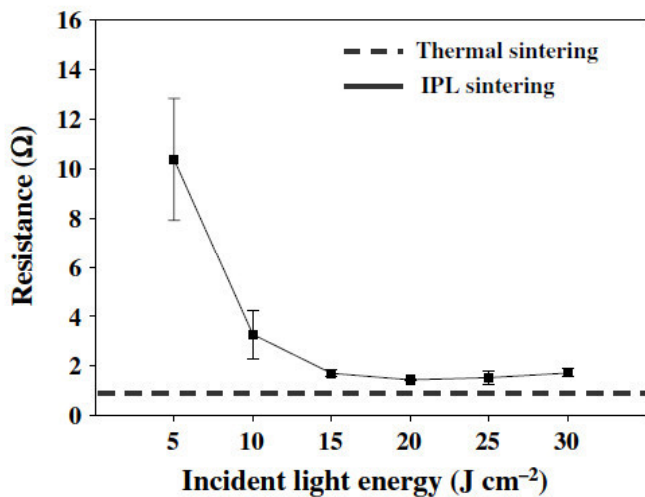


Figure 2.7. Electrical resistance of IPL-sintered nanosilver films as a function of incident light energy [7].

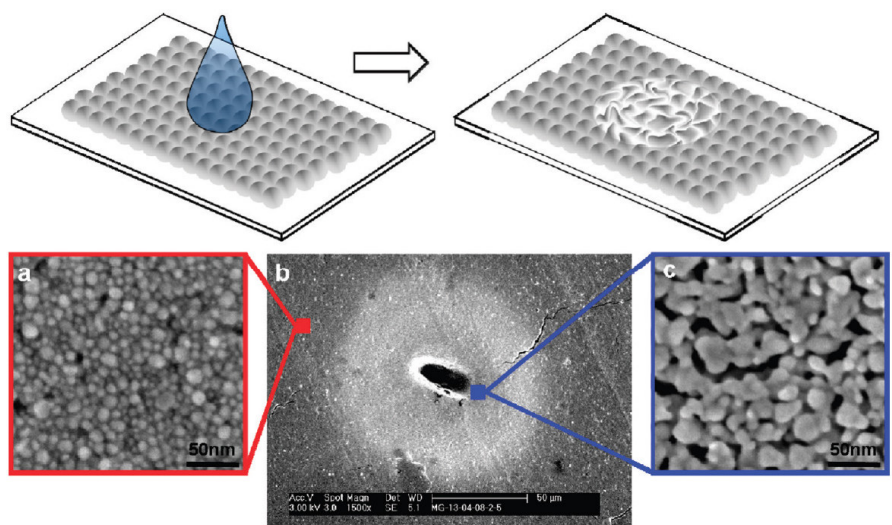


Figure 2.8. Top: Schematic illustration showing what happens when a droplet of PDAC solution is printed on Ag NPs array. Bottom: SEM image of a printed drop zone (b) and the magnified images of NP arrays after the contact with PDAC outside (a) and inside (c) the droplet zone [14].

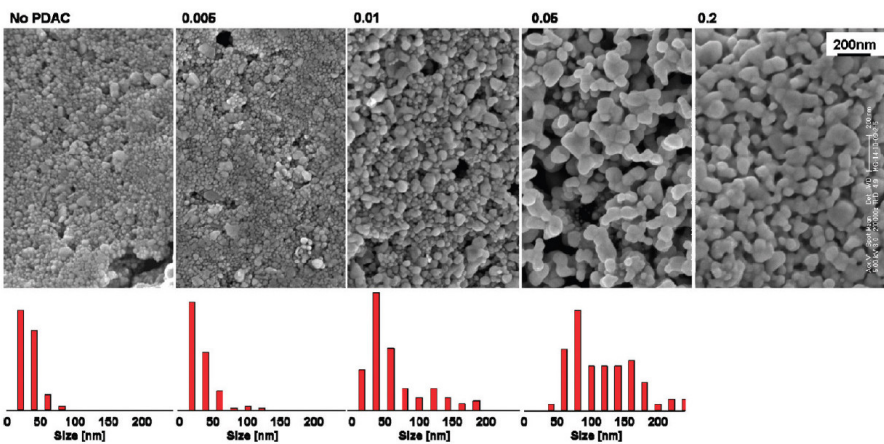


Figure 2.9. HR-SEM images and particle size distributions for printed patterns formed by Ag NPs post-treated with PDAC at various PDAC/Ag ratios (the same magnification for all images) [14].

3. Preparation of Cu(II) Complex Inks, Evolution of Phase and Microstructure of Ink-Printed Cu Films, and Control for Cu Metallization

3.1 Experimental

3.1.1. Preparation of inks

Cu(II) complex inks were formulated with copper(II) formate hydrate ($\text{Cu}(\text{HCOO})_2 \cdot n\text{H}_2\text{O}$; 97% purity; Sigma-Aldrich) as an organometallic precursor, and with hexylamine ($\text{C}_6\text{H}_{15}\text{N}$; 99% purity; Sigma-Aldrich) as a solvent. All the chemicals were used without further purification. The copper content in the commercial precursor ($\text{Cu} = 27.3$ wt%, $n = 4.4$) and the formulated inks was measured by inductively coupled plasma atomic emission spectroscopy (ICP-AES; ICPS-8100; Shimadzu). The actual concentrations of Cu in the inks, formulated from copper(II) formate tetrahydrate : hexylamine = 1 : 1 to 1 : 4, were similar to the mole-calculated values. The concentration of Cu in the inks gradually decreased as the hexylamine content was increased relative to copper(II) formate tetrahydrate.

Ethyl celluloses (9-11 mPa·s, 5% in toluene + ethanol (80:20) at 25 °C; Tokyo Chemical Industry Co., LTD.) dissolved in 1-methyl-2-pyrrolidinone (NMP; 99% purity; Sigma-Aldrich), were added to the inks as an adhesion promoter or binder. The inks containing the polymer additive were strongly

mixed with various-sized zirconia balls in a paste mixer (PDM-300; Dae Hwa Tech.; Korea) and further rotary-milled for 24 h.

The rheological properties of the inks were investigated because of their importance in practical printing applications. The shear viscosities of the inks containing ethyl cellulose (equivalent to ~8.5 wt% of Cu) were measured with various shear rates by rheometer (AR2000; TA Instruments). The thermal properties of the inks were investigated by thermogravimetric analysis (TGA) and differential scanning calorimetry (DSC) (Mettler Toledo TGA/DSC1) under N₂ atmosphere with a heating rate of 10 °C min⁻¹ from room temperature (RT) to 600 °C.

3.1.2. Film formation and characterization

The formulated inks were printed on glass substrates by doctor-blade method using Scotch tape as a spacer in order to form thick films. Corning glasses, which are extensively used in display devices, were chosen as glass substrates and cut into 5 cm × 5 cm pieces and cleaned using acetone, water and isopropyl alcohol. For comparison, the additive-free or -deficient pastes were coated on glass substrates without thermal shrinkage and dewetting. For this, the glass substrate surfaces were rendered hydrophilic by spin-coating and washing using poly(allylamine hydrochloride) (PAH; Sigma-Aldrich) solution, dissolved with 0.1 wt% in water. All the ink-coated glasses, to begin with, were baked at 60 °C for 2 min under air atmosphere. The thermal sintering processes of the films were performed on a conventional hot plate in

the temperature range from 170 °C to 250 °C for a few minutes. The sintered films were immediately quenched into RT to avoid undesirable oxidation. The printed inks were well sintered without any shrinkage or delamination during heat treatment.

The phase and average grain size of the sintered films were detected by X-ray diffraction θ - 2θ method (XRD; X’Pert Pro MPD; PANalytical) using Cu K_a radiation ($\lambda = 0.154$ nm). The cross-sectional microstructures of the films were investigated by a dual-beam focused ion beam scanning electron microscopy (FIB-SEM; Helios 400S; FEI) with an accelerating voltage of 2 kV and a beam current of 43 pA for SEM and with a voltage of 30 kV and a current of 0.28 nA for FIB fine milling. To calculate the average porosities of the films from the cross-sectional SEM images, solid (white)/pore (black) binary 2-dimensional images were analyzed by using simple programming. The sheet resistance and thickness of the films were measured by conventional 4-point probe and surface profiler, respectively, and then converted into electrical resistivity. The adhesion properties between the films and the glass substrates were classified merely as pass or fail by a 180° peel test (ASTM D903-49) using 3M tapes.

3.2 Formulation of novel Cu(II) complex inks with high adhesion to substrates

The criteria of organometallic precursor selection for the printing inks are the following: (1) stability, (2) low-temperature decomposition for flexible plastic device application, and (3) inexpensive cost. Thus far, various Copper(II)-organic compounds have been used as precursors for the printing inks. However, the conventional precursors have many problems violating the criteria of selection, as mentioned above. For example, Copper(II) hydroxide ($\text{Cu}(\text{OH})_2$) induce is very sensitive to pH of an ink and thus it induces the ink instability [1]. bis[2-(methoxyimino)propanoato] copper(II) (1) produce severe organic residue, which resulting in the film instability, during its decomposition [2]. Copper(II) neodecanoate is decomposed at high temperature near $300\text{ }^\circ\text{C}$, which is over glass transition temperature (T_g) of plastics [3].

In this study, a formulation containing Copper(II) formate tetrahydrate (its molecular structure is shown in Figure 3.1) as an organometallic precursor was chosen as one of the best candidates for a novel metal-ion complex ink for the following reasons: (1) Copper(II) formate tetrahydrate ($\text{Cu}(\text{HCOO})_2 \cdot 4\text{H}_2\text{O}$) is resistant to oxidation in air, (2) it is reduced to metallic copper at temperatures as low as $150\text{--}250\text{ }^\circ\text{C}$ [4], (3) it reduces to metallic Cu with minimal residue ($2\text{Cu}(\text{HCOO})_2 \rightarrow 2\text{Cu} + \text{CO} + 3\text{CO}_2 + \text{H}_2 + \text{H}_2\text{O}$; or $\text{Cu}(\text{HCOO})_2 \rightarrow \text{Cu} + 2\text{CO}_2 + \text{H}_2$) [5,6], and (4) the materials are relatively inexpensive. In Copper(II) formate tetrahydrate, Cu^{2+} is resistant to oxidation because of its high ionization energy, 3553 kJ/mol . The low reduction

temperature of Copper(II) formate tetrahydrate is advantageous for the fabrication of flexible electronics whose processing temperature is limited by the T_g of plastic substrates. A processing temperature greater than T_g causes the deterioration of both substrates and devices, but the reduction temperature of Copper(II) formate tetrahydrate is comparable to or lower than the T_g values of commercial polymer substrates: polyethylene naphthalate, 150 °C; polycarbonate, 145 °C; cyclic olefin co-polymer, 164 °C; polyether sulfone, 223 °C; polyimide, <300 °C [7].

Hexylamine ($C_6H_{15}N$) was used as a solvent for the ink formulation because of the following reasons. First, Copper(II) formate tetrahydrate precursor is very soluble in the amine solvents while Copper(II) formate – amine complexes are formed with the following reaction.



Secondly, hexylamine has relatively low boiling point (132 °C) among various amines, compatible with the ink formulation for application in flexible plastic devices. The boiling points of various amine solvents are compared in Table 3.1. Therefore, hexylamine was selected as an optimized solvent for the novel ink system in this study.

Finally, polymeric ethyl cellulose dissolved in 1-methyl-2-pyrrolidinone (NMP) was added to the inks as an adhesion promoter because the addition of ethyl cellulose increases the adhesion of ink-printed films to substrates. The inks containing the polymer additive were strongly mixed with various-sized

zirconia balls in a paste mixer and further rotary-milled for 24 h. In order to investigate the effect of polymer content on properties of the ink-printed films, the electrical resistivity and adhesion property of the films calcined for 2 min at 200 °C under HCOOH atmosphere after being printed on glass substrates were evaluated with various ethyl cellulose contents in copper(II) formate tetrahydrate : hexylamine = 1 : 2 ink. Figure 3.2 shows that the resistivity of the films gradually increased as the ethyl cellulose content was increased relative to Cu in the ink. The films coated with the inks with an ethyl cellulose concentration below 4 wt% relative to Cu were severely shrunk and delaminated on the glass substrates during sintering above 170 °C, indicating poor adhesion with the glass substrates and hence their unsuitability to investigate film properties. Alternatively, their resistivities were measured with the films processed on poly(allylamine hydrochloride) (PAH)-treated substrates. The films containing ethyl cellulose equivalent to more than ~8.5 wt% of Cu reliably passed an adhesion test. As a result, the ink with ethyl cellulose equivalent to ~8.5 wt% of Cu exhibited the maximum electrical conductivity while maintaining strong adhesion with glass substrates. Therefore, ethyl cellulose equivalent to ~8.5 wt% of Cu was contained in all the inks in this study. The films formed with the 1:2 ink showed an electrical resistivity of ~10 $\mu\Omega\text{cm}$ (Figure 3.2).

On the basis of the selection of each ink component, novel Cu(II) complex inks were formulated successfully, containing Copper(II) formate tetrahydrate (organometallic precursor), hexylamine (solvent) and ethyl cellulose dissolved in NMP (adhesion promoter). Cu contents in commercial copper(II) formate

hydrate powder and formulated inks as determined by mole calculation and ICP-AES composition analysis, respectively, are shown in Table 3.2. The copper content in the commercial precursor ($\text{Cu} = 27.3 \text{ wt\%}$, $n = 4.4$) and the formulated inks was measured by inductively coupled plasma atomic emission spectroscopy (ICP-AES). The actual concentrations of Cu in the inks, formulated from copper formate tetrahydrate : hexylamine = 1 : 1 to 1 : 4, were similar to the mole-calculated values. The concentration of Cu in the inks gradually decreased as the hexylamine content was increased relative to copper(II) formate tetrahydrate. A picture of the formulated inks, containing ethyl cellulose equivalent to $\sim 8.5 \text{ wt\%}$ of Cu, is shown with the various mole ratios of copper formate tetrahydrate versus hexylamine in Figure 3.3. The 1 : 1, 1 : 2 and 1 : 2.5 inks were opaque sky-blue, the 1 : 2.8 ink was translucent navy-blue, and the 1 : 3, 1 : 3.3, 1 : 3.6 and 1 : 4 inks were transparent dark-blue, indicating that the inks became more transparent and with a darker blue color as the mole content of hexylamine was increased relative to copper(II) formate tetrahydrate.

The pH value of the formulated ink increases linearly with increasing the molar ratio of hexylamine to Cu(II), as shown in Figure 3.4. This simply shows that the number of OH^- ion and thus basicity in the ink increases linearly with the hexylamine content.

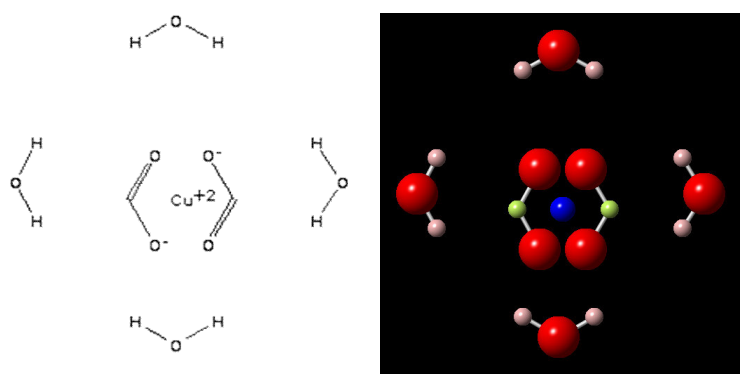


Figure 3.1. Molecular structure of Copper(II) formate tetrahydrate $(\text{Cu}(\text{II})(\text{HCOO})_2 \cdot 4\text{H}_2\text{O})$.

Solvent	Dibutylamine	Diamylamine	Dihexylamine	Hexylamine	Heptylamine	Octylamine	Nonylamine
Boiling point (°C)	159	203	194	132	155	176	201

Table 3.1. Boiling points of various amine solvents.

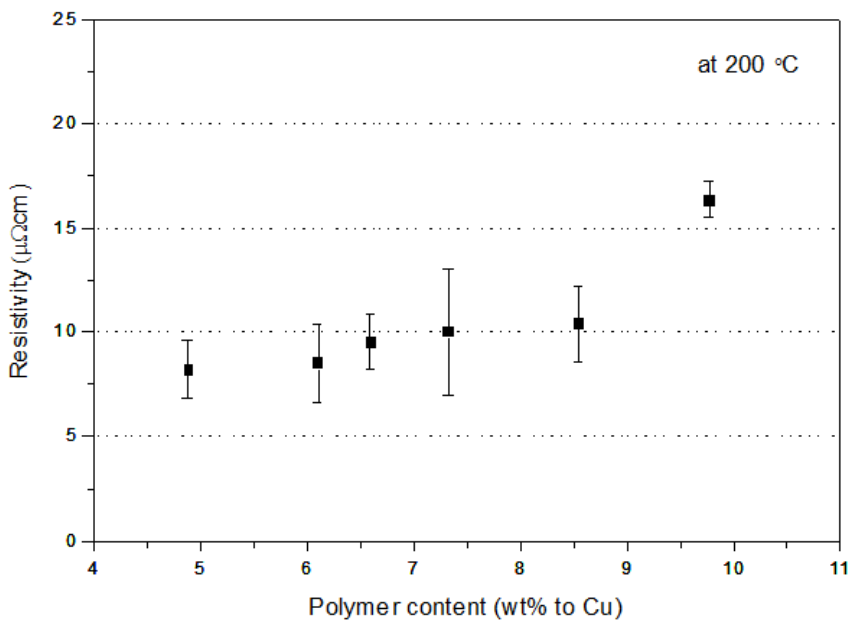


Figure 3.2. Electrical resistivity of Cu electrode films shown as a function of polymeric ethyl cellulose content at a processing temperature of 200 °C.

Ink sample (mole ratio of Cu(II) formate hydrate <i>versus</i> hexylamine)	Cu calculated (wt%) Value (Purity-calibrated)	Cu measured by ICP-AES (wt%) Value
Cu(HCOO) ₂ ·nH ₂ O	N/A	27.3 ± 0.8 (n=4.4 → Tetrahydration)
1:1.0	18.6	18.4 ± 0.6
1:2.0	14.3	14.3 ± 0.1
1:2.5	12.8	12.6 ± 1.0
1:2.8	12.1	11.8 ± 0.7
1:3.0	11.6	11.3 ± 0.9
1:3.3	11.0	10.6 ± 0.4
1:4.0	9.8	9.5 ± 0.3

Table 3.2. Cu contents in commercial copper(II) formate hydrate powder and formulated inks as determined by mole calculation and ICP-AES composition analysis, respectively.



Figure 3.3. A picture of the formulated inks, containing ethyl cellulose equivalent to 8.5 wt% of Cu, with the various mole ratios of copper(II) formate tetrahydrate versus hexylamine. The numbers in Figure indicate the mole ratio of copper(II) formate tetrahydrate versus hexylamine.

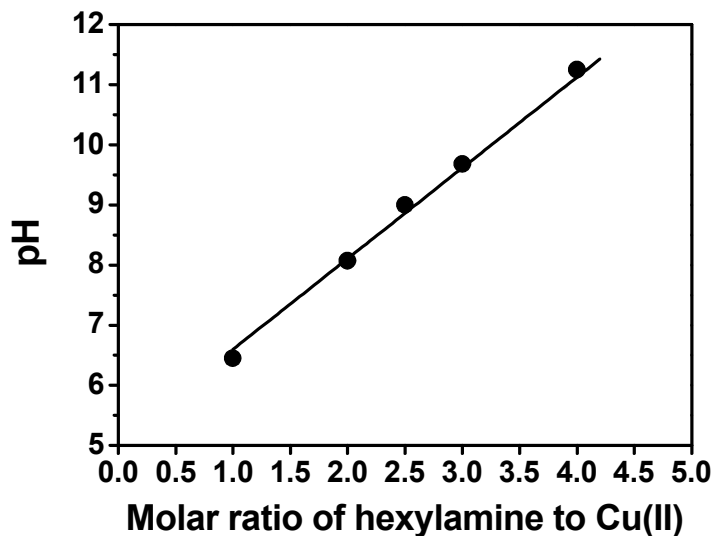


Figure 3.4. The pH value of the formulated ink shown as a function of the molar ratio of hexylamine to Cu(II).

3.3 Rheological properties of Cu(II) complex inks

The rheological properties of the inks were investigated because of their importance in practical printing applications. The apparent viscosity of the inks decreased with increasing hexylamine content relative to copper formate tetrahydrate. The shear viscosities of the 1 : 1, 1 : 2 and 1 : 4 inks containing ethyl cellulose (equivalent to ~8.5 wt% of Cu) were compared with various shear rates by a rheometer at room temperature (RT) and the measurements are shown in Figure 3.5 and 3.6. All the inks showed a non-Newtonian flow with typical pseudoplastic (or shear thinning) behavior, i.e., decreasing viscosity and increasing shear stress with an increase in the applied shear rate, as is generally shown in paints and emulsions [8]. The viscosity value (23.58 Pa·s (or 23580 cP)) of the 1 : 1 ink measured at a shear rate of 1 s⁻¹ was nearly twice as high as that (11750 cP) of an 1 : 2 ink formulated with twice the amount of hexylamine. The viscosity value of the 1 : 2 ink was nearly twice that (5790 cP) of the 1 : 4 ink.

The shear stress was further measured as a function of the shear rate according to the log-log plot in the 1 : 1 ink. No yield stress was observed. The viscosity (η) curve was fitted to the Sisko model [9], as shown by the red solid line in Figure 3.5. The Sisko equation is written as

$$\eta = \eta_\infty + K_2 \dot{\gamma}^{n-1} \quad (3.2)$$

where η_∞ is the limiting viscosity in the high-shear-rate regime, K_2 is the consistency index, $\dot{\gamma}$ is the shear rate, and n is the power-law index. If $n = 0$, then the following holds:

$$\eta = \eta_\infty + \frac{K_2}{\dot{\gamma}} \quad (4.3)$$

From the fitting result, it was found that η_∞ and K_2 were $0.68 \text{ Pa}\cdot\text{s}$ and $26.3 \text{ Pa}\cdot\text{s}^n$, respectively. By considering the viscosities, the present inks are particularly suitable for practical knife-over-edge, screen, slot-die and offset printing applications for printed electronic devices [10]. Importantly, the viscosity of the ink is controlled only by chemical coupling depending on the quantitative ratio between the organometallic precursor and hexylamine solvent. A small amount of polymeric ethyl cellulose added to the ink contributes only to an improvement in the adhesion, printability (or coatability) and film formability during a heat treatment after printing the ink on a substrate.

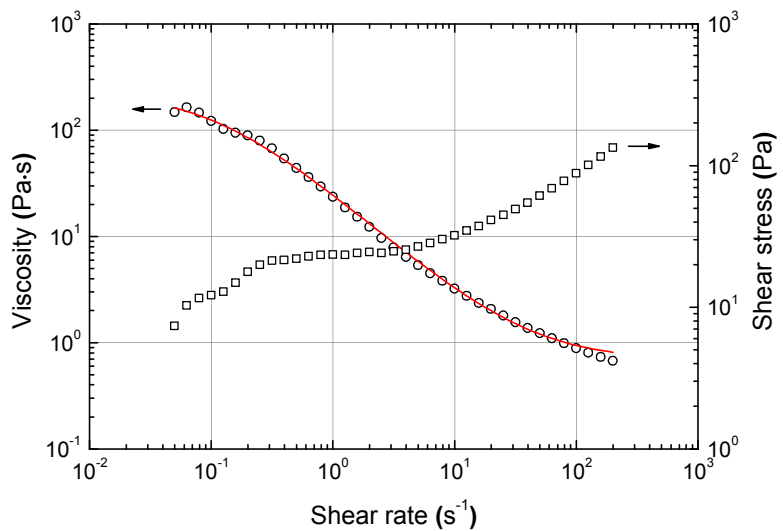


Figure 3.5. Viscosity and shear stress of the formulated 1 : 1 ink shown as a function of the shear rate. The red solid line is the viscosity curve fitted to the Sisko model.

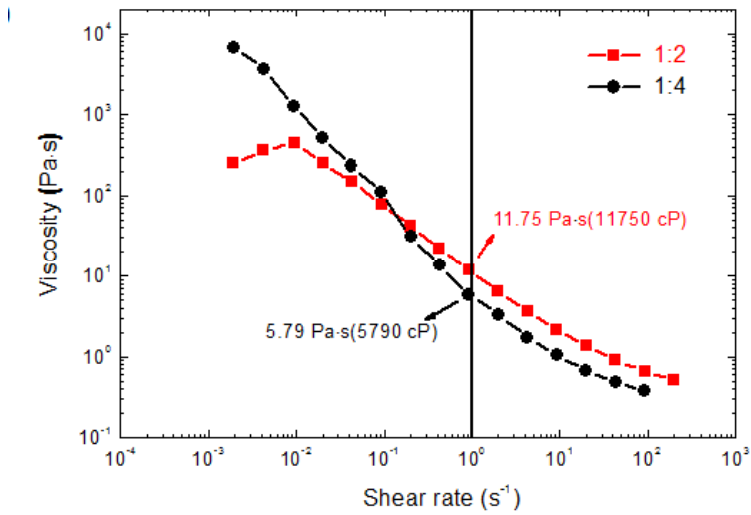


Figure 3.6. Viscosity of the 1 : 2 and 1 : 4 inks shown as a function of the shear rate.

3.4 Thermal decomposition of Cu(II) complex inks

The thermal decompositions of a commercial copper(II) formate tetrahydrate ($\text{Cu}(\text{HCOO})_2 \cdot 4\text{H}_2\text{O}$) and the formulated inks with or without ethyl cellulose were investigated by TGA and DSC. For it, the samples were heated from RT to 600 °C at a rate of 10 °C/min under N₂ atmosphere. As shown in Figure 3.7, the neat copper(II) formate tetrahydrate powders were completely decomposed at approximately 240 °C via a discrete two-step behavior. The first decomposition was completed near 115 °C with a weight loss of 32.5%, which is in computationally good agreement with the dehydration of tetrahydrate (n = 4). Previous ICP-AES analysis also indicated a total of 4.4 hydrates. This suggested that the commercial precursors were coordinated by tetrahydrate. The existence of dihydrate and tetrahydrate in copper(II) formate has been previously reported [11-15]. In addition, the dehydration process of the copper(II) formate tetrahydrate could be well analogized from its DSC result (Figure 3.7). Three endothermic peaks emerged at 56, 85 and 112 °C, which corresponded with the report of Heyns et al. that the dehydration of $\text{Cu}(\text{HCOO})_2 \cdot 4\text{H}_2\text{O}$ proceeds in three steps with TGA and differential thermal analysis peaks at 55, 63 and 95 °C with a heating rate of 10 °C/min. Each peak represents the stepwise transformed decompositions, $\text{Cu}(\text{HCOO})_2 \cdot 4\text{H}_2\text{O} \rightarrow$ monoclinic anhydrous $\text{Cu}(\text{HCOO})_2$ (the dissociation of H₂O at 56 °C and the phase transformation at 85 °C were assumed in our case) \rightarrow orthorhombic anhydrous $\text{Cu}(\text{HCOO})_2$ (this explains the peak at 112 °C in our case) [15]. Subsequently, the anhydrous $\text{Cu}(\text{HCOO})_2$

showed a further one-step weight loss of 39.4% in the temperature range from 173 °C to 240 °C, suggesting the dissociation of the formate group from it (see TGA result in Figure 3.8).

In a contrasting result, Mohamed et al. [16] have previously presented that the decomposition of anhydrous Cu(HCOO)₂ under N₂ atmosphere occurs via a two-step mechanism at 110-190 °C and 190-213 °C, which was attributed to stepwise cation reduction, Cu²⁺ → Cu⁺ → Cu⁰, with breakup of the formic groups from the salt. Despite this difference, it is considered that both the dissociation of formic groups and the reduction into metallic Cu in anhydrous Cu(HCOO)₂ contributed to the one-step weight loss as the temperature was increased from 173 °C to 240 °C, because the amount (39.4%) of the weight loss agreed well with the calculated weight percent (39.9%) of 2HCOO in Cu(HCOO)₂·4H₂O. The corresponding DSC peak was weakly observed near 203 °C (Figure 3.7). Finally, the Cu content remained at 28.1%, which is nearly the same as the value (27.3 ± 0.8) confirmed by ICP-AES in Table 3.2, up to 600 °C after completing the decompositions up to 240 °C.

The TGA results of the inks comprised of copper(II) formate tetrahydrate dissolved in hexylamine with a mole ratio of 1 : 2, without and with ethyl cellulose, are shown in Figure 3.7. The weight losses of 29.3% (without ethyl cellulose) and 23.8% (with ethyl cellulose) were firstly observed up to nearly 140 °C. This was attributed to the results of dehydration, although those are slightly more than that of the calculated weight percent (16.8%). In addition, the second weight losses of 39.0% (without ethyl cellulose) and 38.2% (with ethyl cellulose) similarly occurred from ~140 °C to ~173 °C. They were lower

than the weight (47.2%) of the whole hexylamine (boiling point = 130 °C). This indicated that amine groups were coupled with formates of the anhydrous Cu(HCOO)₂ so that the bound amines still survived above their boiling point. An additional weight loss of 13.3% to 240 °C was detected, so that 18.4% of the metallic Cu finally remained in the ink without ethyl cellulose. Indeed, the sum (21.5%) of the final weight loss (13.3%, which was assumed to be formate) decomposed up to 240 °C and that (8.2%; the difference between the calculated weight (47.2%) of the whole hexylamine and that (39.0%) missed out to 170 °C, which was assumed to be the residual hexylamine, bound with formate) passing through 173 °C coincides very well with the loss (21%; calculated) of 2HCOO from the ink in the range from 173 °C to 240 °C.

On the other hand, except for the third weight loss to 240 °C, a small residue tail was observed up to near 400 °C in the ink with ethyl cellulose (see TGA result in Figure 3.7). This undoubtedly originated from the ethyl cellulose contained in the ink. The thermal degradation of ethyl cellulose occurs in the temperature range from 260 °C to 390 °C [17], which corresponded well with our observation. Accordingly, all of the films, processed below 400 °C with the ink in the next steps, were expected to possess ethyl cellulose, which is desirable for adhesion with glass substrates. The last weight loss of the ink was 21.6%, higher than that of the ink without ethyl cellulose, which was attributed to the addition of both the vaporization of NMP (boiling point = 202-204 °C) and the decomposition of ethyl cellulose. Finally, the residual Cu was 16.4%. As a consequence, it is speculated that the

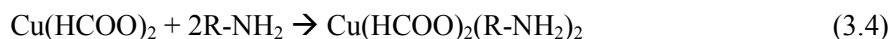
second and third weight losses of both inks were strongly dependent on the chemical reaction and dissociation between amine and formate. This is discussed in detail below. The DSC results (Figure 3.7) of both the inks showed three major peaks at 121, 155 and 230 °C, which matched the three-step decompositions shown in the TGA results.

To investigate the effect of the different volume of hexylamine on the thermal decomposition behavior of the ink, the thermal behavior of the inks formulated with the different hexylamine amount was further analyzed using TGA and DSC (Figure 3.8). For it, the samples were heated from 30 °C to 300 °C at a rate of 10 °C/min under N₂ atmosphere. The DSC profiles of each ink indicated two endothermic reactions, and the reaction temperatures were consistent with those at which the slopes of the TGA profiles changed. Endothermic peaks at 142, 150, and 165 °C for 1 : 4.0, 1 : 2.5, and 1 : 1.0 inks, respectively, were consistent with the temperatures at which the TGA profiles indicated major weight losses. In addition, endothermic peaks at higher temperatures (200, 225, and 247 °C for 1 : 4.0, 1 : 2.5, and 1 : 1.0 inks, respectively) occurred at the temperatures at which the weight of the ink decreased to the weight of the final residue in TGA profile. On the basis of pyrolysis-gas chromatography/mass spectrometry (Py-GC/MS) analysis, the weight losses were attributed to vaporization of hexylamine, 5-ethyl-2-methyl piperidine, and N-1-hexylformamides (their boiling points are 130, 160, and 245 °C, respectively [18]) during reduction of Cu²⁺.

TGA profiles for thermal decomposition of all the inks are divided by three steps, contrary to the two-step decompositions shown in the neat Cu(II)

formate tetrahydrate precursor. In the first step, the H₂O molecules, dehydrated from the precursor in the ink, are vaporized in the range of 130-142 °C. Subsequent decompositions occur at 142-176 °C for 1 : 1.0 ink, at 131-169 °C for 1 : 2.5 ink, and at 130-166 °C for 1 : 4.0 ink, respectively. These decompositions are associated with the vaporization of hexylamine coupled with formate group including 5-ethyl-2-methyl piperidine (boiling point = 160 °C), which is the organic reactant produced between hexylamine and formate. Final decompositions occur at 176-250 °C for 1 : 1.0 ink, at 169-231 °C for 1 : 2.5 ink, and at 166-206 °C for 1 : 4.0 ink, respectively. These indicate the decomposition of the formate group from Cu(HCOO)₂ along with that of N-1-hexylformamides (boiling point = 245 °C) and resulting precipitation of metallic copper.

Importantly, in all the steps, the temperature range and the temperature for decomposition decrease with increasing the molar concentration of hexylamine to Cu(II) formate tetrahydrate precursor in the ink. It is believed that formate group acts as a stabilizing agent for Cu(II) in the ink system. When the molar concentration of hexylamine to Cu(II) increases, Cu(II) - formate coupling (bonding) strength weakens because of stronger formate - hexylamine reaction with the following reaction.

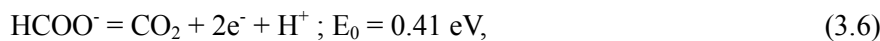
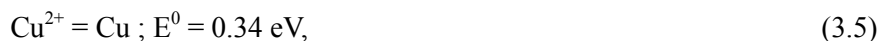


Such a new bonding is formed with some heat emissions as soon as Cu(II) formate tetrahydrate is mixed with hexylamine at room temperature. As a

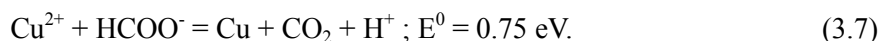
result, weakening in Cu(II) - formate coupling (bonding) strength by hexylamine will lead to the decrease in energy barrier for Cu nucleation by the subsequent reduction of Cu²⁺ and thus the increase in nucleation rate of Cu particles with shorter nucleation time periods during thermal decomposition of the Cu(II) complex ink, as the molar concentration of hexylamine to the precursor (or Cu(II)) increases. Shorter nucleation time periods in the ink with high hexylamine content may also originate from more rapid depletion of relatively low metal precursor source in the ink. At last, such a difference in the nucleation and growth of Cu in the inks will induce the difference in microstructure of the ink-printed and then heat-treated films. The difference in microstructure and phase will be addressed in the next chapter.

The variation of the ink viscosity is also considered to originate from such a difference in Cu(II) - formate - hexylamine coupling (bonding) state.

The increase of pH and thus OH⁻ (basicity) in the ink with hexylamine may also weaken the activity of formate group as a stabilizing agent for Cu²⁺ and thus promote Cu nucleation. According to the standard reduction potentials of Cu²⁺ and formate [19,20],



and thus



According to Eq. 3.7, Cu²⁺ with formate is preferentially reduced to Cu, and the higher hexylamine concentration presumably enhances the reduction reaction because hexylamine decreases the H⁺ concentration.

Furthermore, in the DSC profiles in Figure 3.8, relatively sharp endothermic peaks at 130 °C for 1 : 4.0 and 1 : 2.5 inks represent the vaporization of hexylamine (the boiling point of hexylamine is 130 °C). The peak intensity decreased as the ratio of hexylamine to Cu decreased, and the peak was not detected for 1 : 1.0 ink. As the molar concentration of hexylamine in the ink decreases, the portion to volatilization of free hexylamine with the relatively low boiling point (130 °C) decreases while that of the formate-amine couples, i.e., bound hexylamine, and 5-ethyl-2-methyl piperidine at 140-173 °C and N-1-hexylformamides near 240 °C with the higher boiling points, increases. As a result, these led to the increase in reaction temperature for decomposition and the decrease in the peak intensity in the DSC profile of the ink.

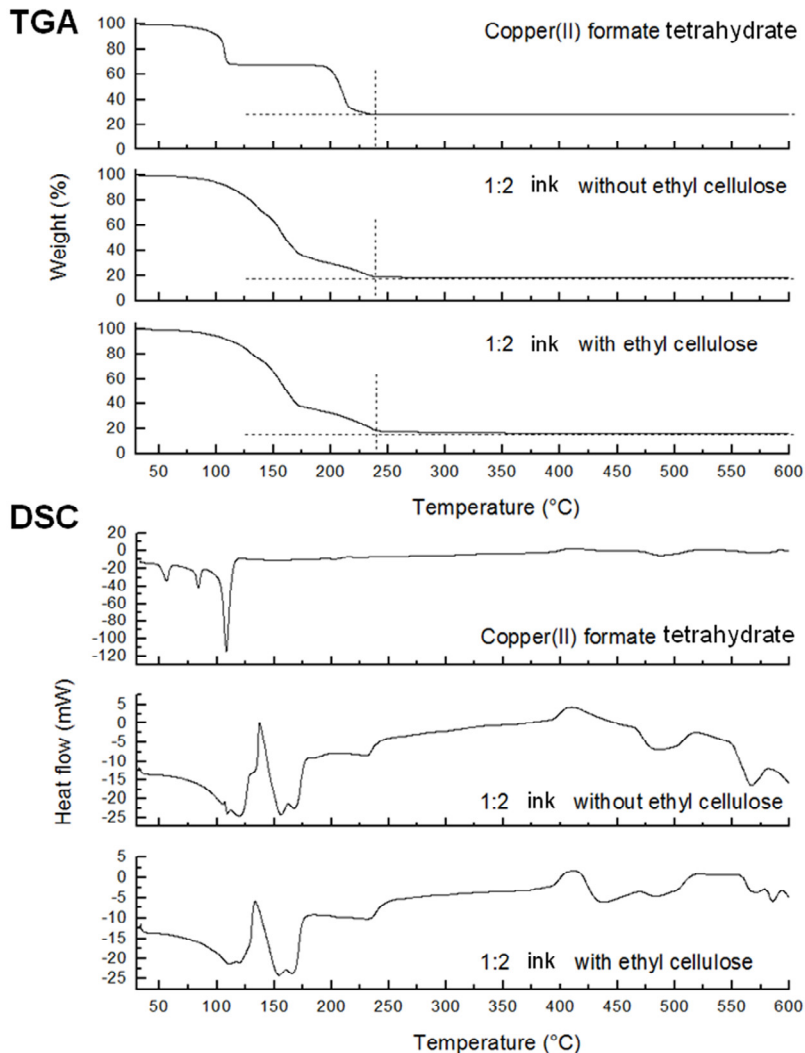


Figure 3.7. TGA and DSC curves of commercial copper(II) formate tetrahydrate powder and 1 : 2 inks without/with ethyl cellulose.

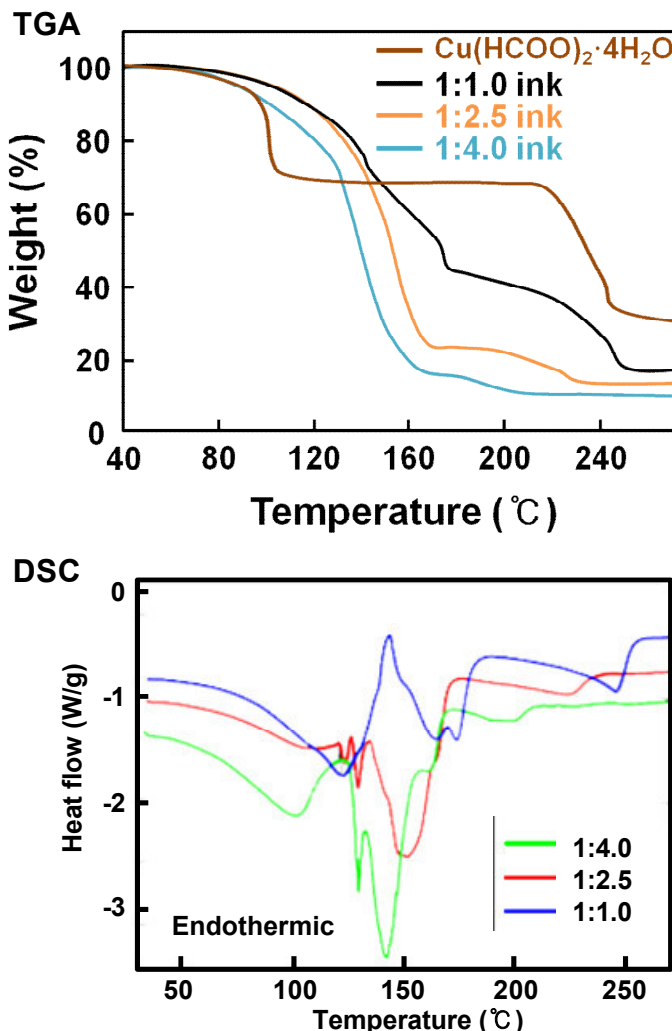


Figure 3.8. TGA and DSC profiles of neat copper(II) formate tetrahydrate powder, and 1 :1.0, 1 : 2.5 and 1 : 4.0 inks.

3.5 Nucleation and growth of Cu particles during thermal decomposition of Cu(II) complex inks

The cross-sectional FE-SEM micrographs of the films, printed with 1 : 1.0, 1 : 2.5 and 1 : 4.0 inks and then heated for different aging times (1-60 min) at 200 °C in N₂ atmosphere, respectively, are shown in Figure 3.9. It was confirmed by XRD analysis that all the films consist of pure polycrystalline Cu. The particle size and distribution measured from the micrographs are shown in Figure 3.10. As the molar concentration of hexylamine to Cu(II) in the used ink increased, the size and distribution of the produced particles decreased and the film density increased, remarkably. The decrease in the particle size and distribution inside the produced film with increasing the hexylamine content in the used ink can be clearly explained by the increase in Cu nucleation rate with shorter nucleation time periods during thermal decomposition of the film printed with the ink containing higher hexylamine concentration, as predicted by the earlier TGA and DSC studies. As smaller particles have higher specific surface area and thus higher surface energy, their agglomeration is promoted by the Gibbs-Thomson effect. Therefore, the density of the film printed with the ink with high hexylamine concentration is increased by the reduced size of constituted particles. The particle size increased gradually with aging time through the films, due to the sintering effect.

The Cu crystallite sizes of each film were obtained from Scherrer formula using the XRD peaks. The crystallite sizes of the Cu films printed with 1 : 1,

1 : 2.5 and 1 : 4.0 inks and then heated at 200 °C in N₂ atmosphere were shown as a function of aging time in Figure 3.11. Similarly to the case of the particle size observed by FE-SEM, the crystallite size of the printed Cu film decreased with increasing the hexylamine concentration in the ink. Hence, it is thought that the Cu particles are grown by coalescence of smaller crystallites. The crystallite size abruptly increased for 1 min, and afterward exhibited very slight increase with aging time through the films. This significantly indicates that most of the size of nuclei/crystallites/particles is determined in the very rapid initial nucleation stages.

To further clarify the difference in nucleation behavior during thermal decomposition of the inks, the existing organic functional groups in Cu(II) precursor, hexylamine solvent, and the inks were investigated by Fourier-transform infrared (FT-IR) spectroscopy at room temperature, respectively (Figure 3.12). As a result, the transmittance intensity of broad peak originating from carboxylic acids with hydrogen bonding (O-H stretch) weakened with increasing molar concentration of hexylamine solvent in the ink. This indicates that formate group (carboxylic acid; HCOO⁻) in copper formate (Cu(HCOO)₂) is gradually dissociated to OH⁻ by hexylamine as hexylamine concentration increases in the ink. This increase of the OH⁻ explains well the pH value increasing with hexylamine content in the ink, as shown in Figure 3.4. As a result, the bonding strength between Cu(II) cation and formate anion weakens with increasing hexylamine content in the ink and thus the reduction of Cu(II) cation, followed by the nucleation of metallic Cu is promoted. For a more direct analysis, in-situ FT-IR measurements of 1 : 1.0 and 1 : 4.0 inks

while heating from 100 °C to 200 °C in air were performed, as shown in Figure 3.13. In a graph, intensity denotes FT-IR absorbance intensity from organic species and time is the amount of time it takes to heat from 100 °C to 200 °C. The result shows that organic species are decomposed and disappear in a shorter time (faster) during heating in the ink with higher hexylamine concentration.

These results indicate that Cu nucleates with shorter nucleation time periods at lower temperature during thermal heating in the ink with higher hexylamine concentration, which support well the difference in thermal decomposition behavior and film microstructure which is found in the inks with different hexylamine concentrations, as confirmed earlier by TGA/ DSC and FE-SEM. In other words, as hexylamine concentration increases in the ink, temperature and period for thermal decomposition of the ink decrease and the produced Cu film reveals densely packed microstructure of smaller-sized Cu nanoparticles with narrower particle size distribution.

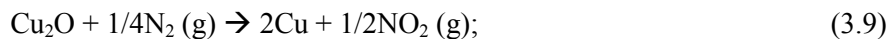
The electrical resistivities of each film are shown in Figure 3.14. The electrical resistivities of the Cu films prepared using 1 : 2.5 and 1 : 4.0 inks are magnified in the inset. The electrical resistivity of the printed Cu film decreased with increasing the hexylamine concentration in the ink, due to the increase in the film density. The resistivity also decreased gradually with aging time through the films, because of the increase in crystallite and particle size and the volatilization of organic residue. The 1 : 1.0 ink-printed films have the porous structure associated with the broad particle-size distribution. The films with such a low density led to the highest resistivity, despite the

large size of Cu particles constituted inside them. In contrast, the 1 : 4.0 ink-printed films have the highest density. Their resistivities were the lowest, despite the agglomeration of small Cu particles inside them and thus high density of grain boundary which acts as carrier scattering sites. It means that film density (specifically, packing density of the particles) is a dominant factor for determining the electrical conductivity. Finally, the lowest resistivity of $\sim 454 \mu\Omega\text{cm}$ was attained in 1 : 4.0 ink-printed film, heated for 60 min at 200 °C in N₂ atmosphere.

To obtain better electrical resistivity, the sintering of the Cu particles produced in the ink should be promoted. Generally, Cu sintering has been performed under N₂ and H₂ gaseous mixture in order to avoid oxidation during post heat treatment. However, the gaseous mixture cannot reduce the contaminated oxide scale or the oxide scale that already exists, because of the relatively slow reduction kinetics of H₂ gas, as the following reactions show.



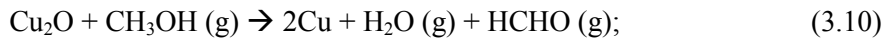
$$\Delta G(400 \text{ } ^\circ\text{C}) = -91 \text{ kJ}$$



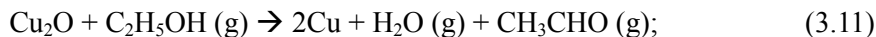
$$\Delta G(400 \text{ } ^\circ\text{C}) = 157 \text{ kJ}$$

Therefore, it is critical to develop a faster and more favorable reduction reaction atmosphere for printed Cu metallization. More candidates for reduction atmosphere were investigated and compared as shown in the

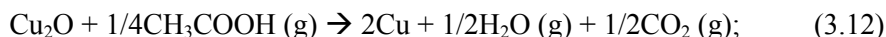
following reactions.



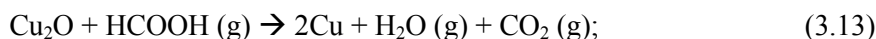
$$\Delta G(310 \text{ } ^\circ\text{C}) = -69 \text{ kJ}$$



$$\Delta G(310 \text{ } ^\circ\text{C}) = -87 \text{ kJ}$$



$$\Delta G(310 \text{ } ^\circ\text{C}) = -99 \text{ kJ}$$



$$\Delta G(310 \text{ } ^\circ\text{C}) = -161 \text{ kJ}$$

By considering the reaction free energy, a formic acid (HCOOH) was finally selected as a reductive atmosphere for the effective sintering of the ink-printed films. The 1 : 1, 1 : 2.5 and 1 : 4.0 ink-printed films were heated for 1 and 6 min at 200 °C in HCOOH, respectively. The cross-sectional FE-SEM micrographs of the films and XRD patterns (for 1 : 4.0 ink-printed films, representatively) are shown in Figure 3.15 and Figure 3.16, respectively. All the films showed pure polycrystalline Cu phase (Figure 3.16). The size and distribution of the produced particles decreased and film density increased with increasing the molar ratio of hexylamine to Cu(II) in the used ink, similarly to the case of sintering in N₂ atmosphere. However, larger particles

were formed in the films compared with that of particles produced in N₂ atmosphere. The 1 : 1.0 ink-printed film heated for 6 min consisted of the particles of ~3 μm in diameter and the 1 : 2.5 ink-printed films produced the particles of 45-90 nm and 365 nm when heated for 1 min and 6 min, respectively, although the less decomposed metal-organic complexes were shown instead of particles in the whole part of 1 : 1.0 ink-printed film and in the upper part of 1 : 2.5 ink-printed film, heated for 1 min, respectively. In particular, highly dense morphologies, compared with those sintered in N₂, were shown in 1 : 4.0 ink-printed films heated for both 1 and 6 min. In other words, more sintered and dense films were obtained in a reductive HCOOH atmosphere, indicating that HCOOH atmosphere is preferable for Cu sintering compared with N₂ or air. As a result, it is found that the reductive sintering using a formic acid (HCOOH) is indeed effective for increasing the film sintering regarding the particle growth and densification of highly packed small particles with high surface energy and thus increasing the electrical conductivity of the ink-printed Cu films. It is thought that the reductive atmosphere increased the surface diffusion of the particles by reduction of the contaminated oxide scale and thus increased the particle size.

During the reduction of Cu₂O to Cu by HCOOH, the generation of CO from HCOOH and its effect on the reduction can be in doubt. When Cu₂O is exposed under CO atmosphere, it reduces to Cu with the following reaction [25,26].



$$\Delta G = -27380 + 1.47T\ln T - 1.4 \times 10^{-3}T^2 + 0.5 \times 10^{-6}T^3 - 7.01T$$

When Cu₂O is exposed under H₂ atmosphere, it reduces to Cu with the following reaction.



$$\Delta G = -16260 + 2.21T\ln T + 1.28 \times 10^{-3}T^2 + 3.8 \times 10^{-7}T^3 - 24.768T$$

In comparison with two gaseous atmospheres at 200 °C where this experiment was performed, $\Delta G = -266.74$ kJ for CO and $\Delta G = -21.21$ kJ for H₂ are obtained. Therefore, CO gaseous atmosphere is more favorable for the reduction of Cu₂O to Cu, compared to H₂. The CO gas has higher reduction potential than HCOOH ($\Delta G = -161$ kJ at 310 °C). HCOOH gas reduces Cu₂O to Cu with the following reaction process [27].



Water vapor and CO₂ gas are generated during the reduction of Cu₂O to Cu by HCOOH. Accordingly, it is considered that there are no generation of CO from HCOOH and its effect on the reduction process.

Figure 3.17 exhibits the electrical resistivities of the films heated for 1 and 6 min at 200 °C in HCOOH atmosphere, respectively. The electrical resistivity of the formed films decreased with increasing film density (packing density of the particles) as the molar concentration ratio of hexylamine to

Cu(II) in the used ink increased, similarly to the case of the films sintered in N₂. The resistivities of all the films were lower than those of the films sintered in N₂, due to the improved sintering effect leading to enlarged particle size and densification. The lowest resistivity of ~40.5 $\mu\Omega\text{cm}$, which is an order of magnitude less than that of the film heated for 60 min in N₂, was achieved in the 1 : 4.0 ink-printed film heated for 6 min at 200 °C in HCOOH.

The reductive sintering of the ink-printed films in HCOOH atmosphere was further promoted by increasing the heating temperature. Figure 3.18 shows the cross-sectional microstructures of the films printed with 1:2 ink and then heated for 5 min at 170, 200 and 250 °C in HCOOH, respectively, observed by FIB-SEM. As the heating temperature increased, better necking and densification of the particles inside the film was observed, which resulted in the improvement of electrical conductivity of the film. The electrical resistivities of the films, printed with 1 : 2 ink and then heated for 2 and 5 min under HCOOH atmosphere were shown as a function of processing temperature in Figure 3.19. The films heated for 5 min exhibited lower resistivity than those heated for 2 min over all processing temperatures. The resistivity was not noticeably decreased as the aging time was extended beyond 5 min. The electrical resistivity decreased gradually with increasing the heating temperature through the heating time. In particular, the lowest resistivity of ~8 $\mu\Omega\text{cm}$ (electrical conductivity of ~125 000 Ωcm^{-1} , equivalent to ~22% of bulk Cu) was obtained for the films heated for 5 min at 250 °C. This resistivity was nearly 4.5 times higher than that of bulk Cu (1.76 $\mu\Omega\text{cm}$) and very low compared with the values reported under similar processing

temperatures in other studies [6,21-24].

The quantitative comparison of oxygen content in the films sintered under N₂ and HCOOH atmospheres was performed using X-ray photoelectron spectroscopy (XPS) in order to provide the evidence that the film sintering is promoted by removing the surface oxide scales of Cu particles constituting films under reductive HCOOH atmosphere. The ink-printed films were sintered for 5 min at 200 °C under each atmosphere for comparison. As shown in Figure 3.20, the Cu film sintered in HCOOH contained lower surface oxygen than that sintered in N₂. The surface oxygen detected in the Cu film sintered in HCOOH is considered to originate from exposure in air during treatment for the measurement of the sample. Therefore, it is clear that the film sintering is promoted by removing the surface oxide scales of Cu particles constituting films under reductive HCOOH atmosphere, in contrast to the inert N₂ used conventionally.

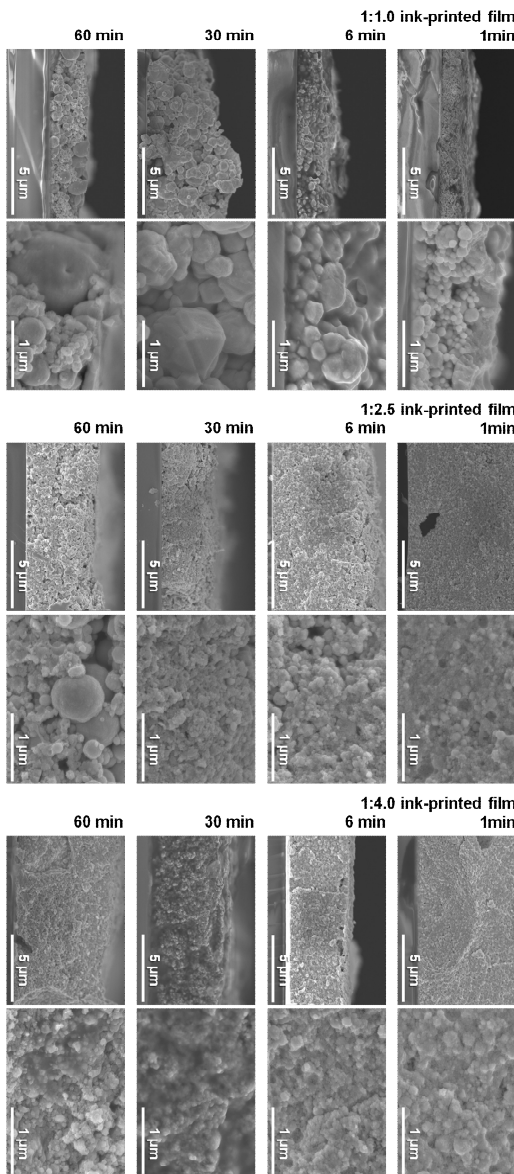


Figure 3.9. Cross-sectional FE-SEM micrographs of the films, printed with 1 : 1.0, 1 : 2.5 and 1 : 4.0 inks and then heated for different aging times at 200 °C in N₂ atmosphere, respectively.

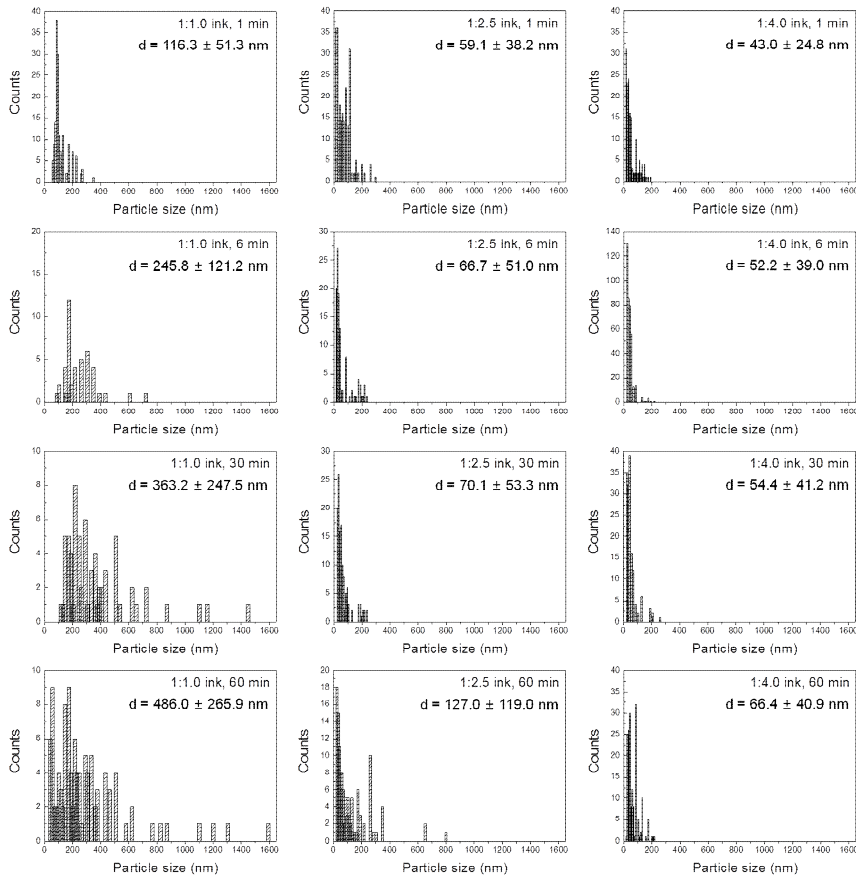


Figure 3.10. Particle size and distribution measured from the FE-SEM micrographs of Figure 3.9.

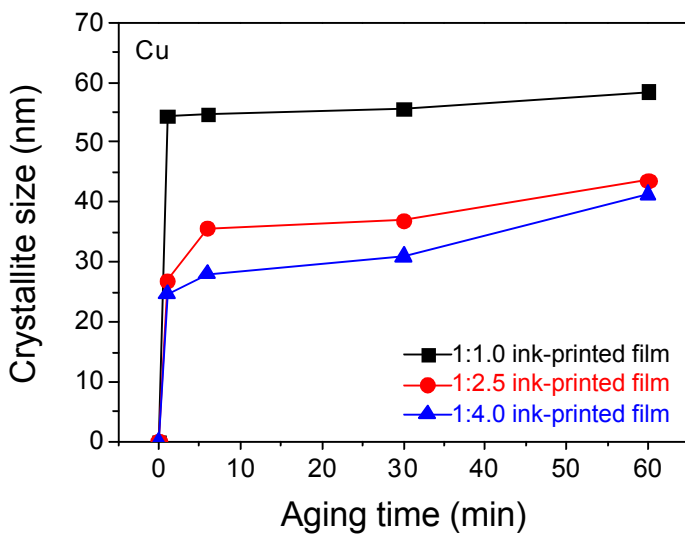


Figure 3.11. Crystallite sizes of the Cu films printed with 1 : 1, 1 : 2.5 and 1 : 4.0 inks and then heated at 200 °C in N₂ atmosphere, shown as a function of aging time.

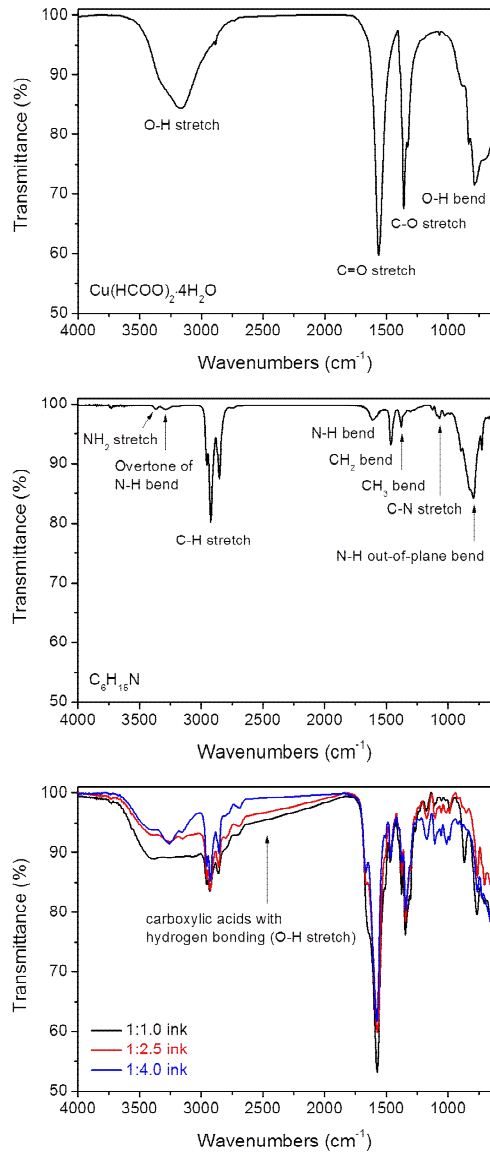


Figure 3.12. FT-IR spectra of Cu(II) precursor, hexylamine solvent, and the formulated inks, investigated at room temperature.

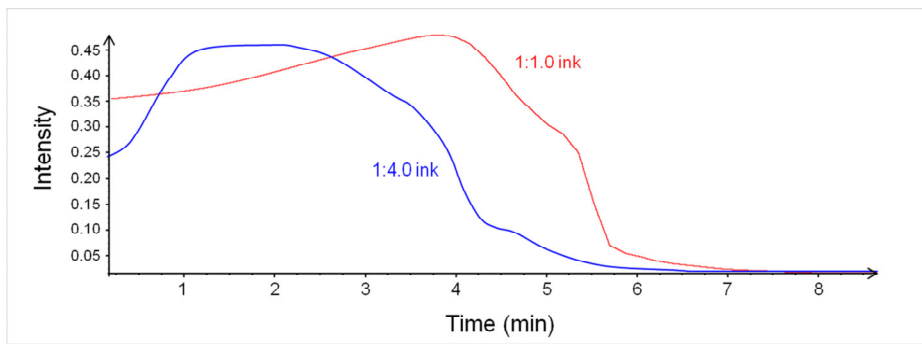


Figure 3.13. in-situ FT-IR measurements of 1 : 1.0 and 1 : 4.0 inks while heating from 100 °C to 200 °C in air.

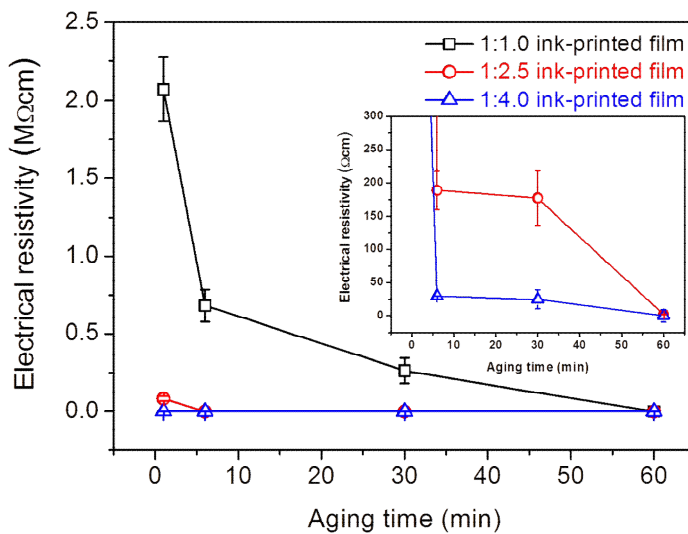


Figure 3.14. Electrical resistivity of the Cu films printed with 1 : 1, 1 : 2.5 and 1 : 4.0 inks and then heated at 200 °C in N₂ atmosphere, shown as a function of aging time. The inset shows the magnification of the electrical resistivity of the Cu films prepared using 1 : 2.5 and 1 : 4.0 inks.

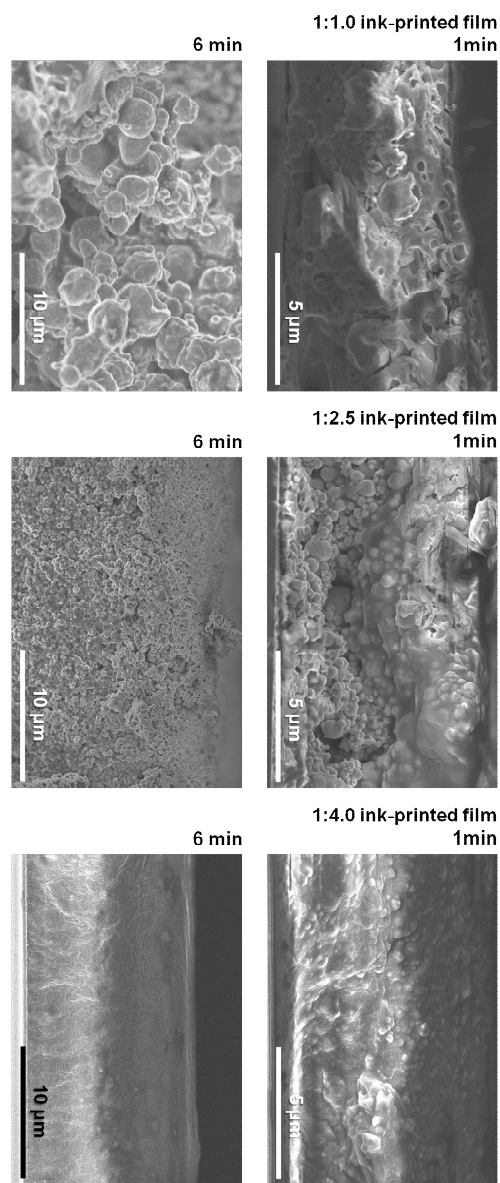


Figure 3.15. Cross-sectional FE-SEM micrographs of the films, printed with 1 : 1.0, 1 : 2.5 and 1 : 4.0 inks and then heated for different aging times at 200 °C in HCOOH atmosphere, respectively.

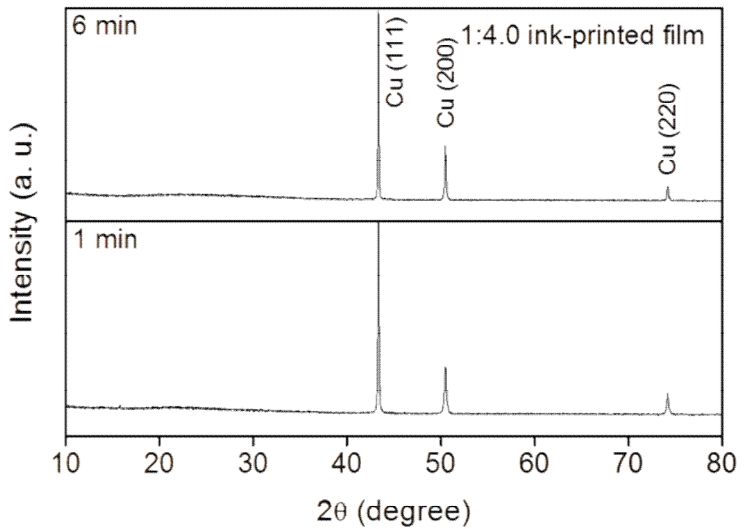


Figure 3.16. XRD patterns of the 1 : 4.0 ink-printed films heated for 1 and 6 min at 200 °C in HCOOH, respectively.

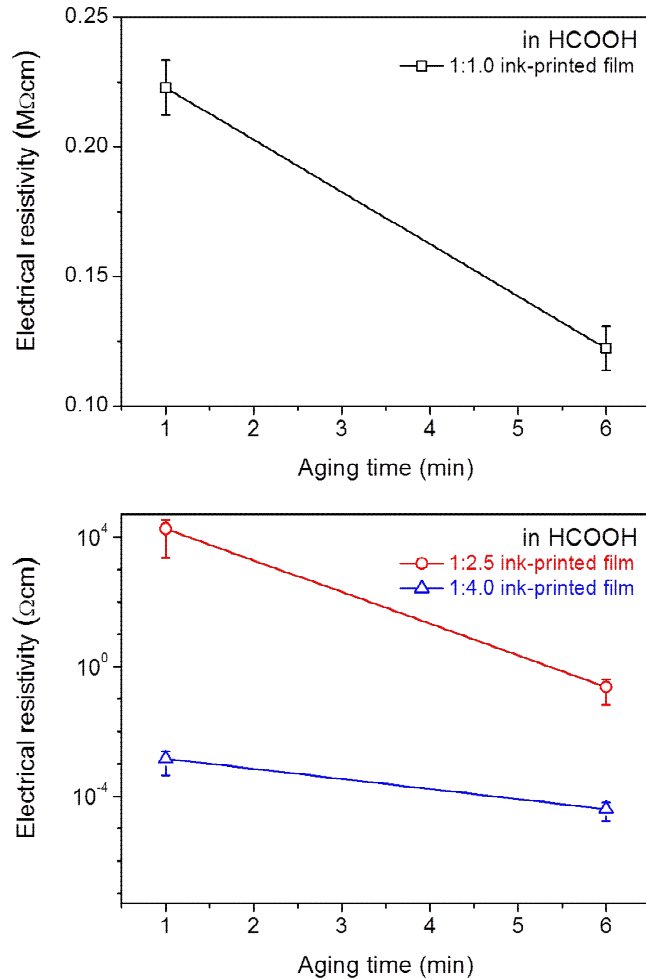


Figure 3.17. Electrical resistivity of the Cu films printed with 1 : 1, 1 : 2.5 and 1 : 4.0 inks and then heated for 1 and 6 min at 200 °C in HCOOH atmosphere, respectively.

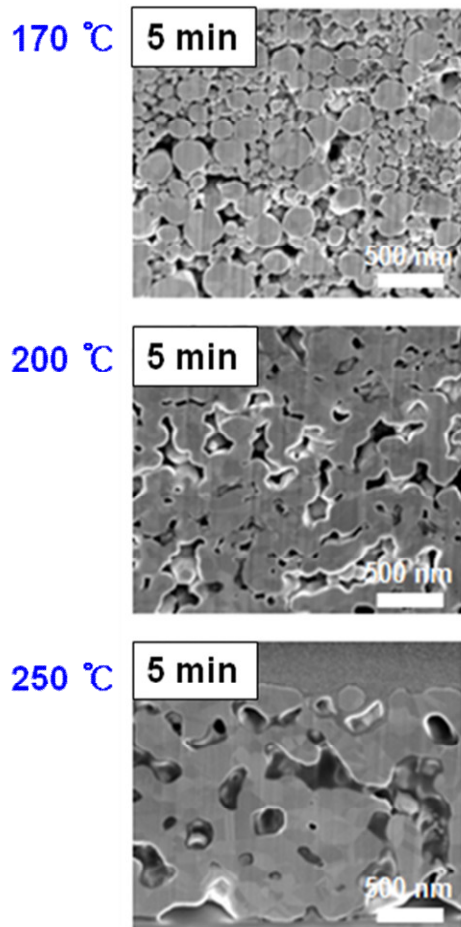


Figure 3.18. Cross-sectional views of the films printed with 1:2 ink and then heated for 5 min at 170, 200 and 250 °C in HCOOH, respectively, observed by FIB-SEM.

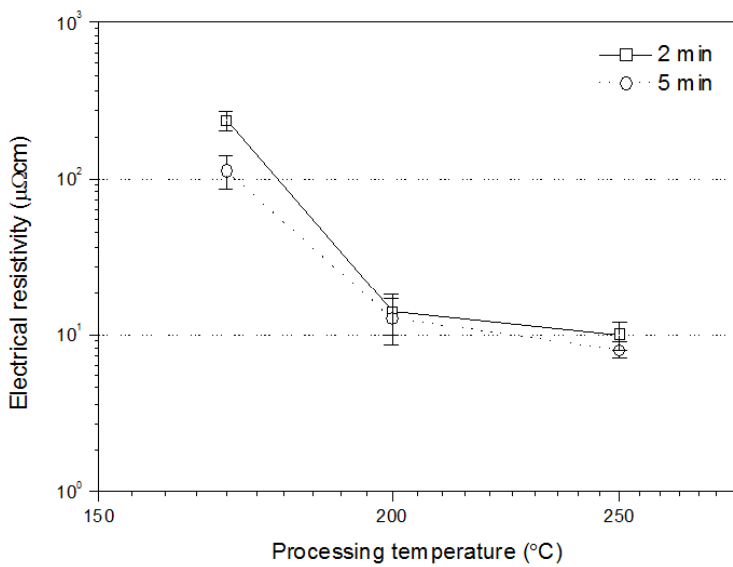
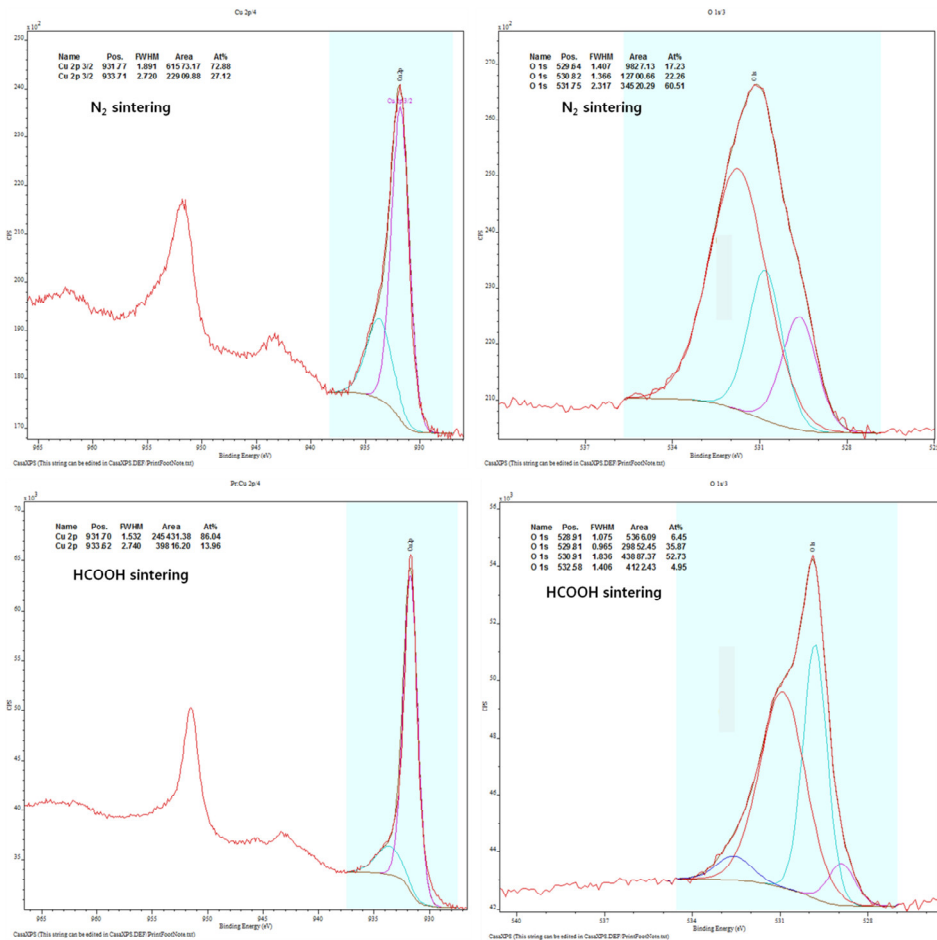


Figure 3.19. Electrical resistivity of the films, printed with 1 : 2 ink and then heated for 2 and 5 min under HCOOH atmosphere, shown as a function of processing temperature.



	Peak	Type	Position BE (eV)	FWHM (eV)	Raw Area (cps eV)	PSF	Atomic Mass	Atomic Conc %	Mass Conc %
N ₂ sintering	O 1s	Reg	5302	2958	175858	0.711	15999	7613	4454
	Cu 2p	Reg	9508	2442	277377	5321	63549	2387	5546
HCOOH sintering	O 1s	Reg	5283	211	262987	0.711	15999	5989	2732
	Cu 2p	Reg	9499	166	889291	5321	63549	4011	7268

Figure 3.20. XPS spectra of Cu 2p and O1s and their quantitative comparison in the films sintered for 5 min at 200 °C under N₂ and HCOOH atmospheres.

3.6 Cu metallization optimized

To begin with, the effect of the molar ratio of hexylamine solvent to precursor (Cu(II)) in the ink on microstructure of the ink-printed films was investigated in terms of nucleation and growth of Cu particles. The size and distribution of particles produced inside the ink-printed film decreased and the film density (packing density of the particles) increased during thermal heating, due to the increasing nucleation rate with shorter nucleation time periods, as the molar concentration ratio of hexylamine increased. As a result, the electrical conductivities of films were enhanced. Secondly, sintering of the ink-printed films under a reductive HCOOH atmosphere was promoted due to the increased surface diffusion of Cu particles, resulting in the particle growth and densification and thus the improved electrical conductivity of films. Finally, sintering of the ink-printed films was further promoted by increasing the heating temperature, leading to the enhancement of necking and densification of particles and thus improved electrical conductivity of films.

Based on these results, the printed Cu metallization was finally optimized. The FIB-SEM cross-sectional micrographs of 1 : 1.0, 1 : 2.5, and 1 : 4.0 ink-printed films heated for 2, 5, and 10 min at 250 °C under a reductive HCOOH atmosphere are shown in Figure 3.21. Porosity was measured as being ~10 % and ~40 % for 1 : 4.0 and 1 : 1.0 ink-printed films, respectively. As a consequence, the lowest electrical resistivity of ~5.2 $\mu\Omega\text{cm}$ (electrical conductivity, equivalent to ~33.8% of bulk Cu) was obtained in the 1 : 4.0 ink-printed film heated for 10 min at 250 °C in HCOOH throughout this study.

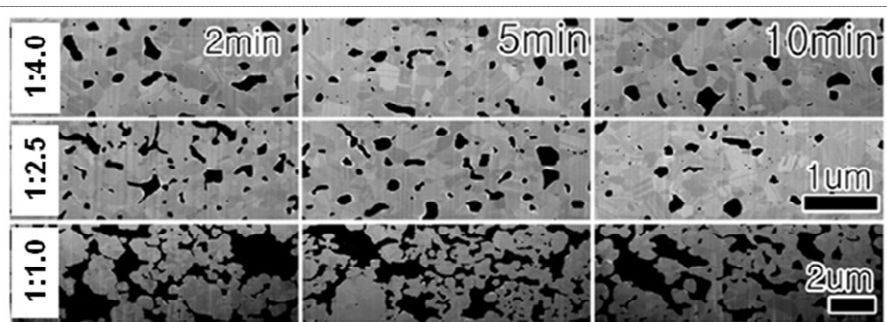


Figure 3.21. FIB-SEM cross-sectional micrographs of 1 : 1.0, 1 : 2.5, and 1 : 4.0 ink-printed films heated for 2, 5, and 10 min at 250 °C under a reductive HCOOH atmosphere.

4. Controlled Preparation of Ink-Printed Copper Oxide Films for Applications in Gas sensor and Photoelectrochemical Water Splitting

4.1 Opening remarks

Pure oxide phase with high specific surface area should be formed for successful printing fabrication of functional devices such as gas sensor and photoelectrochemical cell besides metallization. Therefore, the printed films with 1 : 1.0, 1 : 2.5 and 1 : 4.0 inks were oxidized for 1, 6, 30 and 60 min at 200 °C in air, respectively, and their phases were investigated by XRD, as shown in Figure 4.1. All the films consisted of the mixed phase of Cu and Cu₂O within a given time. Figure 4.2 shows the peak intensity ratio ($I(Cu_2O)/I(Cu)$) between Cu and Cu₂O based on the XRD peaks. As the molar concentration ratio of hexylamine to Cu(II) in the printed ink increased, both oxidation rate and oxide amount in the films increased, due to decreased size of Cu particles inside the film. However, perfectly pure oxide phase in the films was hard to be obtained at the temperature as low as 200 °C in air. To prepare pure oxide, very long aging time or higher oxygen partial pressure are required, but such works will produce the oxide films with still low crystallinity at the low temperature and will be effective only in the 1 : 4.0 ink-printed film consisting of the small Cu particles, with the high oxidation

capability, as shown in Figure 4.2.

In this study, two strategies are suggested and tried to obtain pure oxide phase with high specific area in the films for applications in gas sensor and photoelectrochemical device. First, mesoporous/porous thin films with reduced thickness are formed using 1 : 4 ink and subsequently calcined and oxidized at high temperatures up to 600 °C in air. Second, direct printing synthesis of copper oxide hollow spheres on substrates is realized for the first time through only thermal heating of 1 : 1 ink-printed film in air, demonstrating the successful fusion of printing technology and nanotechnology. This is a very facile, scalable, template-free, and one-pot method, leading to the high-throughput fabrication of high-performance devices.

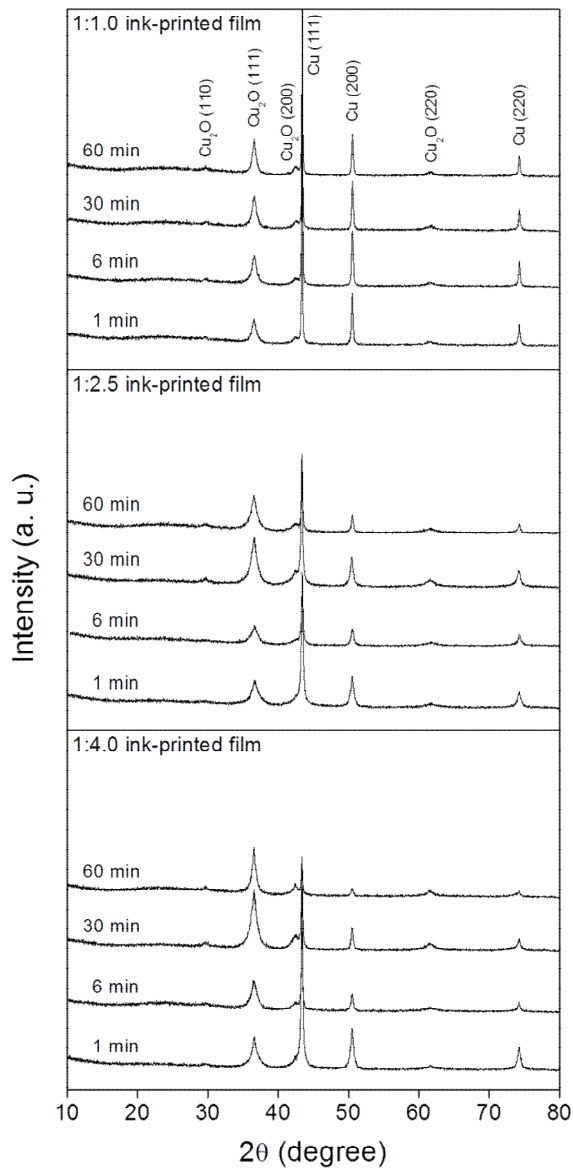


Figure 4.1. XRD patterns of the ink-printed films heated for 1, 6, 30 and 60 min at 200 °C in air, respectively.

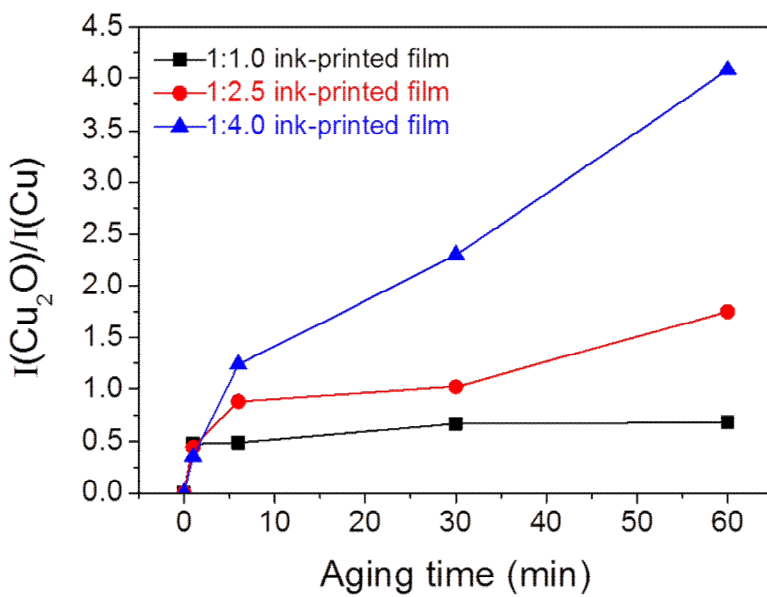


Figure 4.2. Evolution of the peak intensity ratio ($I(\text{Cu}_2\text{O})/I(\text{Cu})$) between XRD peaks of Cu and Cu_2O of each film, shown in Figure 5.1, with aging time.

4.2 Direct printing synthesis of CuO mesoporous/porous thin films

4.2.1. Experimental

4.2.1.1. Ink formulation and film coating

The ink solution was formulated with copper(II) formate hydrate ($\text{Cu}(\text{HCOO})_2 \cdot n\text{H}_2\text{O}$; 97% purity; Sigma-Aldrich), hexylamine ($\text{C}_6\text{H}_{15}\text{N}$; 99% purity; Sigma-Aldrich) and ethyl cellulose (9-11 mPa·s, 5% in toluene + ethanol (80:20) at 25 °C; Tokyo Chemical Industry Co., LTD.) dissolved in 1-methyl-2-pyrrolidinone (NMP; 99% purity; Sigma-Aldrich). The chemicals purchased were used without further purification. The Cu content (27.3 ± 0.8 wt%) in the commercial precursor measured by inductively coupled plasma atomic emission spectroscopy (ICP-AES; ICPS-8100; Shimadzu) indicated that the $\text{Cu}(\text{HCOO})_2$ is coordinated by tetrahydrate ($n=4$). To prepare the ink solution, the copper(II) formate tetrahydrate powder dissolved in hexylamine with a mole ratio of 1:4 and ethyl cellulose equivalent to 8.5 wt% of Cu was added. Subsequently, this was stirred with a magnetic stick bar for 24 h in air and a homogeneous transparent dark-blue ink solution was obtained. The Cu content in the final ink solution, analyzed by ICP-AES, was 9.5 ± 0.3 wt%. All the procedures were performed at room temperature (RT). The shear viscosity of the ink solution was confirmed as $5.79 \text{ Pa}\cdot\text{s}$ at a shear rate of 1 s^{-1} by a rheometer (AR2000; TA Instruments).

In order to form mesoporous CuO films, the ink solution was spin-coated

(2000 rpm, 1 min) on SiO₂ (2000 nm)/Si substrates, followed by calcining thermally for 1 h at 200-600 °C in air with heating rates of 5 °C min⁻¹ using a tube furnace.

4.2.1.2. Characterization and gas-sensor measurement

Phases of the films were investigated by the grazing-incidence X-ray diffraction θ-2θ method (XRD; X’Pert Pro MPD; PANalytical) using Cu K_α radiation ($\lambda = 0.154$ nm). The surface and cross-sectional morphologies of the films were observed by a dual-beam focused ion beam scanning electron microscopy (FIB-SEM; Helios 400S; FEI) with a voltage of 30 kV and a current of 0.28 nA for FIB fine milling. The chemical compositions of each film were examined by energy-dispersive X-ray spectroscopy (EDX) provided in the same machine. In order to calculate the surface and cross-sectional porosities of the films from the SEM images, solid (white)/pore (black) binary 2-dimensional images were analyzed by simple computer-programming. The chemical bonding information near the film surfaces was examined by X-ray photoelectron spectroscopy (XPS; AXIS-HSi; KRATOS) with a Mg K_α radiation (1253.6 eV). The core level XPS spectra for O1s and Cu2p were measured and energy calibration was achieved by setting the hydrocarbon C1s line at 284.5 eV.

In regards to the gas sensing measurements, a pair of comb-like Pt electrodes was formed on CuO films by sputtering through a mask. Each sample was subsequently fired for 1 h at the same temperature as the calcined

one in air to increase crystallinity of the electrodes. No change in morphology or phase of each film was observed for the additional firing. Thereafter, Au wires were attached to them using a Ag paste, followed by drying at 80 °C in a conventional oven. The sensors were placed in a quartz tube located inside an electrical tube furnace with a gas inlet and outlet. The nozzle diameter of the quartz tube was 3.6 cm (4.0 cm, the total diameter including the walls) and its total length was 60 cm (20 cm, the distance between gas inlet and outlet). The H₂ and C₂H₅OH sensing characteristics were determined by measuring the changes in electric resistance between 100 and 1000 ppm gas balanced with air and pure air at 200-500 °C. The electrical resistance was measured using a multimeter (Keithley 2002). The magnitude of the gas response was defined as the ratio (R_g/R_a) of the resistance in air (R_a) to that in a target gas (R_g), and the response time ($t_{90\%}$) was defined as the time required for the sensor to reach 90% of the final signal. The ratio of gas responses was defined as the ratio of the resistance in H₂ to that in C₂H₅OH. It was confirmed by SEM and XRD studies that the morphology and phase of each CuO sensor were maintained constantly for the gas sensor measurements.

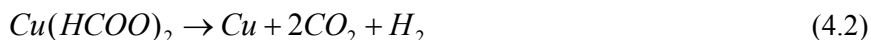
4.2.2. Results and discussion

4.2.2.1. Ink-to-film transformation by thermal calcination

The thermal decomposition of the formulated ink was investigated in detail by thermogravimetric analysis (TGA) and differential scanning calorimetry (DSC) in previous chapter. To begin with, the dehydration of Cu(HCOO)₂·4H₂O in the ink proceeds up to near 115 °C. Secondly, at 140-173 °C, hexylamine volatilizes. However, the volatilization of the hexylamine occurs at the temperature range higher than its boiling point (130 °C), because amine groups are coupled with formates of the anhydrous Cu(HCOO)₂. The resulting chemical products were confirmed as 5-ethyl-2-methyl piperidine (boiling point = 160 °C) and N-1-hexylformamides (boiling point = 245 °C) by pyrolysis gas chromatography mass spectrometry (Py-GC/MS) analysis. Finally, the dissociation of the formate group from the anhydrous Cu(HCOO)₂ occurs at 173-240 °C. Its chemical reductive dissociation is as follows.



or



The reduction from the anhydrous Cu(HCOO)₂ into metallic Cu at 173-

240 °C involves stepwise cation reduction, $\text{Cu}^{2+} \rightarrow \text{Cu}^+ \rightarrow \text{Cu}^0$. In addition, the vaporization of NMP proceeds at its boiling point (202-204 °C). Ethyl cellulose, polymer additive, is decomposed and vaporized completely near 400 °C.

The thermal decomposition of the ink, described above, occurs as temperature increases continuously with heating rates of 5-10 °C min⁻¹. If the calcination/sintering of the ink coats proceeds constantly for more than a few minutes at static temperatures, hexylamine, amine-formate complexes and NMP contained in the ink can be completely volatilized and pure Cu can be formed even at 170-250 °C which is the temperature range lower than the volatilization and dissociation temperatures, confirmed above, except for ethyl cellulose.

The metallic Cu formed is oxidized subsequently to Cu_2O and finally to CuO during calcination in air. The oxidation of the Cu proceeds by the following reactions.



Therefore, in this work, the films coated with the ink based on copper formate-amine complex and polymer additive could be transformed successfully into CuO films with a mesoporous form by thermal calcinations for 1 h at 200-600 °C in air.

4.2.2.2. Structural characteristics

Mesoporous CuO films were formed on SiO₂/Si substrates by spin-coating with the formulated ink solution and then calcining for 1 h at a temperature ranging from 200 to 600 °C, and their grazing-incidence XRD patterns were shown in Figure 4.3. Since stronger peaks indicate higher crystallinity, the crystallinity of the film was improved with increasing calcination temperature while consisting of polycrystalline CuO, based on the CuO powder diffraction pattern (JCPDS # 00-045-0937) (Figure 4.3(a)). Due to thermal vaporization of the ethyl cellulose finishing near 400 °C as well as insufficient thermal energy for crystallization, the crystallinities of the films calcined from 200 to 400 °C were incomplete. In contrast, the films calcined above 500 °C exhibited superior crystallinity. The average full width at half maximum (FWHM) for each (002) and (111) peak was shown as a function of calcination temperature in Figure 4.3(b). The FWHM decreased as calcination temperature increases, indicating a larger grain size at a higher calcination temperature. In particular, the (111) peaks in the CuO films were gradually predominant over (002) with an increasing calcination temperature, unlike the powder diffraction pattern.

The surface morphologies of the CuO films, with the superior crystallinity, calcined at 500 and 600 °C, respectively, were compared by FIB-SEM in Figure 4.4(a) and (b). All the films showed porous structures, which were induced by evolution of the empty spaces between the highly packed small particles produced during thermal heating of the coated ink. The ethyl cellulose played very significant roles in preventing shrinkage, dewetting and delamination of the coated films during heat treatment by promoting the adhesion with substrates. The amount of ethyl cellulose in the ink was experimentally optimized as ~8.5 wt% of Cu, maximizing the metal content in the ink while maintaining good coatability of the ink. The film calcined at 500 °C showed the average grain size diameter of 30 ± 10 nm and relatively small pore sizes of ~10 nm width, while that calcined at 600 °C represented relatively large faceted grain diameters of 63 ± 20 nm and larger pore sizes over 50 nm width (Figure 4.4(a) and (b)). The enlarged grain and pore sizes in the film calcined at 600 °C were attributed to the sintering effect promoted at its higher calcination temperature. The pore-width sizes below 50 nm observed in the film calcined at 500 °C indicated that the film had a ‘mesoporous’ structure, according to the definition in the previous literature [1]. The cross sections of both films were investigated by FIB fine milling (Figure 4.4(c) and (d)). Pt was fully coated on all the films by sputtering to utilize the cross-sectional FIB-SEM (Figure 4.5(a)). Both films exhibited the same thickness of ~200 nm and vermicular cross-sectional structures. Instead of grain boundaries, the clusters that a few grains assembled were observed in the cross-sections after FIB processing. In particular, the film calcined at

600 °C consisted of larger clusters compared to those calcined at 500 °C. In order to deduce the surface-to-volume ratio for both films, the surface and cross-sectional porosities were compared by image analysis in Figure 4.4(e). The surface porosity (18.29%) of the film calcined at 500 °C was lower than that (28.12%) of the film calcined at 600 °C, whereas the cross-sectional porosity (29.28%) of the film calcined at 500 °C was higher than that (19.98%) of the film calcined at 600 °C. Such lower surface porosity (higher solid surface area) and higher cross-sectional porosity of the film calcined at 500 °C demonstrated a higher surface-to-volume ratio than the film calcined at 600 °C. For comparison, the surface (see Figure 4.5(b)) and cross-sectional morphologies, surface (18.59%) and cross-sectional (29.35%) porosities, and thickness of the film calcined at 400 °C were further investigated and consequently, were roughly similar to those of the film calcined at 500 °C, although grain and pore sizes were slightly smaller. However, the film had relatively poor crystallinity, resulting from insufficient thermal energy, even though polymer residue was not observed by EDX analysis, as showing no C peak in Figure 4.5(c). The EDX analysis results of the films calcined at 400, 500 and 600 °C, respectively, showed that the chemical compositions coincide with CuO films formed on SiO₂/Si substrates.

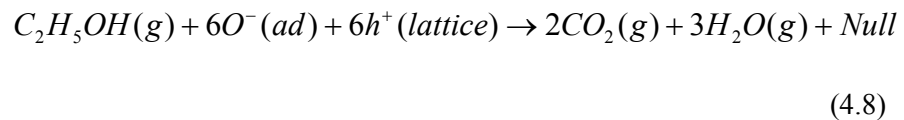
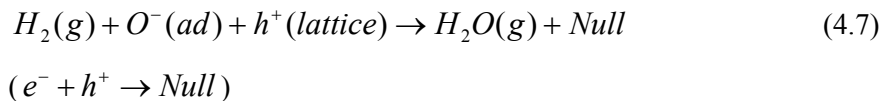
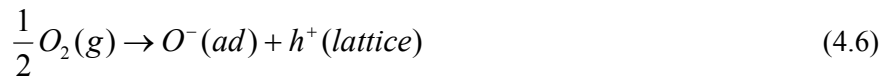
The surface chemical compositions of each film were further investigated by XPS and the core level Cu2p spectra of the films were shown with Cu2p_{3/2} and Cu2p_{1/2} peaks due to spin-orbit splitting of Cu2p in Figure 4.6 [2]. The Cu2p_{3/2} peaks located at 933.83, 933.68 and 933.47 eV, in the film calcined at 400, 500 and 600 °C, respectively, are in good agreement with the values

(933.2-933.9 eV) for the lattice copper(II) of CuO [3-5]. The Cu $2p_{1/2}$ peaks are observed at 953.93, 953.62 and 953.37 eV in the film calcined at 400, 500 and 600 °C, respectively. In particular, the shake-up satellite peaks of the Cu $2p_{3/2}$ and Cu $2p_{1/2}$ in all the films occurred near 942.5 and 962.5 eV, respectively, which provide clear evidence of an open 3d⁹ shell of copper(II) in CuO [6]. Furthermore, the doublet structures shown in the Cu $2p_{3/2}$ satellite peaks (~942.5 eV) indicate that the cupric states are well maintained in all the films even in the outermost layers [3,7].

4.2.2.3. Gas sensing properties

Gas sensing properties of the mesoporous/porous CuO films calcined at 400, 500 and 600 °C, respectively toward 100-1000 ppm H₂ and C₂H₅OH balanced with air were measured in the operating temperature range from 200 to 500 °C. The stable and reversible response transients of the mesoporous CuO film calcined at 500 °C toward 1000 ppm H₂ and C₂H₅OH measured at 300 °C are shown in Fig. 4.7(a) and (b), respectively. The typical p-type character that the electrical resistance is increased to both reducing gases was detected. Gas responses (R_g/R_a) for each sensor toward 1000 ppm H₂ were exhibited as a function of operating temperature in Fig. 4.8(a). The CuO films calcined at 400 and 600 °C showed the maximum H₂ responses of 1.5-1.9 at 400 °C, whereas that calcined at 500 °C represented the highest response of 25 at 300 °C. The H₂ responses of the film calcined at 400 °C were inferior to the others throughout the operating temperature. In contrast, the film calcined

at 500 °C showed superior H₂ responses in comparison to the others throughout the operating temperature. Fig. 4.8(b) shows 1000 ppm C₂H₅OH responses of the films measured at 300 and 400 °C. Also, the film calcined at 500 °C displayed superior responses throughout the operating temperature with the highest response of 15 at 300 °C. In particular, gas responses toward C₂H₅OH were superb, compared with those toward H₂, throughout the sensor except for that regarding the film calcined at 500 °C measured at 300 °C. It is thought that the difference in the response between both gases, inducing gas selectivity, is due to the difference in the chemical dissociation of the gases on the surface of CuO. The atmospheric oxygen molecule is adsorbed in the form of an oxygen ion on the oxide surface (Eq. 4.6). When the CuO is exposed upon H₂ (Eq. 4.7) and C₂H₅OH (Eq. 4.8) gases, the chemical reactions for each reducing gas on the oxide surface are as follows.



The electrical resistances increase under both reducing gases, due to the

nullification of the holes, major carriers of the p-type semiconductor. Particularly, the adsorption of C_2H_5OH contributes to a greater nullification of the six holes, in comparison with that of H_2 leading to the nullification of a single hole. This seems to be the reason why gas response toward C_2H_5OH is higher than that toward H_2 . In each sensor, the ratio of gas responses, which is defined as the ratio of the resistance in 1000 ppm H_2 to that in 1000 ppm C_2H_5OH , was compared in the operating temperatures of 300 and 400 °C (Figure 4.9). The film calcined at 500 °C exhibited the maximum selectivity of 3.24 at 400 °C.

The concentration dependence of the gas response was investigated with the log-log plot in the ranges of 100-1000 ppm H_2 and C_2H_5OH at 300 °C, respectively (Figure 4.8(c) and (d)). The film calcined at 500 °C placed first in regards to the responses toward both H_2 and C_2H_5OH gases for all gas concentrations, that calcined at 600 °C came second, followed by that calcined at 400 °C. The gas response toward H_2 of the film calcined at 500 °C demonstrated a sudden elevation toward 1000 ppm H_2 , whereas the others exhibited linear concentration dependence with slightly different slopes, indicating the power law nature of the sensing response [8]. The gas responses toward C_2H_5OH were linearly dependent on the gas concentration throughout the sensor. The concentration dependences investigated at 400 °C were further shown in Figure 4.8(e) and (f). All of them exhibited a somewhat linear dependence on both H_2 and C_2H_5OH concentrations. By considering the slopes, the concentration dependence of the gas response was strengthened in a better sensor and was noticeably affected by the calcination temperature of

the film and target gas species rather than the operating temperature. Though roughly linear dependence on the gas concentration was observed in most cases, the slightly increased responses beyond the linearity were detected under 1000 ppm gases. Therefore, it is thought that the highly nonlinear response behavior of the film calcined at 500 °C, to 1000 ppm H₂ at the operating temperature 300 °C, was based on the maximization of true character regarding these CuO sensors. Since this led to the highest response value toward H₂ gas, further investigation correlating such a structural singularity with a chemical reaction is strongly required.

Response time ($t_{90\%}$) to 1000 ppm H₂ was investigated as a function of operating temperature and shown in Figure 4.8(g). The $t_{90\%}$ was reduced with increasing operating temperature in all the sensors. The fastest responses ($t_{90\%} = 4-8$ s) were achieved at the operating temperature 400 °C. The film calcined at 600 °C exhibited the fastest responses as opposed to the slowest responses of that calcined at 400 °C. The $t_{90\%}$ values to 1000 ppm C₂H₅OH showed similar trends to those to H₂.

First of all, we investigated the initial stand-by d. c. electrical resistances in air (R_a) for each CuO film as a function of operating temperature in order to explain the results of gas sensitivity and response time for each sensor (Figure 4.8(h)). Such an approach is reasonable since the p-type semiconducting property of CuO is induced by the hopping process of the holes, formed by the copper ion vacancies activated thermally in the nonstoichiometric Cu_{1-x}O [9]. Jeong and Choi [10] reported that the resistance of CuO increases with increasing its sintering temperature, attributed to the decrease of the copper-

vacancy density and the resulting decrease of hole carrier concentration in spite of the improvement for crystallinity, indicating a negative enthalpy of the defect generation reaction. In our case, the R_a of the film calcined at 400 °C was slightly higher than that calcined at 500 °C through the operating temperature. This agrees well with the report of Hoa et al. [11]. According to their report, the resistance of CuO is governed by its crystallinity for the calcinations under 500 °C. Additionally, in our case, the morphological factors such as grain/pore size, porosity and surface-to-volume ratio of the film calcined at 400 °C were roughly similar to those of the film calcined at 500 °C, as previously mentioned. Therefore, slightly higher resistance of the film calcined at 400 °C is merely due to its poor crystallinity, confirmed by the XRD pattern in Figure 5.3, without the morphological influence. Because the nonstoichiometry of $Cu_{1-\delta}O$ contributes to conduction better in the higher crystallinity matrix [11], the poor crystalline film calcined at 400 °C showed the worst gas sensitivity and response time. On the other hand, the lowest resistances of the film calcined at 500 °C result from both the improved crystallinity in comparison to the film calcined at 400 °C and the higher hole carrier concentration due to the higher density of copper vacancy compared to the film calcined at 600 °C. In addition, the film calcined at 500 °C has the highest surface-to-volume ratio. These explain why its gas responses were the highest. These also imply that the hole carrier concentration of the oxide is very significant together with the crystallinity and surface-to-volume ratio in this p-type gas response. Therefore, the moderate synthesis/calcination/sintering/processing temperature, maximizing the hole

concentration while maintaining high crystallinity and surface-to-volume ratio, is a key factor for the highly responsible p-type CuO gas sensor. The film calcined at 600 °C showed the highest resistance despite its best crystallinity, attributed to the poor carrier concentration. However, the resistance of the film can be decreased by the reduction of the grain boundary density, working as the conduction barrier of the carriers, which resulted from the grains grown by increasing the calcination temperature of the film from 500 to 600 °C. In regards to this, Hoa et al. [11] demonstrated that the resistance of CuO, increasing with an increase of the synthesis temperature above 500 °C, is namely caused by the reduced copper vacancy density and enhanced crystallinity and that the resistance reduction by the enlarged grain/crystallite size reveals a relatively small contribution to total resistance change at synthesis temperatures above 500 °C. Similarly, it was most recently reported that the carrier (the donor in n-type) action could dominate over grain boundary scattering for resistivity control in the n-type ZnO system [12]. Herein, we consider that both the excellent crystallinity and the low grain boundary density of the film calcined at 600 °C led to the fastest responses in the sensor, despite its lower surface-to-volume ratio. It was noticeably seen that the response time is inversely dependent on the hole concentration unlike the response or sensitivity in these p-type gas sensors. This is particularly understandable because the increase of hole concentration is due to increased generation of the defects acting as carrier trapping sites. Hence, the enhancements of the crystallinity, stoichiometric composition and the reduction of the carrier scattering/trapping sites such as grain boundary and

point defect are important factors for the rapidly responsible p-type CuO gas sensor.

The gas responses of our sensor were compared with those reported in the literatures based on the pristine CuO sensors for H₂ and C₂H₅OH detections in Table 4.1. As a result, the responses toward H₂ and C₂H₅OH gases of the mesoporous CuO films prepared in this work are comparable to the values previously reported. Most of all, the superior p-type responses toward H₂ gas of our sensor are worthy of note, even though they are still unsatisfactory compared with the conventional n-type sensors.

4.2.3. Conclusions

In conclusion, the novel precursor-type ink solution was formulated and used for the facile preparation of mesoporous p-type CuO sensing films. The mesoporous CuO film calcined for 1 h at 500 °C in air revealed the best H₂ and C₂H₅OH sensing characteristics, attributed to sufficient hole concentration, good crystallinity and the highest surface-to-volume ratio. The film calcined at 600 °C exhibited the fastest response time, due to both the excellent crystallinity and the low grain boundary density. These results obtained using neat CuO provide the right direction for the development of a high-performance p-type gas sensor. Furthermore, the novel ink solution route used for fabricating the mesoporous structure in this work can provide the realization of the printed sensor devices as well as the facile approach for ion doping or alloying in oxides to improve the sensor performance.

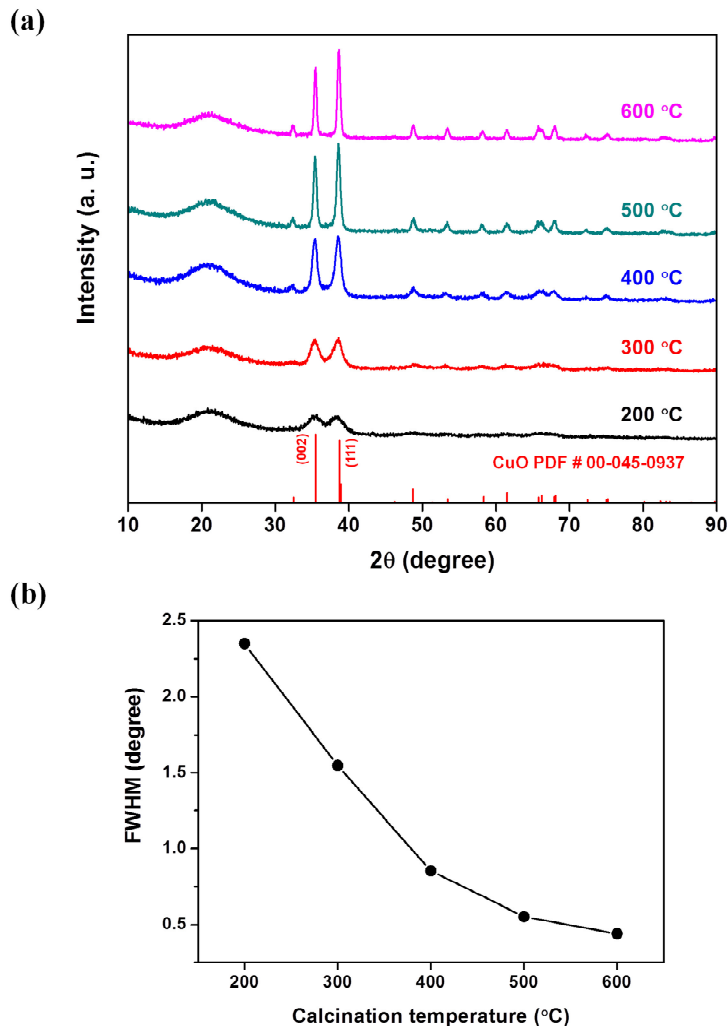


Figure 4.3. (a) Grazing-incidence XRD patterns of the mesoporous CuO films, calcined for 1 h at 200-600 °C in air after being spin-coated on SiO₂/Si substrates with an ink solution. (b) FWHM shown as a function of calcination temperature. They were deduced from the XRD patterns of the films.

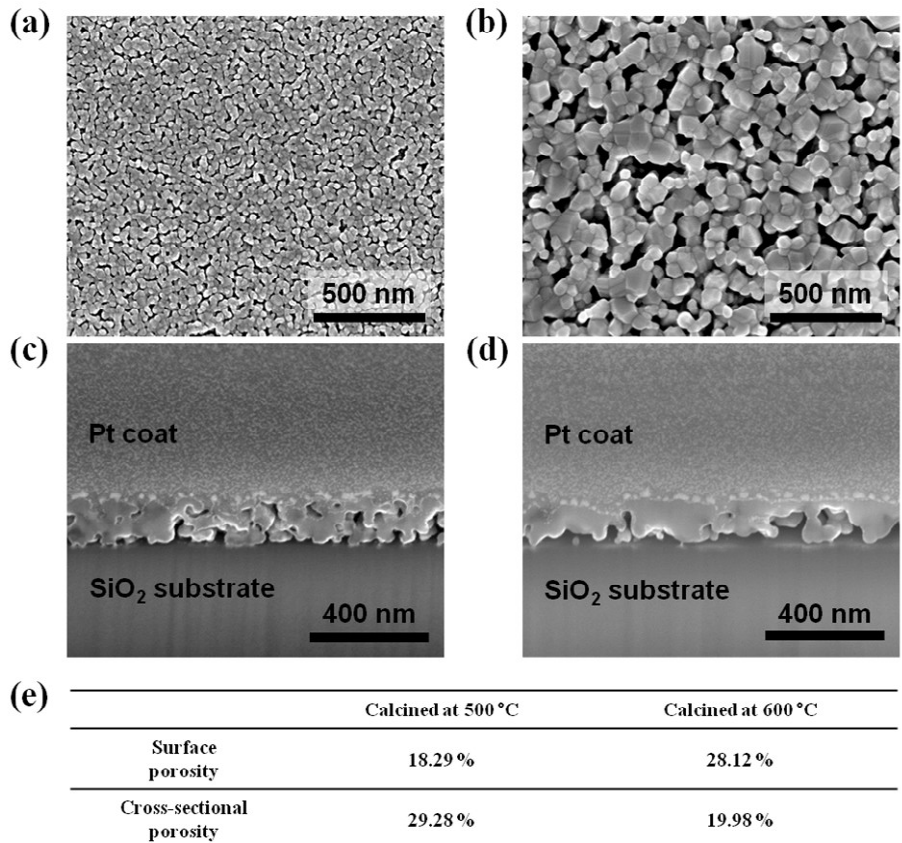


Figure 4.4. The surface SEM images of the mesoporous CuO films calcined at (a) 500 and (b) 600 °C, respectively. The cross-sectional SEM images of the CuO films calcined at (c) 500 and (d) 600 °C, respectively. (e) The surface and cross-sectional porosities of both films.

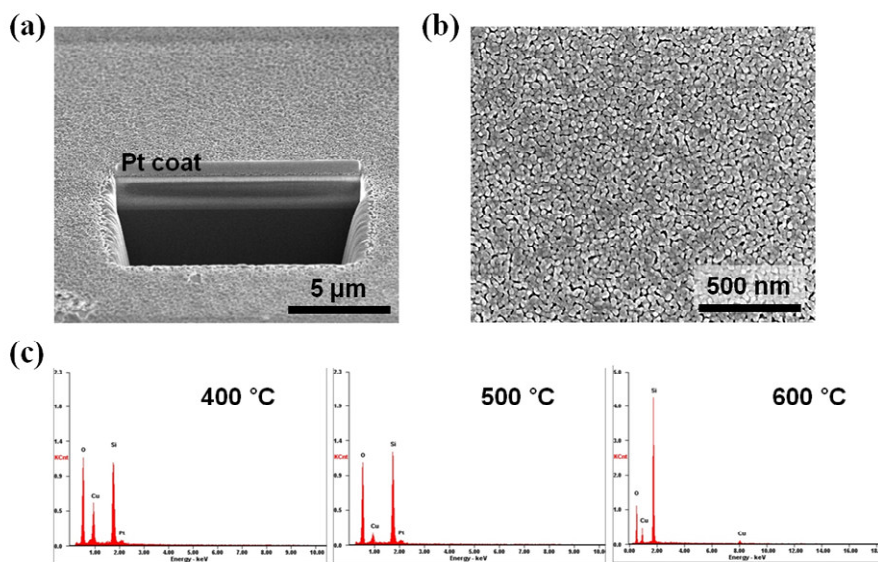


Figure 4.5. (a) Pt sputtered on the film after FIB fine milling to investigate the cross-section of the mesoporous CuO film calcined at 600 °C, (b) the surface morphology of the film calcined at 400 °C observed by FIB-SEM and (c) EDX patterns analyzed on the surfaces of the films calcined at 400, 500 and 600 °C, respectively.

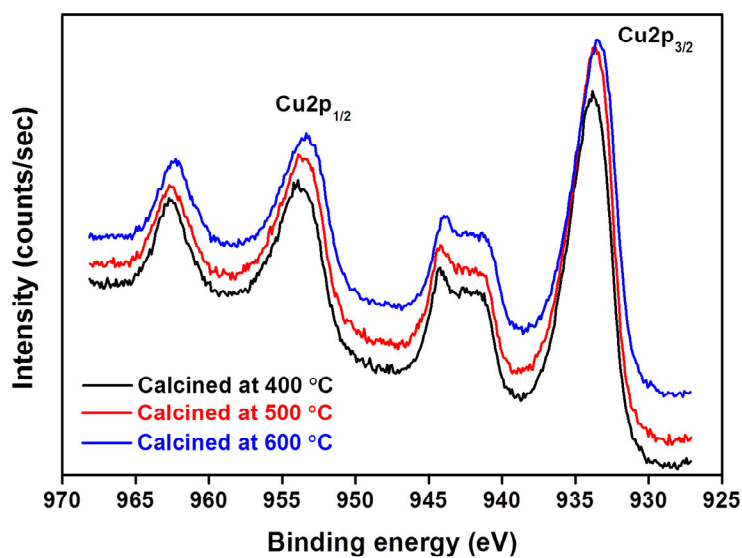


Figure 4.6. The Cu2p core level XPS spectra of the mesoporous CuO films calcined at 400, 500 and 600 °C.

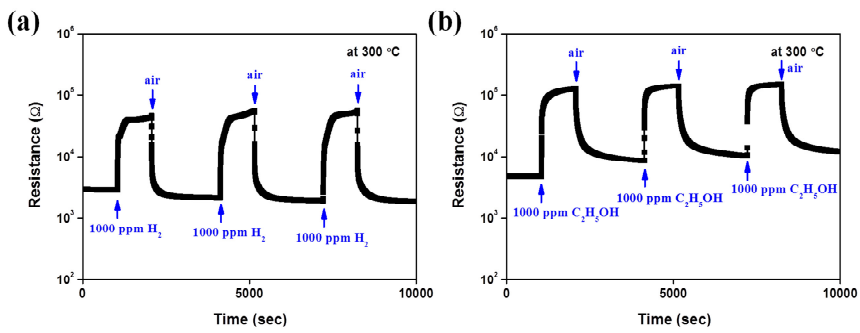


Figure 4.7. Reversible (a) H_2 and (b) $\text{C}_2\text{H}_5\text{OH}$ response transients of the mesoporous CuO films calcined at 500°C .

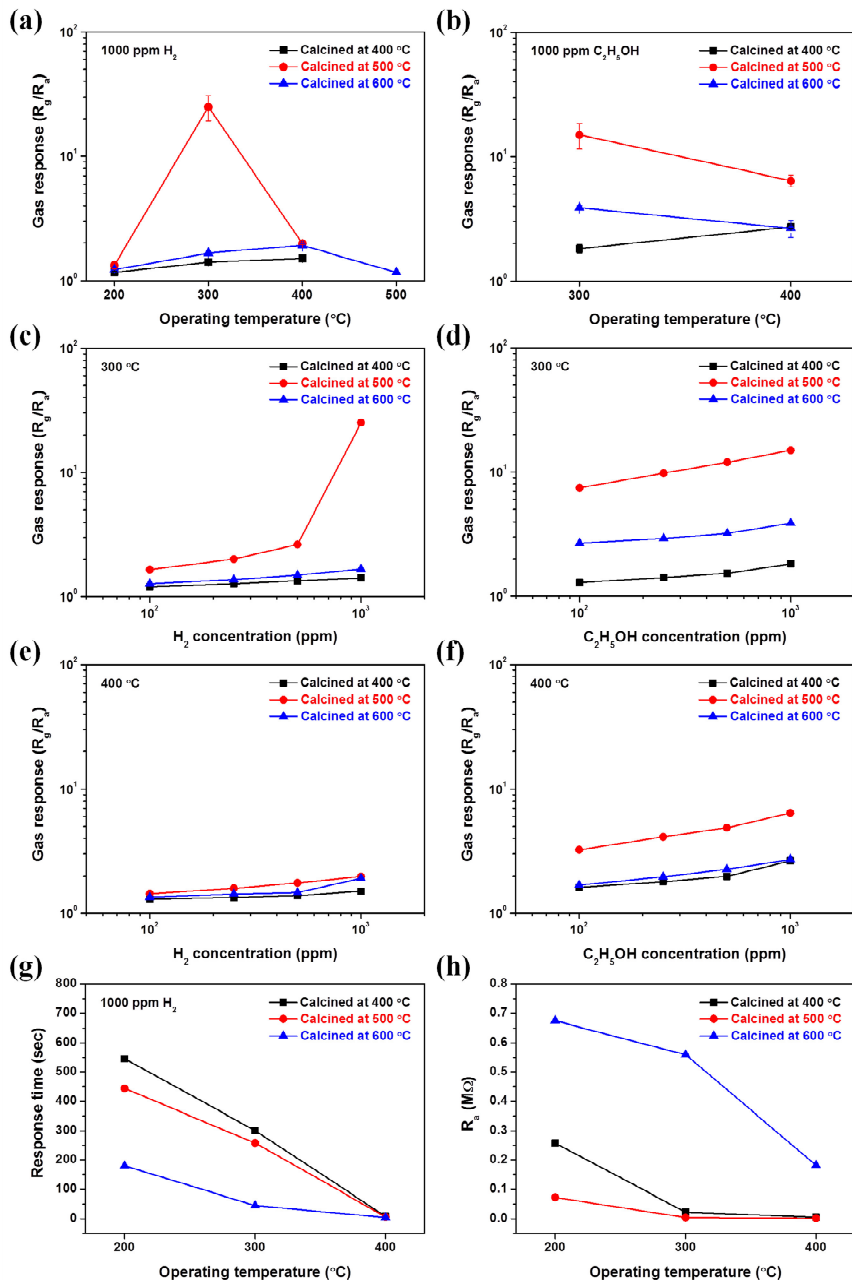


Figure 4.8. (a) H₂ and (b) C₂H₅OH responses of each CuO sensor shown as a function of operating temperature. The gas concentration dependences on (c) H₂ and (d) C₂H₅OH responses of each CuO sensor investigated at the operating temperature of 300 °C and those on (e) H₂ and (f) C₂H₅OH responses of each CuO sensor investigated at the operating temperature of 400 °C. (g) Response times to 1000 ppm H₂ and (h) the initial stand-by d. c. electrical resistances in air (R_a) of each CuO sensor shown as a function of operating temperature.

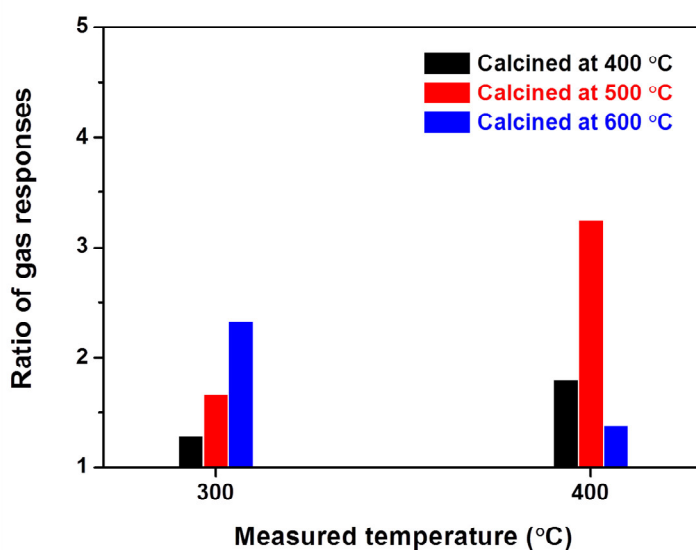


Figure 4.9. The ratio of gas responses of each CuO sensor shown in the operating temperatures of 300 and 400 °C, respectively.

Material form	H ₂ response (R _g /R _a)	Operating temperature	Publication year	Reference
Mesoporous CuO film	1.65 @ 100 ppm 2.01 @ 250 ppm 2.64 @ 500 ppm 25 @ 1000 ppm	300 °C	This year	This work
CuO nanowire field effect transistor (FET)	1.71 @ 500 ppm	200 °C	2009	[13]
Single crystalline CuO nanowire	1.24 @ 10000 ppm	250 °C	2009	[14]
CuO thin film	1.4 @ 10000 ppm	250 °C	2010	[15]
Porous CuO nanowire	9.75 @ 60000 ppm	250 °C	2010	[11]
Material form	C ₂ H ₅ OII response (R _g /R _a)	Operating temperature	Publication year	Reference
Mesoporous CuO film	7.45 @ 100 ppm 9.79 @ 250 ppm 11.96 @ 500 ppm 15 @ 1000 ppm	300 °C	This year	This work
CuO nanorod	2 @ 2000 ppm	300 °C	2007	[16]
Hollow and hierarchical CuO microsphere	~7.5 @ 2 ppm 2-3 @ 2 ppm ~38 @ 100 ppm	~230 °C 320 °C 320 °C	2007	[17]
Single crystalline CuO nanoribbon	~4 @ 1000 ppm	200 °C	2008	[18]
CuO nanowire field effect transistor (FET)	1.57 @ 500 ppm	200 °C	2009	[13]
Perpendicularly cross-bedded CuO microstructure	5.0-5.5 @ 500 ppm ~2 @ 100 ppm	200 °C	2009	[19]
CuO nanowire	1.5 @ 1000 ppm	240 °C	2009	[20]
CuO nanostructured film	~3 @ 10 ppm	200 °C	2009	[21]
CuO nanorod	9.8 @ 1000 ppm	210 °C	2011	[22]
CuO nanoplate	4.11 @ 100 ppm ~6 @ 500 ppm	200 °C	2012	[23]
Hierarchically porous CuO microsphere	1.9-2.0 @ 100 ppm	400 °C	2012	[24]
CuO nanoparticle	2.39 @ 100 ppm ~3.3 @ 1000 ppm	200 °C	2012	[25]

Table 4.1. Comparison of performances of the pristine CuO sensors reported in the literatures.

4.3 Direct printing synthesis of copper oxide hollow spheres

4.3.1. Experimental

4.3.1.1. Ink formulation and direct printing synthesis of CuO films with hollow spheres

Cu(II) complex ink was formulated with copper(II) formate hydrate ($\text{Cu}(\text{HCOO})_2 \cdot n\text{H}_2\text{O}$, 97% purity, Sigma-Aldrich), hexylamine ($\text{C}_6\text{H}_{15}\text{N}$, 99% purity, Sigma-Aldrich) and ethyl cellulose (48.0-49.5% (w/w) ethoxyl basis, 30-70 mPa·s, 5% in toluene/ethanol 80:20 (25 °C), Sigma-Aldrich) dissolved in 1-methyl-2-pyrrolidinone (NMP, 99% purity, Sigma-Aldrich). All chemicals were used without further purification. The Cu content (27.3 ± 0.8 wt%) and resulting tetrahydration ($n=4$) of a commercial precursor were determined by inductively coupled plasma atomic emission spectroscopy (ICP-AES, ICPS-8100, Shimadzu). To prepare the ink, copper(II) formate tetrahydrate powder was dissolved in hexylamine at a mole ratio of 1:1. Then, ethyl cellulose dissolved in NMP, equivalent to 8.5 wt% of Cu, was added. The ink was strongly mixed with zirconia balls in a paste mixer for some minutes. The Cu content in the final ink, analyzed by ICP-AES, was 18.4 wt%. All procedures were performed in ambient air at room temperature (RT). The formulated ink was printed on SiO_2 (2 μm)/ $\text{Si}<100>$ or $\text{SnO}_2:\text{F}$ (FTO) substrates by a doctor-blade method using a thickness-controllable spacer. Subsequently, the ink-printed films were heated thermally with calcination

with a rate of 5 °C/min to 200, 300, 400, 500 and 600 °C, respectively, held for 1 h at each temperature, and then cooled to RT naturally under static air atmosphere using a box furnace to ensure the formation of thick films. The substrates were cleaned using acetone, de-ionized water and ethanol prior to use.

4.3.1.2. Synthesis of CuO powders and film formation

For a comparison of sensor and photoelectrochemical (PEC) performance levels, conventional CuO powders were synthesized by a polymerized complex method (i.e., the Pechini process) [26]. First, 1 mol of citric acid (anhydrous, 99.5% purity, Junsei) was dissolved in 4 mol of ethylene glycol (anhydrous, 99.8% purity, Sigma-Aldrich) with constant stirring for 24 h at RT to obtain a transparent solution. Subsequently, 0.1 mol of copper(II) chloride dihydrate ($\text{CuCl}_2 \cdot 2\text{H}_2\text{O}$, 99.9% purity, High Purity Chemicals, Japan) was dissolved in the solution and stirred for 5 h at 90 °C in order to form a metal-citric acid complex through a chelate process. The transparent green solution obtained was further stirred for 16 h at 140 °C for polyesterification, and a yellowish sticky polymeric resin was finally obtained, showing high viscosity. This polymeric product was decomposed into black CuO powder via pyrolysis for 5 h at 400 °C, after which it was ground. Porous CuO films were prepared on clean SiO_2 (2 μm)/ $\text{Si}<100>$ or FTO substrates from a home-made paste including the synthesized CuO powder via a doctor-blade method. The coated films were annealed for 1 h at 500 °C under an ambient

atmosphere.

4.3.1.3. Characterization

The rheological properties of the ink were investigated by a rheometer (Advanced Rheometric Expansion System (ARES), Rheometric Scientific, UK) with steady-state sweeps at RT. The crystal structure and phase of the films and powders were analyzed by the X-ray diffraction θ - 2θ method (XRD, D8-Advance, BRUKER MILLER Co.) using Cu K α radiation ($\lambda = 1.5406 \text{ \AA}$). The surface and cross-sectional morphologies of the specimens were observed by a field emission scanning electron microscope (FE-SEM, JEOL JSM-6500F). The hollow structures were further examined by (high-resolution) transmission electron microscopy ((HR)TEM, JEM-3000F, JEOL, Japan) operated at 300 kV. Nitrogen adsorption and desorption isotherms were measured to yield Brunauer-Emmett-Teller (BET) specific surface area of the CuO hollow spheres and powders. The chemical composition was investigated by X-ray photoelectron spectroscopy (XPS, AXIS-His, KRATOS) with Mg K α radiation (1253.6 eV). The core-level XPS spectra for O1s and Cu2p were measured and energy calibration was achieved by setting the hydrocarbon C1s line to 284.5 eV.

4.3.1.4. Measurements of gas sensing and PEC properties

With regard to the gas-sensor measurements, a pair of comb-like Pt electrodes was deposited on the ink or powder films, formed on SiO₂ (2 µm)/Si<100> substrates, by sputtering through a mask. This was followed by firing for a short time at 500 °C without a change in the morphology or phase. Thereafter, Au wires were attached to the electrodes using Ag paste and the samples were dried at 80 °C in a conventional oven. The sensors were placed in a quartz tube located inside an electrical tube furnace with a gas inlet/outlet system. The sensor responses were obtained by measuring the changes in the electrical resistance between each reducing gas flow (with varying concentrations) balanced with air and a pure dry-air flow at 200-400 °C using a multimeter (Keithley 2002). PEC measurements were performed with a solar simulator (AM 1.5, 100 mW/cm², PEC-L11, Pecell) using a potentiostat (CHI 608C, CH instruments) in a three-electrode system. The ink or powder films formed on FTO substrates were used as a working electrode (photocathode). A counter electrode was a Pt wire and a reference electrode was a saturated Ag/AgCl. Aqueous electrolyte was 0.5 M Na₂SO₄ (pH~6) solution. The solution was purged by argon to remove the dissolved oxygen for 30 min before measuring. Area of a photocathode immersed in the electrolyte was 0.28 cm².

4.3.2. Results and discussion

4.3.2.1. Spontaneous formation mechanism of copper oxide hollow spheres in the form of film and their structural characteristics

The phase evolution of the ink-printed film was investigated with an increase in the heating (calcining) temperature by XRD, as shown in Figure 4.10(a). The ink film revealed a polycrystalline nature for all heating temperatures. The films calcined at 200 and 300 °C consisted of mixtures of Cu₂O and CuO phases, while only CuO was detected in the films calcined at 400 °C and over. For a quantitative comparison between the Cu₂O and CuO contents in the films calcined at 200 and 300 °C, the relative peak intensities, I(CuO)/I(Cu₂O), were determined using the XRD peaks of each phase, for which the intensity (integrated area) ratio between the CuO (002)/(11̄1) and Cu₂O (111) main peaks and that between the CuO (111)/(200) and Cu₂O (200) second peaks were averaged. In the film calcined at 200 °C, the resulting I(CuO)/I(Cu₂O) ratio was 0.29, indicating that the content of Cu₂O overwhelmingly prevailed over that of CuO. In contrast, CuO exceeded Cu₂O with an I(CuO)/I(Cu₂O) ratio of 4.36 in the film calcined at 300 °C. The CuO peaks were gradually sharpened and strengthened with an increase in the calcination temperature from 200 to 600 °C, indicating improved crystallinity of the films. The evolution of the crystallite sizes with the calcination temperature was determined by the Scherrer formula using the full width at half maximum (FWHM) for the main and second peaks of CuO and Cu₂O, as

shown in Figure 4.10(b). Interestingly, the crystallite sizes of Cu₂O, obtained from all of its peaks, were constantly maintained as the calcination temperature increased from 200 to 300 °C, reflecting that Cu₂O is oxidized to CuO and does not increase in size when it is heated in air. On the other hand, the crystallite sizes of CuO gradually increased with an increase in the calcination temperature, indicating the coarsening of the CuO grains.

The cross-sections and surfaces of the ink-printed films, calcined at 200–600 °C, were observed by FE-SEM in order to investigate their microstructural evolution (Figure 4.11). All of the films had a thickness of 8 ± 1 µm and exhibited a randomly assembled structure of the spherical particles inside them, as shown in Figures 4.11(a), (d), (g), (j) and (m). In the earlier studies, these features generally occurred when printed ink film was thermally calcined at temperatures above 170 °C, specifically when the amount of hexylamine was roughly two times lower than that of the copper formate in the ink. However, only spherical particles were assembled with non-hollow, solid cores at such low temperatures. At elevated temperatures, the spontaneous hollowing of solid-core spheres is observed for the first time in this work. The solid-core spheres formed at low temperatures are transformed into hollow spheres with the stepwise phase transition of Cu(II) complex → Cu → Cu₂O → CuO while they are heated in air. This differs with mesoporous/porous ink films prepared using Cu(II) complex inks formulated with low Cu contents and viscosities. Consequently, a greater amount of metal in the ink appears to be advantageous for producing such solid-core spheres as precursors for hollow spheres. It was experimentally found that the spheres

emerge inside films printed using the highly viscous inks formulated with Cu contents of ~14 wt% or more.

In all of the calcined ink-printed films, smaller particles were located at the near surface region, in contrast to the large spherical particles. The large spheres maintained a submicron size ($\leq 1 \mu\text{m}$ in diameter) at all calcination temperatures, whereas the smaller particles varied somewhat in terms of their shape and size. Additional images of the large spheres and the small particles near the film surfaces are shown in Figures 4.11(b), (e), (h), (k) and (n) and in Figures 4.11(c), (f), (i), (l) and (o), respectively. In the film calcined at 200 °C, the large and small particles showed three-dimensional spherical and cubic shapes, respectively (Figures 4.11(b) and (c)). Particularly, the small particles assembled near the film surface revealed mostly cubic shapes with sides of 200-300 nm. These were regarded as Cu₂O crystals because their morphologies corresponded well with those of Cu₂O particles exhibiting cubic symmetry of the {100} facets, as synthesized via various solution routes at moderate temperatures in previous reports [27-31]. In light of the earlier XRD results, it was deduced that the large spheres consisted mainly of Cu₂O with a low CuO content. Indeed, the angular surfaces of the large spheres served as evidence that Cu₂O cubes constituted the particles. Dark spots were also observed on the surfaces of both types of particles. These were regarded to be the residue of the formate-amine couples, i.e., bound hexylamine and N-1-hexylformamides, which were not volatilized at this low temperature, as they disappeared during the calcination process at 300 °C or more (see Figures 4.11(d) and (e)). As shown in Figure 4.11(c), the film surface was covered

with cubic Cu₂O small particles with smooth surfaces. In the film calcined at 300 °C, they were transformed from the cubic to the spherical shape without a change in their size, through oxidation from Cu₂O into CuO, as supported by the XRD results (Figure 4.11(f)). Both types of particles maintained the dense surfaces composed of smaller grains (Figures 4.11(e) and (f)). In particular, coarse structures consisting of sparsely populated grains ~50 nm in diameter (similar to size of the grains constituting the shells) were observed in the inner parts stripped from the dense shells of the large spheres, as shown in Figure 4.11(e). Membranes of the polymeric ethyl cellulose added to the ink were found at intervals of the particles in the films calcined at 200 and 300 °C (see Figures 4.11(c) and (f)), but not in the films calcined at 400 °C or higher. This is related to their decomposition characteristics. When calcined at 400 °C, the large spheres clearly showed hollow cores in their interiors (Figure 4.11(h)). The shell surfaces of the spheres were still dense, but the grains constituting them were slightly enlarged to ~70 nm in diameter. However, the coarse structures observed inside the shells of the spheres calcined at 300 °C disappeared. Significantly, it was observed that the size of the small particles near the film surface decreased to ~70 nm in diameter, which was similar to that of the grains constituting the shells of the large spheres at this calcination temperature (Figure 4.11(i)). This reflects the fact that the small particles acted as primary particles constituting the large hollow spheres (secondary particles). At 500 °C, distinct hollow cores in the large spheres were also observed (Figure 4.11(k)). The surfaces of the hollow spheres became rough and porous, and the diameters of the grains constituting their shells increased

to ~100 nm. The shells were composed of stacks of two grains with open pores. The sizes of the small particles near the film surface recovered close to those calcined at 200 or 300 °C due to the coalescence of the smaller particles during additional heating from 400 to 500 °C, reducing their overall density (Figure 4.11(l)). During calcination at 600 °C, the hollow spheres which formed endured well and their shells became remarkably dense again due to the sintering effect, which caused necking and densification of the grains (Figure 4.11(n)). This is also shown on the film surface in Figure 4.11(o). The necks connecting the small particles were clearly observed. The size of the connected small particles was similar to that of the grains constituting the shells of the large hollow spheres. Interestingly, the size of the small particles strongly depended on the calcination temperature, whereas that of the large spheres was independent of this factor. Instead, the size of the grains constituting the large spheres was affected by the calcination temperature.

However, it was not clarified by FE-SEM observation whether the large spheres calcined at 200 or 300 °C had hollow cores in their interiors. Thus, an additional TEM analysis was performed to investigate their cores clearly. Prior to this analysis, large spheres collected from ink-printed films calcined at each temperature were mixed with polymeric resin and then hardened. Thereafter, the samples were sliced at intervals of about 200 nm by a microtome, after which the cores of the spheres were observed by TEM, as shown in Figure 4.12. As a result, small voids near the core were observed in the interiors of the large spheres calcined at 200 °C instead of complete hollow cores, whereas interior voids were not detected in the cubic Cu₂O

small particles. The two-dimensional hexagon images of the small particles in the figure were created from top views of their cubes when rotated three-dimensionally (inset). On the other hand, the large spheres calcined at 300 °C revealed distinct hollow cores with diameters of 300-400 nm in their interiors and donut-like shapes given that they were sliced by a microtome. In particular, it was found that the shells of these hollow spheres consisted of dense outer shells and coarse inner shells, which corresponded well to the structures observed by FE-SEM, as shown in Figure 4.11(e). The large spheres calcined at 400, 500 and 600 °C exhibited clear hollow cores in their interiors and enlarged grains in their shells, which also corresponded well to the FE-SEM results (Figures 4.11(h), (k) and (n)).

On the basis of the XRD, FE-SEM and TEM observations, a spontaneous formation mechanism of hollow spheres inside the ink-printed film was found to occur during the heating steps, as shown with the schematic illustration in Figure 4.13. As mentioned earlier, the as-printed film using the Cu(II) complex ink is calcined into metallic Cu and subsequently oxidized to Cu₂O and CuO during slow heating up to 200 °C. The primarily formed Cu₂O is spontaneously assembled inside the film in two types, i.e., smaller cubic particles with a single phase at the near film surface region and larger spherical particles mixed with the minority CuO which function as precursors for the formation of hollow spheres at elevated temperatures. The solid cores of the large spheres are surrounded by small Kirkendall voids, generated via the bulk diffusion of atoms/ions at the Cu-O interface during the oxidation of Cu → Cu₂O/CuO at this low temperature of 200 °C [32]. Upon additional

heating to 300 °C, completely hollow cores are formed inside the large spheres while the Cu₂O phase is oxidized to CuO phase. This hollowing process involving a compositional transition (Cu₂O → CuO) is attributed to the Kirkendall effect, demonstrating unbalanced void formation due to the different diffusion rates in an inter-diffusive couple [33-37]. In detail, evacuation of the solid core by the Kirkendall effect occurs when the outward diffusion of the Cu cation through the oxide shell layer is much faster than the inward diffusion of the oxygen to the core ($D_{Cu} > D_O$ for the diffusion coefficient and thus $J_{Cu} > J_O$ for the total flux) in the Cu-O diffusion couple [37,38]. This essentially involves variations in the phase, composition or stoichiometry during the oxidation of Cu. Furthermore, the shells of the hollow spheres consist of dense outer shells and coarse inner shells. The dense, less permeable structures shown in their outer shells further confirm that their hollowing occurs due to the Kirkendall effect [39]. The small Kirkendall voids left inside the coarse inner shells are evidence that the hollowing proceeded via the surface diffusion of the core material (i.e., the fast-diffusing Cu cations) along the pore surface to the shell parts while heating at 300 °C [32,40]. Meanwhile, the cubic small particles located near the film surface become spherically shaped without a change in their size or hollowing during the oxidation of Cu₂O to CuO. Upon heating at 400 °C, the hollow spheres consist only of dense, less permeable shells. The sizes of the small particles near the film surface decrease because they are consumed by the grain growth in the shells of the large hollow spheres. Under additional heating to 500 °C, the shells of the hollow spheres become rough and porous due to the grain

growth. The sizes of the small particles near the film surface recover to a range similar to those calcined at 200 or 300 °C, while the particle density is decreased due to the coalescence of the smaller particles. The complete hollow structures of the large spheres developed by the Kirkendall effect are well maintained upon additional heating to 600 °C. However, the shells of the hollow spheres become dense and the small particles near the film surface are all connected to one another by means of necking. This results from the high-temperature sintering. Consequently, the spontaneous hollowing of the oxide particles originates from the Kirkendall effect and their shells undergo grain growth and sintering during thermal heating via the direct printing synthesis process.

4.3.2.2. Gas sensing and PEC properties of ink-printed CuO film with hollow spheres

The ink-printed CuO film with hollow spheres, calcined at 500 °C, was chosen to assess its feasibility for high-throughput applications in superior gas sensor and PEC devices due to its high surface-to-volume ratio and gas/electrolyte permeability imparted by its completely hollow cores and rough/porous shell structures and by its single phase, high crystallinity, no organic/polymer residue and operability at the optimal temperature (400 °C) for sensors [39]. In addition, this film showed a reduction in the density of its small particles near its surface region, as mentioned above, fortunately simplifying the permeation of the target gases or electrolytes. Well-defined,

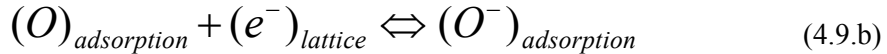
spontaneously assembled CuO hollow spheres with a uniform submicron-diameter ($\leq 1 \mu\text{m}$) and permeable shells were noted in the cross-section of the film by FE-SEM imaging (Figure 4.14(a)). Nitrogen adsorption and desorption isotherms and the corresponding pore size distribution (inset) of the CuO hollow spheres are shown in Figure 4.14(b). The BET specific surface area of the material was $24.5 \text{ m}^2/\text{g}$ and the total pore volume was $0.1 \text{ cm}^3/\text{g}$. The pore size distribution indicated that the CuO hollow spheres have the multi-scale pores with the diameter of 3.8 nm, 24.4 nm and 50.4 nm. The lattice fringes of the shell of a single hollow sphere observed by HRTEM clearly demonstrated the polycrystalline shells of the hollow spheres, as shown in Figure 4.14(c). The fast Fourier transformation (FFT) pattern of the selected single-crystalline area (the inner part of the red square in Figure 4.14(c)), viewed along the $[1\bar{1}0]$ zone axis, showed four strong peaks that were indexed to the $\{111\}$ planes of the monoclinic CuO (see the inset in Figure 4.14(c)). A high-magnification HRTEM image of the same area also represent the real lattices equivalent to monoclinic CuO (111) and $(11\bar{1})$ in Figure 4.14(d). The selected-area electron diffraction (SAED) pattern shown in Figure 4.14(e) again confirms that the hollow spheres are composed of polycrystalline monoclinic CuO. The chemical composition of the hollow spheres was investigated by XPS; the Cu2p core level spectrum is shown in Figure 4.14(f). The Cu2p_{3/2} and Cu2p_{1/2} peaks were located at 933.6 and 953.5 eV, respectively, in good agreement with the binding energies for the Cu(II) lattice of CuO [3-5]. Furthermore, all of the shake-up satellite peaks of the Cu2p_{3/2} and Cu2p_{1/2}, observed at 942.8 and 962.5 eV, respectively, and the

doublet structure shown in the Cu2p_{3/2} satellite peak clearly indicate that the hollow spheres consist of cupric oxide consisting of Cu(II) with an open 3d⁹ shell [3,6,7]. As a result, it was confirmed that the ink-printed film, calcined at 500 °C, consisted of well-defined monoclinic CuO hollow submicron spheres with 200-nm-thick polycrystalline shells.

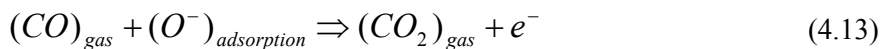
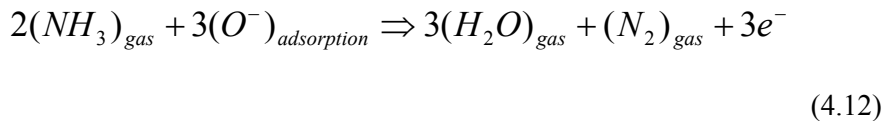
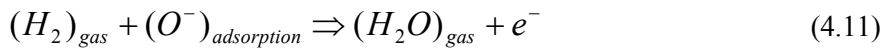
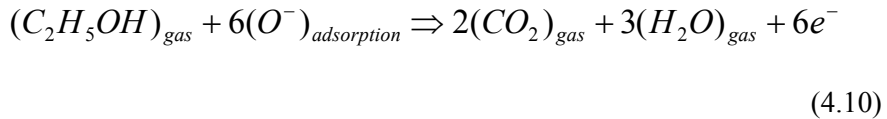
The sensing properties of the CuO film with hollow spheres were investigated with various reducing gases (C₂H₅OH, H₂, NH₃, CO and H₂S) balanced with air at operating temperatures of 200, 300 and 400 °C. As shown in Figure 4.15(a), the gas responses ($R_{\text{gas}}/R_{\text{air}}$, the ratio of the resistance in air (R_{air}) to that in a target gas (R_{gas})) were obtained with stable and reversible response transients at the cross-input conditions of the air and the reducing gases, guaranteeing the stability and reproducibility of the printed CuO hollow-sphere sensor. Typical p-type semiconducting responses in which the electrical resistance increases under a reducing gas were exhibited. The responses to all target gases decreased monotonously with a decrease in the gas concentration. The gas responses to C₂H₅OH, H₂, NH₃ and CO were enhanced by about twofold with an increase in the operating temperature from 200 to 300 °C, while they were maintained without a noticeable change upon further heating from 300 to 400 °C at all gas concentrations (50-1000 ppm). A maximum gas response of ~3 was obtained with 1000 ppm of C₂H₅OH at the operating temperatures of 300 and 400 °C. The gas responses to H₂ were second highest, and those for NH₃ were third, followed by the responses for CO at all operating temperatures and gas concentrations, with the exceptions being the responses for H₂S (The gas responses for H₂S will be described later

due to their relatively low detection concentrations and unusual response behavior). The response and recovery times were defined as the time required for the response and that for the recovery to reach 90% of the final signal, respectively. These times gradually decreased, eventually reaching a response time of ~2 min and a recovery time of ~6 min (i.e., the sensing speed was faster) with an increase in the operating temperature from 200 to 400 °C regardless of the gas concentration or type, except for those for H₂S. The temperature dependence of the gas response and the response/recovery times can be explained in terms of the kinetics and mechanics of the gas adsorption and desorption characteristics on the surface of the CuO hollow spheres [41]. At a low temperature of 200 °C, the sensor response and sensing speed are restricted by the speed of the chemical reaction (i.e., the reaction-controlled), as demonstrated by the insufficient thermal activation of the gas molecules reacting with the adsorbed oxygen species, leading to both a low response and a low speed. At high temperatures above 300 °C, these are governed by the speed of the diffusion of the gas molecules (i.e., the diffusion-controlled), which is demonstrated by sufficient thermal energy to overcome the potential barrier to hole transport formed on the surface of the CuO grains, resulting in a significant increase in the hole concentration and leading to a high response rate and speed. Such a difference in the response rate with a different gas type is due to the difference in the chemical dissociation of the gases on the CuO surface, thus endowing the sensor with gas selectivity. The detailed response mechanism for each gas is as follows. First, atmospheric O₂ gases are adsorbed in the form of O⁻ ions on the CuO surface at temperatures above

200 °C (Reaction equation 4.9a and b) [42].



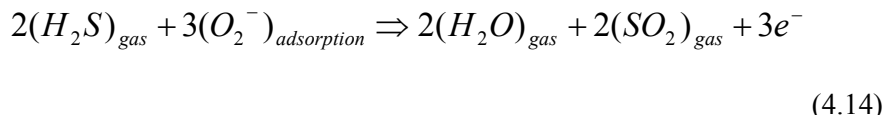
This process increases the hole density of the surface charge layer of the CuO and thus reduces the resistance of the CuO. When the CuO sensor is exposed to each reducing gas, the chemical reactions are as follows:



The adsorption of the reducing gases on the surface of the p-type CuO

sensor decreases the hole density in the surface charge layer and therefore increases the sensor resistance. As a result, a change in the resistance depending on the gas adsorption/desorption induces a gas response or sensitivity in the sensor. At that moment, the difference in the chemical kinetics, including the molecular dissociation, gas adsorption-desorption and electron-hole annihilation due to the different types of gas molecules on the sensor surface, will cause a difference in the sensor response.

Given that CuO exhibits essentially good sensitivity toward H₂S gas [43-45], the H₂S sensing properties of our CuO hollow spheres were further examined with low gas concentrations of 1-20 ppm. Interestingly, the sensing responses did not recover at a low operating temperature of 200 °C, but they recovered at 300 °C or more, as shown in Figure 4.15(a) (bottom). This non-recovery at a low temperature can be understood in terms of the H₂S sensing mechanism of CuO. Two different reaction mechanisms between CuO and H₂S are established [43-45]. At low H₂S concentrations (<0.5 ppm), the adsorbed oxygen on the CuO surface causes the oxidation of H₂S, as follows:

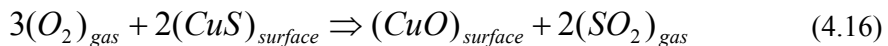


The released electrons recombine with holes on the CuO surface, which results in an increase in the resistance. This process is easily recovered by removing H₂S and exposing the CuO surface to air. At high H₂S

concentrations (0.5-50 ppm), another reaction (4.15) occurs together with reaction (4.14).



Reaction (4.15) involves the formation of the metallic CuS compound, which decreases the resistance. This process is somewhat reversible, but this is much slower than it is for reaction (4.14), and the reversibility is thermally activated. When air is supplied, CuS is oxidized and converted back to CuO through the following reaction:



In our case, because the H₂S concentration tested was in the high range of 1-20 ppm, reaction (4.15) governed the overall sensor response more than reaction (4.14). Under the domination of reactions (4.15) and (4.16) with a slow recovery time and thermal promotion, no baseline was recovered in a reasonable time (minutes) at the low temperature of 200 °C. At 300 °C, recovery was slow, and reasonably fast recovery times were finally attained with the highest responses at 400 °C. However, at the high temperature of 400 °C, such a rapid recovery is considered to originate from the domination of the oxidation of H₂S by reaction (4.14) because the temperature was too high for the formation of metallic CuS by reaction (4.15) [43].

In particular, at 400 °C, the response time decreased remarkably with an increase in the H₂S concentration, whereas the recovery time remained relatively unchanged, at ~12.6 min, as shown in Figure 4.15(b). Finally, the fastest response speed of ~2 min was achieved at 10 ppm and was maintained to 20 ppm. Noticeably, the concentration-dependent response time toward H₂S gas is distinguished from the concentration-independent response times of other reducing gases.

H₂S is a highly toxic gas which affects the human nervous system at a very low concentration; thus, its permissible exposure limit value is set to 10 ppm for every 10 min of exposure by the US National Institute for Occupational Safety and Health (NIOSH) [45,46]. In our CuO hollow-sphere sensor operated at 400 °C, the lowest concentration to quantify H₂S could be as low as 1 ppm, which is an order of magnitude lower than the permissible exposure limit concentration (10 ppm). Furthermore, our sensor exhibited the fastest response speed of ~2 min, which is five times shorter than the permissible exposure limit time (10 min) at H₂S concentrations above the permissible exposure limit concentration (10 ppm).

The sensor responses to various reducing gases for the CuO hollow spheres (specific surface area = 24.5 m²/g) prepared by direct printing synthesis were compared with those of CuO powders (1.5 m²/g) in Figure 4.15(c). Both types of CuO sensors were compared with the same submicron diameter ($\leq 1 \mu\text{m}$) sizes, film thickness (~8 μm), polycrystalline characteristics and synthesis temperature (500 °C). The responses measured at 300 or 400 °C to 1000 ppm of C₂H₅OH, H₂, NH₃ and CO gases and those measured at

400 °C to 10 or 20 ppm of H₂S gas were chosen for a comparison of the two types of CuO sensors. As a result, the response (~3) of the CuO hollow spheres was two times higher than that (~1.5) of the CuO powder for C₂H₅OH. In addition, the CuO hollow spheres exhibited a high and stable response of ~2 to H₂S, whereas no response was detected in the CuO powder with unstable baselines throughout the H₂S concentration range, presumably due to its relatively low specific surface area. For H₂, NH₃ and CO, the sensor responses of the CuO hollow spheres were also higher than those of the CuO powders. These enhanced gas responses of the CuO hollow spheres are also comparable to the values reported for various nanostructured CuO sensors prepared by other relatively complicated and time-consuming processes [13,14,16,20,24,25,43].

Current density vs. applied potential (J-V) plots for CuO hollow-sphere and powder photocathodes at the dark and under illumination are presented in Figure 4.16. The potentials were scanned cathodically at 50 mV/s. The photocurrent densities were measured in order to estimate water splitting performance of the photocathodes in the present study, as in general they are proportional to the amount of hydrogen evolution for cathode and oxygen evolution for anode in PEC cell, respectively. As a result, the CuO hollow-sphere photocathode exhibited nearly three times higher photocurrent density (1.47 mA/cm²) than that (0.54 mA/cm²) of the powder photocathode at the bias voltage of -0.3 V vs. Ag/AgCl. The photocurrent densities (vs. dark currents) were 2.39 mA/cm² for hollow sphere and 0.66 mA/cm² for powder at -0.55 V vs. Ag/AgCl, equivalent to water reduction potential (0 V for

reversible hydrogen electrode), respectively. Although the CuO hollow-sphere photocathode produces high dark current at negatively high bias voltages over -0.3 V vs. Ag/AgCl, its photocurrent density (vs. dark current) is considerably higher than the values (0.35-1.20 mA/cm² at water reduction potential) previously reported [47-50]. Such a high photocurrent density measured with the CuO hollow-sphere photocathode is considered to originate from its multi-scale porous structure and thus high specific surface area.

Consequently, in the present study, the high-throughput printing fabrication of a nanostructured p-type gas sensor and photocathode exhibiting superior performances could be successfully realized using CuO hollow spheres synthesized facilely by direct-printing with Cu(II) complex ink on a substrate. This technique (i.e., the direct printing synthesis of oxide hollow spheres) and its principles (i.e., the spontaneous hollowing by the Kirkendall effect) are expected to be applicable to the high-throughput printing fabrication of high-performance nanostructured batteries, solar cells, photonic devices and biological system. The technique can also be utilized in systems with different materials (e.g., Zn-O or Al-O [38,39]) in which the diffusion of the metal cation is faster than the diffusion of the anion. In this work, thermal heating was used as the energy source to promote hollowing, resulting in the requiring high-temperature processing exceeding 300 °C. If, however, other advanced methods such as the selective laser or flash sintering methods are used and controlled properly, the effective printing fabrication of hollow spheres and devices may be possible at lower temperatures applicable to polymer substrates and flexible devices.

4.3.3. Conclusions

In this report, we introduced the direct printing synthesis of copper oxide hollow spheres in the form of film on a substrate by printing using a Cu(II) complex ink, for the first time, resulting in their facile, scalable, high-throughput production and straightforward device fabrication. The Cu(II) complex ink based on formate-amine coupling was formulated optimally with a high viscosity of 23.58 Pa·s (or 23580 cP) at a shear rate of 1 s⁻¹. The ink was printed on a substrate by a doctor-blade method and subsequently thermal-calcined, with sequential thermal decomposition and oxidation steps. Polycrystalline copper oxide hollow spheres with submicron diameters ($\leq 1 \mu\text{m}$) were formed spontaneously while being assembled in the form of film with good adhesion to a substrate during thermal heating. This spontaneous hollowing mechanism was found in a stepwise experiment to result from the Kirkendall effect during oxidation ($\text{Cu} \rightarrow \text{Cu}_2\text{O} \rightarrow \text{CuO}$) at an elevated temperature. The ink-printed CuO film with hollow spheres, calcined at 500 °C, was chosen for use in superior p-type gas sensor and photocathode for PEC water splitting due to its completely hollow core (a high surface-to-volume ratio), rough/porous shell structure (high gas/electrolyte permeability), single phase, high crystallinity, and no organic/polymer residue. It was then compared to conventional CuO powder sensor and photocathode. As a consequence, the CuO hollow-sphere films prepared by a facile method via direct printing synthesis exhibited high gas responses and permissible response speeds to reducing gases (C₂H₅OH, H₂, NH₃, CO and H₂S) and high

photocurrent density, compared with conventional CuO powder films and with the values previously reported, thus exemplifying the successful realization of the high-throughput printing fabrication of superior nanostructured devices.

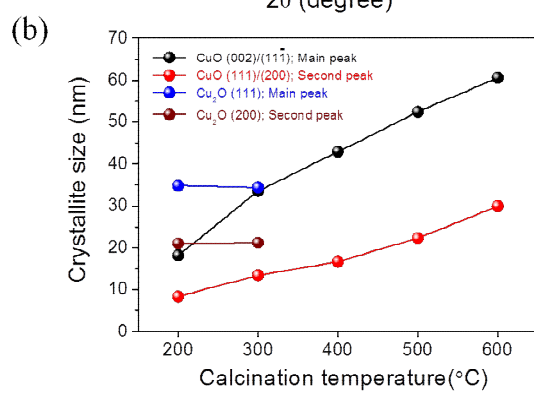
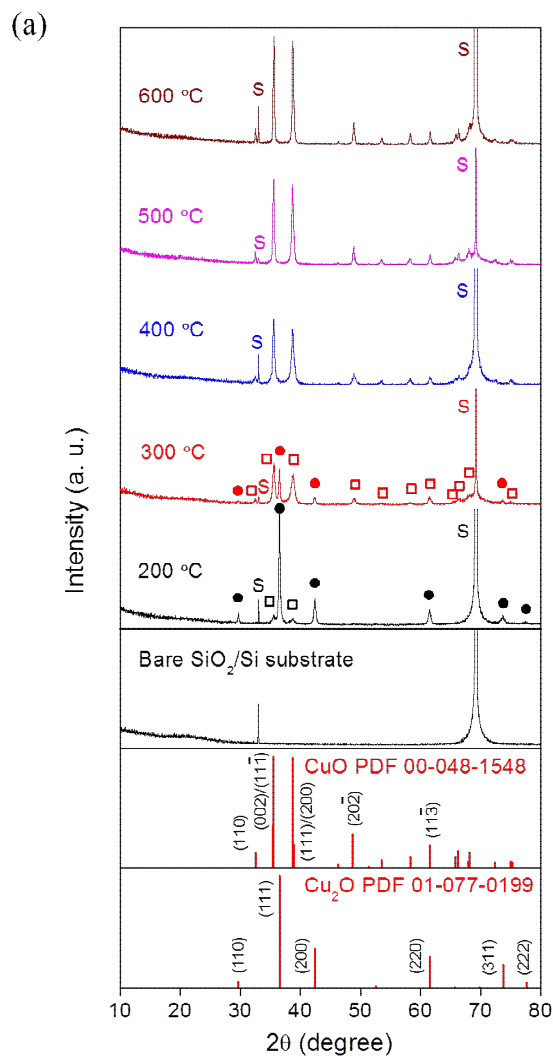


Figure 4.10. (a) XRD patterns of films calcined at each temperature after being printed on SiO_2/Si substrates with Cu(II) complex ink (S, \square and \bullet denote the peaks originating from the substrate, CuO and Cu_2O , respectively). (b) The evolution of the crystallite sizes of the CuO and Cu_2O phases in the films shown as a function of the calcination temperature as determined by the Scherrer formula.

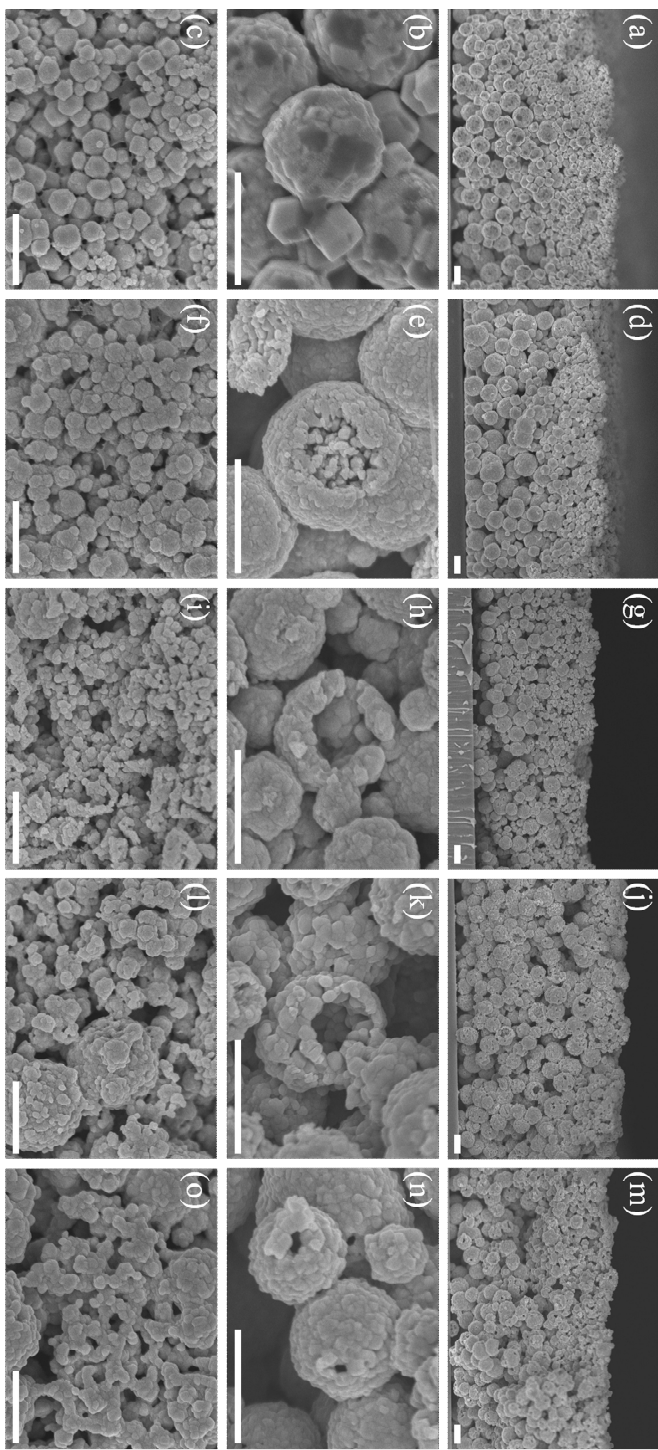


Figure 4.11. FE-SEM cross-sectional views of ink films calcined at (a) 200, (d) 300, (g) 400, (j) 500 and (m) 600 °C. The images focus on large spheres inside the ink films calcined at (b) 200, (e) 300, (h) 400, (k) 500 and (n) 600 °C, respectively. Top views of the surface morphologies of the ink films calcined at (c) 200, (f) 300, (i) 400, (l) 500 and (o) 600 °C, respectively. All scale bars are 1 μ m.

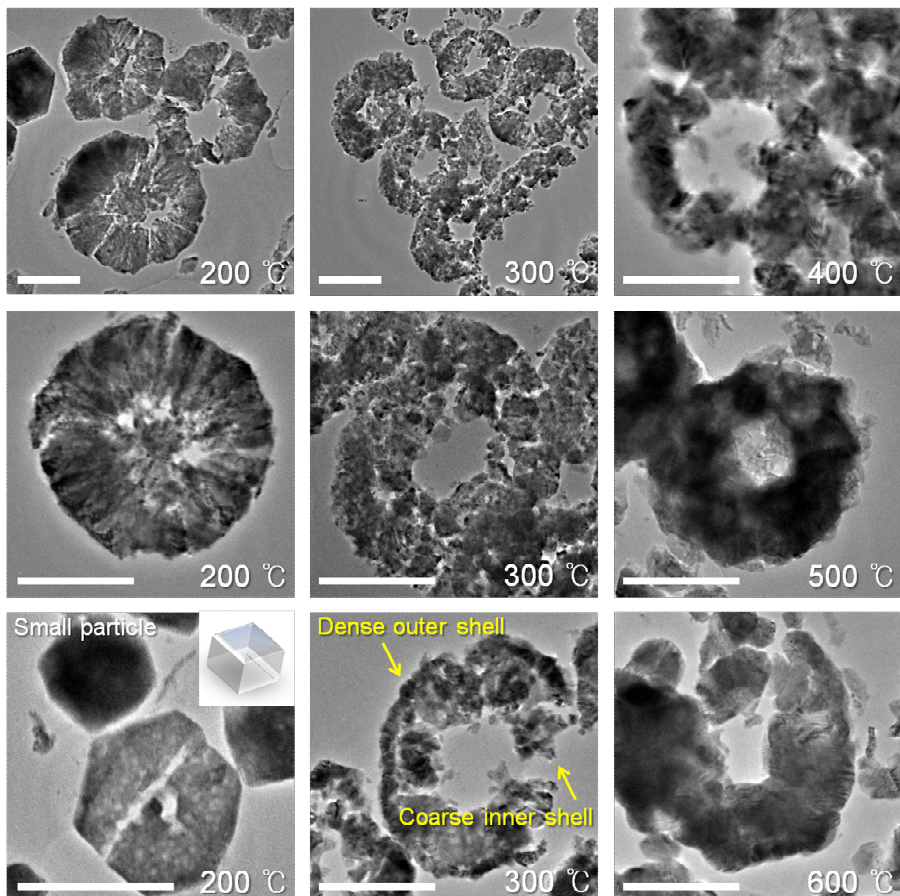


Figure 4.12. TEM images of the particles inside ink-printed films calcined at 200, 300, 400, 500 and 600 °C and sliced by a microtome. All scale bars are 0.5 μ m.

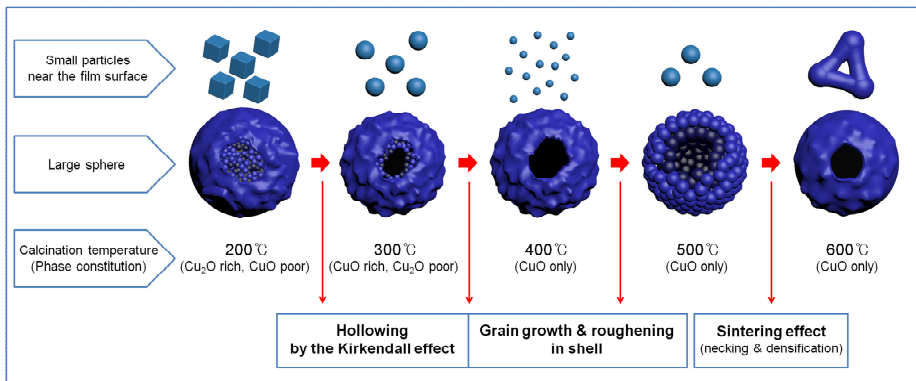


Figure 4.13. Schematic illustration depicting the spontaneous formation mechanism of copper oxide hollow spheres inside a film sample printed with Cu(II) complex ink during thermal heating.

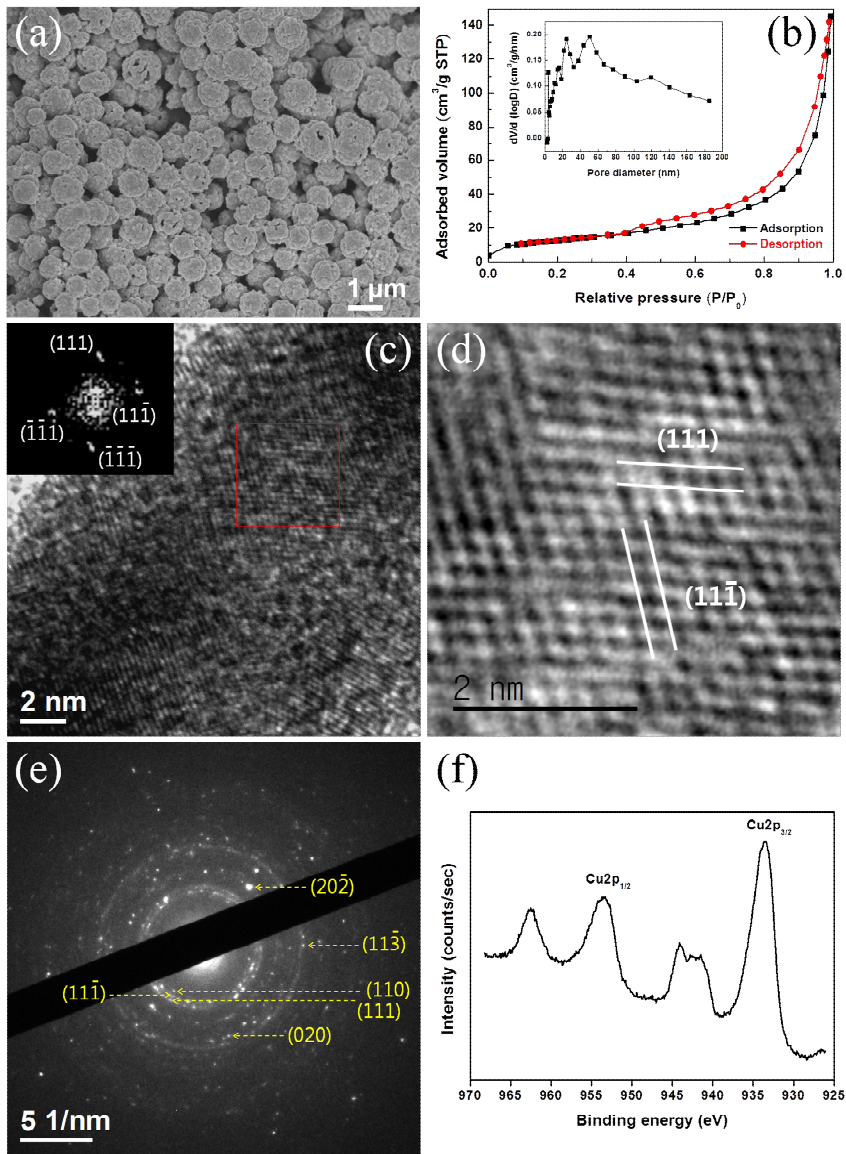


Figure 4.14. (a) CuO hollow spheres assembled spontaneously inside an ink-printed film sample calcined at 500 °C as observed by FE-SEM and (b) their nitrogen adsorption/desorption isotherm and Barrett-Joyner-Halenda (BJH) pore size distribution plot (inset). (c) The lattice fringes of the shell of a single CuO hollow sphere, observed by HRTEM. The inset shows the FFT pattern of the selected single-crystalline area (the inner part of the red square). (d) High-magnification HRTEM real-lattice image of the same single-crystalline area. (e) SAED pattern of the shell. (f) The Cu2p core-level XPS spectrum of the ink-printed CuO film with hollow spheres calcined at 500 °C.

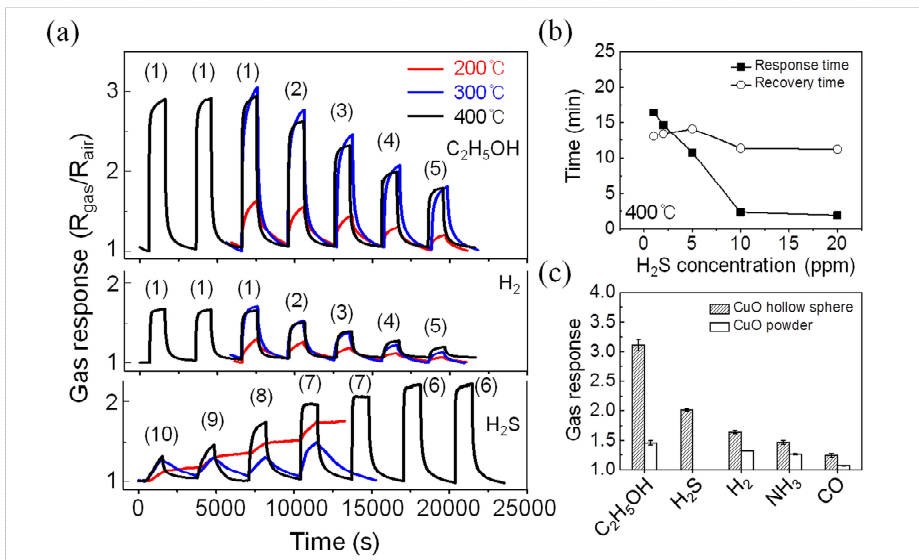


Figure 4.15. (a) Gas responses to $\text{C}_2\text{H}_5\text{OH}$, H_2 and H_2S by a CuO hollow-sphere sensor measured at operating temperatures of 200, 300 and 400 °C with various gas concentrations ((1) 1000, (2) 500, (3) 250, (4) 100, (5) 50, (6) 20, (7) 10, (8) 5, (9) 2 and (10) 1 ppm). (b) Response/recovery times for H_2S gas shown as a function of the gas concentration at an operating temperature of 400 °C. (c) Gas responses to reducing gases of a CuO hollow-sphere sensor compared to those of a CuO powder sensor. The responses measured at 300 or 400 °C to 1000 ppm of $\text{C}_2\text{H}_5\text{OH}$, H_2 , NH_3 and CO gases and those measured at 400 °C to 10 or 20 ppm of H_2S gas were compared.

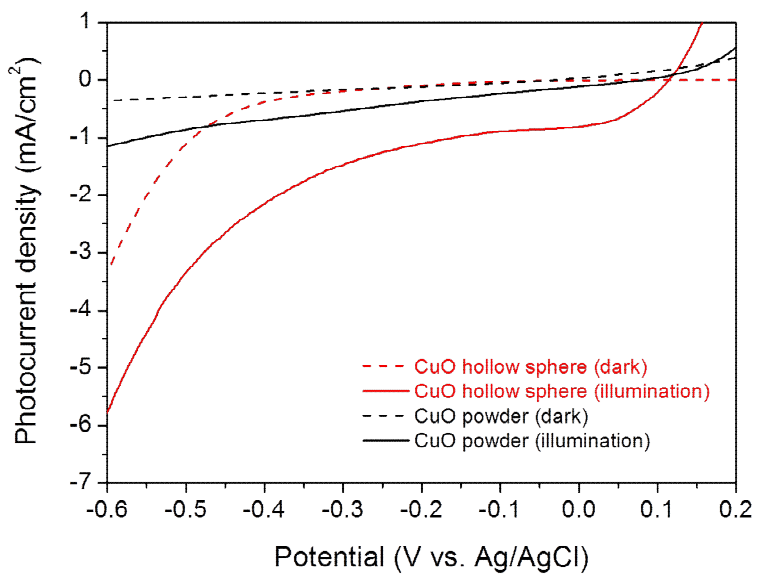


Figure 4.16. Current density vs. applied potential (J-V) plots for CuO hollow-sphere and powder photocathodes.

4.4 Closing remarks

CuO hollow-sphere film exhibited inferior gas sensing properties to CuO mesoporous thin film. It is considered that CuO mesoporous thin film had smaller grain size (~30 nm) and film thickness (~200 nm), and the resulting high specific surface area, compared with CuO hollow-sphere film whose grain size was ~100 nm, film thickness was ~8 μm and shell thickness was ~200 nm. To further improve gas sensing properties of CuO hollow-sphere film, burning the organics while minimizing the grain size by fast densification via flash sintering or spark plasma sintering is proposed.

5. Conclusions

1. Novel Cu(II) complex inks with high adhesion to substrates were successfully prepared and the evolution of phase and microstructure during thermal heating could be investigated in the ink-printed films.
2. It was found that Cu nucleation rate increased with shorter nucleation time periods with increasing the molar ratio of hexylamine solvent to Cu(II) precursor in the ink.
3. During thermal heating of the printed film with the ink with high molar ratio of hexylamine to Cu(II), small Cu particles were produced with narrow size distribution and highly packed dense structure inside the film, resulting in improvement of electrical conductivity of the printed film.

The selection rules for ink formulation compatible with Cu metallization are suggested.

4. Sintering of the ink-printed films, promoted under a reducing HCOOH atmosphere and higher heating temperature, improved the electrical conductivity of the printed films.

The selection rules for sintering condition compatible with Cu metallization are suggested.

5. To obtain pure oxide phase with high specific surface area for applications in the functional devices such as gas sensor and photoelectrochemical cell for water splitting, two strategies were suggested and tried:
 - (1) Thin film was prepared with reduced thickness and heated at higher temperatures.
 - (2) Direct printing synthesis of oxide hollow spheres on substrates was realized for the first time through the nanoscale Kirkendall effect
6. (1) Using 1 : 4 ink with high hexylamine content, the mesoporous/porous CuO thin films were successfully prepared. The mesoporous film calcined at 500 °C revealed the best gas sensing response, attributed to sufficient hole concentration, good crystallinity and the highest surface-to-volume ratio. The porous film calcined at 600 °C exhibited the fastest response time, due to both the excellent crystallinity and the low grain boundary density.
7. (2) Using 1 : 1 ink with low hexylamine content, the direct printing synthesis of metal oxide hollow spheres in the form of film on a substrate was reported for the first time. This method offers facile, scalable high-throughput production and device fabrication processes. The CuO films with hollow spheres, prepared via direct printing synthesis at 500 °C, showed high gas responses and permissible

response speeds to reducing gases and high photocurrent density, compared to conventional CuO powder films and to the values previously reported. These results exemplify the successful realization of a high-throughput printing fabrication method for the creation of superior nanostructured devices.

Bibliography

Chapter 1.

- [1] J. Perelaer, P. J. Smith, D. Mager, D. Soltman, S. K. Volkman, V. Subramanian, J. G. Korvink, U. S. Schubert, *Journal of Materials Chemistry*, **20** (2010) 8446.
- [2] B. Y. Ahn, E. B. Duoss, M. J. Motala, X. Guo, S.-I. Park, Y. Xiong, J. Yoon, R. G. Nuzzo, J. A. Rogers, J. A. Lewis, *Science*, **323** (2009) 1590.
- [3] H. Minemawari, T. Yamada, H. Matsui, J. Tsutsumi, S. Haas, R. Chiba, R. Kumai, T. Hasegawa, *Nature*, **475** (2011) 364.
- [4] J. Z. Wang, Z. H. Zheng, H. W. Li, W. T. S. Huck, H. Sirringhaus, *Nature Materials*, **3** (2004) 171.
- [5] J. Perelaer, B.-J. de Gans, U. S. Schubert, *Advanced Materials*, **18** (2006) 2101.
- [6] J. Wang, M. Musameh, *Analyst*, **129** (2004) 1.
- [7] W. K. Lee, Z. Dai, W. P. King, P. E. Sheehan, *Nano Letters*, **10** (2010) 129.
- [8] Y. Lin, K. A. Watson, M. J. Fallbach, S. Ghose, J. G. Smith Jr., D. M. Delozier , W. Cao , R. E. Crooks, J. W. Connell, *ACS Nano*, **3** (2009) 871.

Chapter 2.

- [1] J. R. Greer, R. A. Street, *Acta materialia*, **55** (2007) 6345.
- [2] J. Frenkel, *Journal of Physics*, **9** (1945) 385.
- [3] H. E. Exner, *Reviews on Powder Metallurgy and Physical Ceramics*, **1** (1979) 1.
- [4] W. D. Kingery, M. Berg, *Journal of Applied Physics*, **26** (1955) 1205.
- [5] R. L. Coble, *Journal of Applied Physics*, **32** (1961) 787.
- [6] M. L. Allen, M. Aronniemi, T. Mattila, A. Alastalo, K. Ojanperä, M. Suhonen, Heikki Seppä, *Nanotechnology*, **19** (2008) 175201.
- [7] D. J. Lee, S. H. Park, S. Jang, H. S. Kim, J. H. Oh, Y. W. Song, *Journal of Micromechanics and Microengineering*, **21** (2011) 125023.
- [8] J. Perelaer, B.-J. de Gans, U. S. Schubert, *Advanced Materials*, **18** (2006) 2101.
- [9] J. Perelaer, M. Klokkenburg, C. E. Hendriks, U. S. Schubert, *Advanced Materials*, **21** (2009) 4830.
- [10] S. Wünscher, S. Stumpf, A. Teichler, O. Pabst, J. Perelaer, E. Beckert, U. S. Schubert, *Journal of Materials Chemistry*, **22** (2012) 24569.
- [11] T. Kumpulainen, J. Pekkanen, J. Valkama, J. Laakso, R. Tuokko, M. Mäntysalo, *Optics & Laser Technology*, **43** (2011) 570.
- [12] B.-Y. Wang, T.-H. Yoo, Y.-W. Song, D.-S. Lim, Y.-J. Oh, *ACS Applied Materials & Interfaces*, **5** (2013) 4113.
- [13] H.-J. Hwang, W.-H. Chung, H.-S. Kim, *Nanotechnology*, **23** (2012) 485205.
- [14] S. Magdassi, M. Grouchko, O. Berezin, A. Kamyshny, *ACS Nano*, **4** (2010) 1943.
- [15] M. Grouchko, A. Kamyshny, C. F. Mihailescu, D. F. Anghel, S. Magdassi, *ACS Nano*, **5** (2011) 3354.

Chapter 3.

- [1] B.-Y. Wang, T.-H. Yoo, Y.-W. Song, D.-S. Lim, Y.-J. Oh, *ACS Applied Materials and Interfaces*, **5** (2013) 4113.
- [2] M. Pashchanka, R. M. Prasad, R. C. Hoffmann, A. Gurlo, J. J. Schneider, *European Journal of Inorganic Chemistry*, (2013) 1481.
- [3] B. Lee, Y. Kim, S. Yang, I. Jeong, J. Moon, *Current Applied Physics*, **9** (2009) e157.
- [4] M. A. Mohamed, A. K. Galwey, S. A. Halawy, *Thermochimica Acta*, **411** (2004) 13.
- [5] J. M. Montes, J. A. Rodriguez, E. J. Herrera, *Powder Metallurgy*, **46** (2003) 251.
- [6] A. Yabuki, N. Arriffin, M. Yanase, *Thin Solid Films*, **519** (2011) 6530.
- [7] H. Ito, W. Oka, H. Goto, H. Umeda, *Japanese Journal of Applied Physics*, **45** (2006) 4325.
- [8] C. W. Macosko, *Rheology: Principles, Measurements, and Applications*; Wiley-VCH: New York, 1994, Ch. 2.
- [9] T. F. Tadros, *Rheology of Dispersions: Principles and Applications*; Wiley-VCH: New York, 2010, Ch. 3.
- [10] F. C. Krebs, *Solar Energy Materials and Solar Cells*, **93** (2009) 394.
- [11] P. Baraldi, *Spectrochimica Acta Part A: Molecular and Biomolecular Spectroscopy*, **35** (1979) 1003.
- [12] A. M. Heyns, *Journal of Molecular Structure*, **18** (1973) 471.
- [13] A. M. Heyns, *Journal of Molecular Structure*, **127** (1985) 9.
- [14] A. M. Heyns, *Journal of Molecular Structure*, **127** (1985) 217.
- [15] A. M. Heyns, K.-J. Range, *Journal of Molecular Structure*, **162** (1987) 57.
- [16] M. A. Mohamed, A. K. Galwey, S. A. Halawy, *Thermochimica Acta*, **411** (2004) 13.
- [17] X.-G. Li, M.-R. Huang, H. Bai, *Journal of Applied Polymer Science*, **73** (1999) 2927.

- [18] Calculated using Advanced Chemistry Development (ACD/Labs) Software V11.02 (© 1994–2010 ACD/Labs)).
- [19] CRC Handbook of Chemistry and Physics, CRC Press, Boca Raton, Florida, 1995.
- [20] P. S. Surdhar, S. P. Mezyk, D. A. Armstrong, *The Journal of Physical Chemistry*, **93** (1989) 3360.
- [21] S. Jeong, K. Woo, D. Kim, S. Lim, J. S. Kim, H. Shin, Y. Xia, J. Moon, *Advanced Functional Materials*, **18** (2008) 679.
- [22] K. Woo, D. Kim, J. S. Kim, S. Lim, J. Moon, *Langmuir*, **25** (2009) 429.
- [23] Y.-I. Lee, K.-J. Lee, Y.-S. Goo, N.-W. Kim, Y. Byun, J.-D. Kim, B. Yoo, Y.-H. Choa, *Japanese Journal of Applied Physics*, **49** (2010) 086501.
- [24] Y.-S. Goo, Y.-I. Lee, N. Kim, K.-J. Lee, B. Yoo, S.-J. Hong, J.-D. Kim, Y.-H. Choa, *Surface and Coatings Technology*, **205** (2010) S369.
- [25] X. Wang, J. C. Hanson, A. I. Frenkel, J.-Y. Kim, J. A. Rodriguez, *The Journal of Physical Chemistry B*, **108** (2004) 13667.
- [26] J. R. Davis, Copper and Copper Alloys; ASM International, 2001.
- [27] S. Jang, Y. Seo, J. Choi, T. Kim, J. Cho, S. Kim, D. Kim, *Scripta Materialia*, **62** (2010) 258.

Chapter 4.

- [1] J. Rouquerol, D. Avnir, C. W. Fairbridge, D. H. Everett, J. H. Haynes, N. Pernicone, J. D. F. Ramsay, K. S. W. Sing, K. K. Unger, *Pure and Applied Chemistry*, **66** (1994) 1739.
- [2] T. L. Barr, *The Journal of Physical Chemistry*, **82** (1978) 1801.
- [3] J. F. Moulder, W. F. Stickle, P. E. Sobol, K. D. Bomben, *Handbook of X-ray Photoelectron Spectroscopy: A Reference Book of Standard Spectra for Identification and Interpretation of XPS Data*, Physical Electronics, Minnesota, 1995.
- [4] J. Ghijsen, L. H. Tjeng, J. van Elp, H. Eskes, J. Westerink, G. A. Sawatzky, M. T. Czyzyk, *Physical Review B*, **38** (1988) 11322.
- [5] J. J. Teo, Y. Chang, H. C. Zeng, *Langmuir*, **22** (2006) 7369.
- [6] C. C. Chusuei, M. A. Brookshier, D. W. Goodman, *Langmuir*, **15** (1999) 2806.
- [7] J. E. Castle, *Nature Physical Science*, **234** (1971) 93.
- [8] N. Yamazoe, K. Shimanoe, *Sensors and Actuators B: Chemical*, **128** (2008) 566.
- [9] A. Crucolini, R. Narducci, R. Palombari, *Sensors and Actuators B: Chemical*, **98** (2004) 227.
- [10] Y. K. Jeong, G. M. Choi, *Journal of Physics and Chemistry of Solids*, **57** (1996) 81.
- [11] N. D. Hoa, N. V. Quy, H. Jung, D. Kim, H. Kim, S.-K. Hong, *Sensors and Actuators B: Chemical*, **146** (2010) 266.
- [12] A. P. Rambu, N. Iftimie, V. Nica, *Journal of Materials Science*, **47** (2012) 6979.
- [13] L. Liao, Z. Zhang, B. Yan, Z. Zheng, Q. L. Bao, T. Wu, C. M. Li, Z. X. Shen, J. X. Zhang, H. Gong, J. C. Li, T. Yu, *Nanotechnology*, **20** (2009) 085203.
- [14] N. D. Hoa, N. V. Quy, M. A. Tuan, N. V. Hieu, *Physica E: Low-dimensional Systems and Nanostructures*, **42** (2009) 146.

- [15] N. D. Hoa, S. Y. An, N. Q. Dung, N. V. Quy, D. Kim, *Sensors and Actuators B: Chemical*, **146** (2010) 239.
- [16] C. Wang, X. Q. Fu, X. Y. Xue, Y. G. Wang, T. H. Wang, *Nanotechnology*, **18** (2007) 145506.
- [17] Y. Zhang, X. He, J. Li, H. Zhang, X. Gao, *Sensors and Actuators B: Chemical*, **128** (2007) 293.
- [18] X. Gou, G. Wang, J. Yang, J. Park, D. Wexler, *Journal of Materials Chemistry*, **18** (2008) 965.
- [19] J.-Y. Li, S. Xiong, B. Xi, X.-G. Li, Y.-T. Qian, *Crystal Growth & Design*, **9** (2009) 4108.
- [20] P. Raksa, A. Gardchareon, T. Chairuangsri, P. Mangkorntong, N. Mangkorntong, S. Choopun, *Ceramics International*, **35** (2009) 649.
- [21] D. Barreca, E. Comini, A. Gasparotto, C. Maccato, C. Sada, G. Sberveglieri, E. Tondello, *Sensors and Actuators B: Chemical*, **141** (2009) 270.
- [22] C. Yang, X. Su, F. Xiao, J. Jian, J. Wang, *Sensors and Actuators B: Chemical*, **158** (2011) 299.
- [23] R. Li, J. Du, Y. Luan, Y. Xue, H. Zou, G. Zhuang, Z. Li, *Sensors and Actuators B: Chemical*, **168** (2012) 156.
- [24] G. Zhu, H. Xu, Y. Xiao, Y. Liu, A. Yuan, X. Shen, *ACS Applied Materials & Interfaces*, **4** (2012) 744.
- [25] A. Taubert, F. Stange, Z. Li, M. Junginger, C. Günter, M. Neumann, A. Friedrich, *ACS Applied Materials & Interfaces*, **4** (2012) 791.
- [26] M. P. Pechini, U.S. Patent 1967, 3330697.
- [27] J. C. Park, J. Kim, H. Kwon, H. Song, *Advanced Materials*, **21** (2009) 803.
- [28] J. J. Teo, Y. Chang, H. C. Zeng, *Langmuir*, **22** (2006) 7369.
- [29] J. Xu, D. Xue, *Acta Materialia*, **55** (2007) 2397.
- [30] Y.-H. Won, L. A. Stanciu, *Sensors*, **12** (2012) 13019.
- [31] H. Liu, Y. Zhou, S. A. Kulinich, J.-J. Li, L.-L. Han, S.-Z. Qiao, X.-W.

- Du, *Journal of Materials Chemistry A*, **1** (2013) 302.
- [32] H. J. Fan, U. Gösele, M. Zacharias, *Small*, **3** (2007) 1660.
- [33] A. D. Smigelskas, E. O. Kirkendall, *Transactions of the American Institute of Mining, Metallurgical and Petroleum Engineers*, **171** (1947) 130.
- [34] Y. Yin, R. M. Rioux, C. K. Erdonmez, S. Hughes, G. A. Somorjai, A. P. Alivisatos, *Science*, **304** (2004), 711.
- [35] K. N. Tu, U. Gösele, *Applied Physics Letters*, **86** (2005) 093111.
- [36] J. Svoboda, F. D. Fischer, D. Vollath, *Acta Materialia*, **57** (2009) 1912.
- [37] W. Wang, M. Dahl, Y. Yin, *Chemistry of Materials*, **25** (2013) 1179.
- [38] R. Nakamura, D. Tokozakura, H. Nakajima, J.-G. Lee, H. Mori, *Journal of Applied Physics*, **101** (2007) 074303.
- [39] J.-H. Lee, *Sensors and Actuators B: Chemical*, **140** (2009) 319.
- [40] H. J. Fan, M. Knez, R. Scholz, D. Hesse, K. Nielsch, M. Zacharias, U. Gösele, *Nano Letters*, **7** (2007) 993.
- [41] G. Xiao, Y. Zeng, Y. Jiang, J. Ning, W. Zheng, B. Liu, X. Chen, G. Zou, B. Zou, *Small*, **9** (2013) 793.
- [42] A. Bejaoui, J. Guerin, K. Aguir, *Sensors and Actuators B: Chemical*, **181** (2013) 340.
- [43] D. Zappa, E. Comini, R. Zamani, J. Arbiol, J. R. Morante, G. Sberveglieri, *Sensors and Actuators B: Chemical*, **182** (2013) 7.
- [44] H. Kim, C. Jin, S. Park, S. Kim, C. Lee, *Sensors and Actuators B: Chemical*, **161** (2012) 594.
- [45] N. S. Ramgir, S. K. Ganapathi, M. Kaur, N. Datta, K. P. Muthe, D. K. Aswal, S. K. Gupta, J. V. Yakhmi, *Sensors and Actuators B: Chemical*, **151** (2010) 90.
- [46] C. Zong, X. Liu, H. Sun, G. Zhang, L. Lu, *Journal of Materials Chemistry*, **22** (2012) 18418.
- [47] J. Y. Zheng, G. Song, C. W. Kim, Y. S. Kang, *Electrochimica Acta*, **69** (2012) 340.
- [48] C.-Y. Chiang, Y. Shin, S. Ehrman, *Journal of The Electrochemical*

Society, **159** (2012) B227.

- [49] C.-Y. Chiang, Y. Shin, K. Aroh, S. Ehrman, *International Journal of Hydrogen Energy*, **37** (2012) 8232.
- [50] C.-Y. Chiang, K. Aroh, N. Franson, V. R. Satsangi, S. Dass, S. Ehrman, *International Journal of Hydrogen Energy*, **36** (2011) 15519.

국문초록

Inkjet, microcontact, offset 및 gravure 공정 등의 인쇄 기술은 고체 전자소자, 특히 유연 전자소자를 더 빠르게 저가의 대면적 제조 공정으로 제조할 수 있기 때문에 기존의 진공 제조 기술의 대체 공정으로써 주목 되어 왔다. 이러한 인쇄 기술의 발전에 따라 각각의 세부적인 인쇄 공정에 적합한 유연학적 특성을 가진 잉크의 제조가 새로운 이슈로 부각되었다. 인쇄 전자에 대한 초창기 연구는 주로 금 (Au), 은 (Ag) 및 구리 (Cu) 나노입자 기반 잉크를 사용한 금속 배선 전극의 형성에 집중되어 왔다. 그러나 그러한 나노입자 기반 잉크는 입자의 균질한 분산 및 대량 합성의 어려움, 낮은 보관 안정성 및 계면활성제나 분산제 등의 사용에 따른 가격 상승 등의 요인으로 인해 실제 산업적 생산에 심각한 어려움 가지고 있다. 그러므로 본 연구에서 높은 대기 안정성을 가지고 대량 합성이 손쉬운 새로운 유기금속 전구체 기반 잉크들이 제조되고 그것들의 적용 가능성이 조사된다.

그러나 나노입자 기반 잉크의 경우와는 달리, 유기금속 전구체 기반 잉크로 인쇄된 막에서 고상 입자 및 막의 형성, 그것들의 소결 거동과 미세조직 변화에 대한 연구는 이전에 시도되지 않았다. 특별히 Cu를 포함한 금속 전극의 기판에 대한 낮은 접착성이 유기금속 전구체 기반 잉크로 인쇄된 막에 대한 연구를 어렵게 만든다. 따라서 본 연구에서는 Cu(II) formate tetrahydrate, hexylamine 및 ethyl cellulose를 사용하여 기판과의 접착성이 우수하고 점도가

조절된 새로운 Cu 이온 착체 잉크가 제조되었고, 잉크 막이 인쇄 Cu 전극, p형 반도체 CuO 가스센서 및 광전기화학적 물 분해를 위한 광 전극과 같은 다양한 소자로의 적용을 위해 glass, SiO₂/Si 및 SnO₂:F (FTO) 기판 위에 직접 인쇄되었고 열처리 되었다. Cu 이온 착체 잉크의 열적 분해 거동, 고상 입자 형성, 상 및 미세조직 발달 및 소결 거동에 대한 자세한 연구는 각 소자 응용에 적합한 인쇄 막의 최적화를 가능케 하였다.

Part I에서, Fourier-transform infrared spectroscopy (FT-IR), thermogravimetric analysis (TGA), differential scanning calorimetry (DSC) 및 field emission scanning electron microscopy (FE-SEM) 연구들을 통하여 Cu 이온 착체 잉크의 Cu(II) formate tetrahydrate 전구체와 hexylamine 용매 사이의 몰 농도 비율의 변화가 잉크의 열 분해 시 Cu의 핵 생성 거동에서의 차이를 야기시킨다는 것이 발견되었다. 구체적으로, 상대적으로 낮은 hexylamine 양을 포함한 잉크로 인쇄된 막의 열 분해 시, Cu 나노입자가 느린 핵 생성 속도와 더 긴 핵 생성 시간을 가지고 생성되었고, 결과적으로 막의 미세조직은 넓은 크기 분포를 가진 큰 입자들로 구성되었다. 이 막의 내부에서 Cu 입자의 충진 밀도는 낮았고, 따라서 전기 비저항은 높았다. 반대로, 높은 hexylamine 양을 포함한 잉크로 인쇄된 막의 열 분해 시, Cu 나노입자가 빠른 핵 생성 속도와 더 짧은 핵 생성 시간을 가지고 생성되었고, 결과적으로 막의 미세조직은 좁은 크기 분포를 가진 작은 입자들이 치밀하게 충진된 구조를 나타내었다. 결과적으로, 더 낮은 전기 비저항이 이 막에서 도달되었다. 이러한 결과들을 바탕으로, 높은 전기 전도도를 요구하는 인쇄 금속 전극을

위한 금속 이온 잉크는 유기금속 전구체 대비 반응성 용매의 농도가 높아지도록 제조 되는 것이 바람직하다고 결론지어진다. 다음으로, 생성된 Cu 나노입자 표면에 오염된 산화물 층을 환원시켜 제거함에 따라 입자 소결을 촉진 시켜 전기 전도도 향상을 도모하기 위해 개미산 (HCOOH) 가스를 이용한 환원 분위기에서 소결 공정이 시도되었다. 이러한 환원 분위기 소결을 통하여 열처리 시간에 따라 Cu 나노입자 성장이 촉진되었고, 결과적으로 인쇄 막의 전기 비저항이 10배 정도 감소될 수 있었다. 또한 열처리 온도를 높여 Cu 나노입자들의 목 성장 및 치밀화를 유도시켜 인쇄 막의 전기 비저항이 낮아질 수 있음을 확인하였다. 결과적으로 이 세가지 방법 (잉크 조성 선택, 환원분위기 및 승온 소결)을 이용한 최적화된 공정을 통하여 금속 이온 착체 잉크로 인쇄된 금속 전극의 가장 낮은 전기 비저항 ($\sim 5.2 \mu\Omega\text{cm}$)을 얻을 수 있었다.

Part II에서, 기능성 가스 센서 및 광전기화학 소자로의 적용을 위해 높은 결정성과 비표면적을 가진 순수 산화물 막이 본 연구에서 개발된 새로운 Cu 이온 착체 잉크 인쇄 법을 통해 제조되었다. 첫 번째로, Cu(II) 전구체 대비 높은 hexylamine 함량을 가진 Cu 이온 착체 잉크가 메조크기 다공성 p형 반도체 CuO 센서 막의 손쉬운 제조를 위해 사용되었다. 200°C 부터 600°C 까지의 공기 중 열처리를 통해 순수한 다결정 CuO 막이 다공성 구조를 가지고 형성되었다. 그러한 다공성 구조는 치밀하게 충진된 작은 Cu 나노입자들 사이의 빈 공간의 열적 진화에 기인한 실린더 모양의 상호 연결된 기공 채널에 의해 형성되었다. 특히 500°C

에서 1 시간 열처리로 생성된 메조크기의 CuO 막은 충분한 hole 농도, 좋은 결정성 및 가장 높은 비표면적을 가지고 가장 높은 수소 및 에탄올 가스 감응도를 나타내었다. 600 °C에서 생성된 다공성 막은 가장 우수한 결정성 및 낮은 결정립계 밀도를 가지고 가장 빠른 가스 응답 속도를 나타내었다. 순수한 CuO를 이용하여 얻어진 이 결과들은 고성능 p형 반도체 가스 센서의 개발을 위한 올바른 방향을 제공한다. 게다가, 이 연구에서 메조크기 다공성 구조를 제조하는데 사용된 새로운 잉크 용액 법은 인쇄 센서 소자의 실현 및 센서 성능 향상을 위한 산화물에 이온 도핑 또는 합금화를 위한 손쉬운 접근법을 제공할 수 있다.

두 번째로, 높은 결정상 및 비표면적을 가진 순수한 산화물 막을 제조하기 위한 또 다른 새롭고 손쉬운 인쇄 공정이 소개되었다. 기판 위에 막의 형태로 금속 산화물 중공입자의 직접 인쇄 형성이 처음으로 보고된다. 이 방법은 손쉽고 빠른 속도로 대량생산 및 소자 제조공정을 가능하게 한다. 인쇄는 낮은 hexylamine 양을 가진 Cu 이온 착체 잉크를 사용하여 doctor blade 법으로 수행되었다. 단지 산소에서 열처리 후 1 μm 이하 직경의 다결정 구리 산화물 중공 입자가 기판과의 좋은 접착성을 가지고 막의 형태로 자발적으로 형성되었다. 이러한 자발적 중공화 기작은 승온 시 산화 도중 일어나는 Kirkendall 효과로부터 비롯되었다. 500 °C에서 직접 인쇄 합성을 통해 제조된 중공입자들로 구성된 CuO 막은 구성 입자들의 완전한 중공 구조, 다공성의 거칠한 껍질 구조, 단상, 높은 결정성 및 유기/고분자 잔류물의 부재를 가지고 우수한 p형 반도체 가스 센서 및 광전기화학적 물 분해용 광

전극의 제조를 실현시켰다. 결과적으로, CuO 중공입자 막은 기존의 CuO 분말로 구성된 막과 이전에 보고된 것들에 비하여 환원성 가스들에 대한 높은 가스 감응도와 허용된 응답 속도 및 높은 광전류밀도를 나타내었다. 이 결과들은 우수한 나노구조 소자의 제조를 위한 고 수율 인쇄 제조의 성공적인 실현을 예증한다.

주요어: 인쇄전자, 잉크, 유기금속, 미세조직, 금속화, 가스센서, 광전기화학, 구리, 산화구리

학 번: 2010-31308

My Publications

- International SCI Journals (Peer-reviewed)

14. **Yun-Hyuk Choi**, Dai-Hong Kim, Hyun Soo Han, Sun Shin, Seong-Hyeon Hong, and Kug Sun Hong*,
“Direct Printing Synthesis of Self-Organized Copper Oxide Hollow Spheres on a Substrate Using Copper(II) Complex Ink: Gas Sensing and Photoelectrochemical Properties”
Langmuir, (2014) in press, DOI: 10.1021/la404098s.
13. **Yun-Hyuk Choi**, Kug Sun Hong*,
“Homogeneous size reduction of metallic glass in a common acidic aqueous medium”,
Materials Letters, 100 (2013) 299-302.
12. **Yun-Hyuk Choi**, Dai-Hong Kim, Seong-Hyeon Hong, Kug Sun Hong*,
“H₂ and C₂H₅OH sensing characteristics of mesoporous p-type CuO films prepared via a novel precursor-based ink solution route”,
Sensors and Actuators B: Chemical, 178 (2013) 395-403.
: Highlighted as a news article on the Vertical News, 9 April 2013
[\(<http://www.verticalnews.com/newsletters/Journal-of-Technology/2013-04-09/71851TE.html>\)](http://www.verticalnews.com/newsletters/Journal-of-Technology/2013-04-09/71851TE.html)
11. **Yun-Hyuk Choi***, Jaeho Lee, Suk Jun Kim, Dong-Hee Yeon and Younghun Byun,
“Highly conductive polymer-decorated Cu electrode films printed on glass substrates with novel precursor-based inks and pastes”,
Journal of Materials Chemistry, 22 [8] (2012) 3624-3631.

10. Suk Jun Kim, Jaeho Lee, **Yun-Hyuk Choi**, Dong-Hee Yeon, Younghun Byun*,
 “Effect of copper concentration in printable copper inks on film fabrication”,
Thin Solid Films, 520 [7] (2012) 2731-2734.
09. Xavier Bulliard, Anass Benayad, Kwang-Hee Lee, **Yun-Hyuk Choi**, Jae Cheol
 Lee, Jong-Jin Park* and Jong-Min Kim,
 “Cobalt oxide polymorph growth on electrostatic self-assembled nanoparticle
 arrays for dually tunable nano-textures”,
Nanotechnology, 22 [47] (2011) 475602.
**: Cover Gallery and Featured Article of Nanotechnology (Volume 22,
 Number 47, 25 November 2011)**
08. **Y.-H. Choi**, X. Bulliard, A. Benayad, Y. Leterrier, J.-A.E. Månsen, K.-H. Lee,
 D. Choi*, J.-J. Park*, J. Kim,
 “Design and fabrication of compositionally graded inorganic oxide thin films:
 Mechanical, optical and permeation characteristics”,
Acta Materialia, 58 [19] (2010) 6495-6503.
: Highlighted as a news article on the Vertical News, 7 December 2010
(<http://technology.verticalnews.com/articles/4634628.html>)
07. **Yun-Hyuk Choi**, Young Gu Lee, Xavier Bulliard, Kwang-Hee Lee, Sangyoon
 Lee, Dukhyun Choi*, Jong-Jin Park* and Jong Min Kim,
 “Homogeneous Al₂O₃ multilayer structures with reinforced mechanical stability
 for high-performance and high-throughput thin-film encapsulation”,
Scripta Materialia, 62 [7] (2010) 447-450.

06. Kyoung-Seok Son*, Ji-Sim Jung*, Kwang-Hee Lee*, Tae-Sang Kim*, Joon-Seok Park*, **Yun-Hyuk Choi***, KeeChan Park*, Jang-Yeon Kwon*, Bonwon Koo*, and Sang-Yoon Lee*,
 “Characteristics of Double-Gate Ga-In-Zn-O Thin-Film Transistor”,
IEEE Electron Device Letters, 31 [3] (2010) 219-221.
05. Young Gu Lee, **Yun-Hyuk Choi**, In Seo Kee, Hong Shik Shim, YongWan Jin, Sangyoonee Lee, Ken Ha Koh, Soonil Lee*,
 “Thin-film encapsulation of top-emission organic light-emitting devices with polyurea/Al₂O₃ hybrid multi-layers”,
Organic Electronics, 10 [7] (2009) 1352-1355.
04. Ji-Hwan Kwon, **Yun-Hyuk Choi**, Dai Hong Kim, Myeong Yang, Jiyoung Jang, Tae Woong Kim, Seong-Hyeon Hong, Miyoung Kim*,
 “Orientation relationship of polycrystalline Pd-doped SnO₂ thin film deposits on sapphire substrates”,
Thin Solid Films, 517 [2] (2008) 550-553.
03. **Yun-Hyuk Choi**, Myung Yang, Seong-Hyeon Hong*,
 “H₂ sensing characteristics of highly textured Pd-doped SnO₂ thin films”,
Sensors and Actuators B: Chemical, 134 [1] (2008) 117-121.
02. **Yun-Hyuk Choi**, Seong-Hyeon Hong*,
 “H₂ sensing properties in highly oriented SnO₂ thin films”,
Sensors and Actuators B: Chemical, 125 [2] (2007) 504-509.
: Ranked TOP 21 among TOP 25 Hottest Articles in Sensors and Actuators B: Chemical, Chemistry, ScienceDirect, Elsevier (July to September 2007)

01. Sung Myung, Kwang Heo, Minbaek Lee, **Yun-Hyuk Choi**, Seong-Hyeon Hong and Seunghun Hong*,
“‘Focused’ assembly of V₂O₅ nanowire masks for the fabrication of metallic nanowire sensors”,
Nanotechnology, 18 [20] (2007) 205304.